Divergent changes in aerosol optical hygroscopicity and new particle formation ~~during~~~~induced by~~ heatwaves ~~of summer 2022~~

Yuhang Hao[1, a], Peizhao Li[1, a], Yafeng Gou[1], Zhenshuai Wang[1], Mi Tian[1], Yang Chen[2], Ye Kuang[3], Hanbing Xu[4], Fenglian Wan[1], Yuqian Luo[1], Wei Huang[5], Jing Chen[1, 6, *]

[1] College of Environment and Ecology, Chongqing University, Chongqing 400045, China

[2] Center for the Atmospheric Environment Research, Chongqing Institute of Green and Intelligent Technology, Chinese Academy of Sciences, Chongqing 400714, China

[3] Institute for Environmental and Climate Research, Jinan University, Guangzhou 511443, China

[4] Experimental Teaching Center, Sun Yat-sen University, Guangzhou 510275, China

[5] National Meteorological Center, China Meteorological Administration, Beijing 100081, China

[6] Key Laboratory of Three Gorges Reservoir Region's Eco-Environment, Ministry of Education, Chongqing University, Chongqing 400045, China

[a] These authors contributed equally

Correspondence to: Jing Chen (chen.jing@cqu.edu.cn)

Abstract. As a crucial climate-forcing driver, the aerosol optical enhancement factor (*f*(RH)) is significantly modulated by chemical compositions and the evolution of particle number size distribution (PNSD), e.g., during new particle formation (NPF). However, the mechanisms regulating aerosol optical hygroscopicity during different NPF days, particularly those influenced by heatwaves due to global warming, remain poorly understood. In the extremely hot summer of 2022 in urban Chongqing of southwest China, simultaneous measurements of aerosol optical and hygroscopic properties, PNSD, and bulk chemical compositions were conducted. Two distinct types of NPF were identified: the ones with relatively polluted period (~~NPF~~$_{P}$NPF$_{polluted}$) and clean cases during heatwave-dominated period (~~NPF~~$_{C, HW}$NPF$_{clean, HW}$). Compared to the ~~NPF~~$_{P}$NPF$_{polluted}$ events, ~~NPF~~$_{C, HW}$NPF$_{clean, HW}$ occurred approximately one hour earlier and the subsequent growth was prolonged, accompanied by a smaller aerosol effective radius (R_{eff}) and lower formation/growth rate during heatwaves. This agreed with the concurrently increased aerosol hemispheric backscattering fraction and scattering Ångström exponent. *f*(RH) was generally higher on NPF days in comparison to that for non-event cases in both periods. Moreover, heatwave-induced stronger photooxidation may intensify the formation of more hygroscopic secondary components, as well as the atmospheric aging/subsequent growth of both pre-existing and newly formed particles, thereby enhancing *f*(RH) especially during ~~NPF~~$_{C, HW}$NPF$_{clean, HW}$ days. The promoted *f*(RH) and lowered R_{eff} could synergistically elevate the aerosol direct radiative forcing, specifically under persistent heatwave conditions. Further in-depth exploration on molecular-level characterizations and aerosol radiative impacts of both direct and indirect interactions during weather extremes (e.g., heatwaves) with the warming climate are recommended.

1 Introduction

Weather extremes (e.g., heatwaves) have become more and more frequent and intense largely due to the global climate change, and the heatwave-driven

environmental, climatic, and health effects have garnered widespread attention (Hauser et al., 2016; Sun et al., 2016). The China Climate Bulletin 2022 confirmed that the national average temperature reached an unprecedented high level since 2012 (China Meteorological Administration, 2022), and the risk of heatwaves in China will persist and potentially intensify in the future (Guo et al., 2016; Li et al., 2017). Extreme heatwave events could pose significant threats to human health, the survival of organisms, agriculture, and socio-economic activities (e.g., power supply restrictions) (Anderson and Bell, 2011; Ma et al., 2021; Su, 2021). Moreover, heatwaves can trigger natural disasters such as droughts and wildfires, affecting social stability (Sharma and Mujumdar, 2017).

Heatwaves could also affect the atmospheric physical and chemical processes by modulating ambient meteorological conditions. Specifically, extremely high temperature weather is typically characterized by a combination of intensified solar radiation with elevated temperature and low humidity levels. This could significantly affect the formation and evolution of secondary aerosols in the atmosphere (Bousiotis et al., 2021; Hamed et al., 2011; Kurtén et al., 2007), given that the air temperature is crucial for chemical reactions (Xu et al., 2011). New particle formation (NPF) serves as a crucial source of atmospheric particulate matter and plays a significant role in the secondary transformation processes in the atmosphere (Zhu et al., 2021). Generally, NPF involves the initial formation of thermodynamically stable clusters from condensable vapors (e.g., ammonia, sulfuric acid, and organic precursor gases) and subsequent growth of the formed clusters, eventually reaching detectable sizes or even larger dimensions (Kerminen et al., 2018; Kulmala et al., 2003, 2012). Over time, these newly formed particles have the potential to serve as cloud condensation nuclei (CCN), thereby impacting the global climate (Salma et al., 2016). NPF events normally introduce a sharp increase in the number concentration of nucleation mode particles within a short time, altering the particle number size distribution (PNSD). These variations in PNSD likely influence intrinsic physicochemical properties of aerosols, such as the optical hygroscopicity (Chen et al., 2014; Titos et al., 2016; Zhao et al., 2019).

Aerosol hygroscopicity plays a critical role in the atmospheric environment and climate change, given the complex interaction between aerosol particles and water vapor (Zhao et al., 2019; Zieger et al., 2011). Water uptake by aerosols not only alters the particle size and composition (e.g., as reflected in the aerosol refractive index) but also impacts aerosol scattering efficiency, which further contributes to the uncertainty in aerosol radiative forcing estimation (Titos et al., 2016, 2021). The aerosol optical hygroscopicity parameter, f(RH), defined as the ratio of the scattering coefficient at a certain RH to that of the dry condition, was widely used to describe the aerosol scattering enhancement through water uptake (Covert et al., 1972; Titos et al., 2016; Zhao et al., 2019). Numerous studies have demonstrated that f(RH) is influenced by the size distribution, in addition to particle chemical composition (Chen et al., 2014; Kuang et al., 2017; Petters and Kreidenweis, 2007; Quinn et al., 2005). There is currently limited research on the variations in aerosol optical hygroscopicity during NPF days despite significant changes in aerosol size distributions and chemical compositions, partly due to that newly formed particles insignificantly affect the optical properties of aerosols (Kuang et al., 2018). However, previous studies have observed the enhancement in aerosol hygroscopicity (Cheung et al., 2020; Wu et al., 2015, 2016) and extinction coefficients (Shen et al., 2011; Sun et al., 2024) during the subsequent growth of NPF. It is suggested that the influence of NPF on aerosol hygroscopicity was likely due to changes in aerosol chemical composition at different stages of NPF events (Cheung et al., 2020), whereas the subsequent particle growth associated with NPF events can significantly affect particle hygroscopicity as well (Wu et al., 2016). Although previous studies showed the dependences of aerosol hygroscopicity on chemical composition (Petters and Kreidenweis, 2007; Titos et al., 2016; Zhao et al., 2019) (e.g., the variation in composition of precursor species during NPF events), it is important to acknowledge that the utilized chemical compositions of NPF were either from $PM_{2.5}$ or PM_1 bulk data. This may differ from the corresponding composition of newly formed ultrafine particles primarily in the nucleation and Aitken modes, further introducing bias in exploring the impacts of NPF and subsequent growth on aerosol optical hygroscopicity. Hence, more

comprehensive investigations on the influencing mechanisms of aerosol optical hygroscopicity from different perspectives are required, e.g., for the aspects of the evolution of particle size distribution in modulating aerosol optical and hygroscopic properties (Tang et al., 2019; Zhao et al., 2019). Additionally, field observations on *f*(RH) under extreme weather conditions (e.g., heatwaves) are rather scarce, largely hindering our understanding of how weather extremes (e.g., extremely high temperature) influence the optical hygroscopic properties of aerosols. This knowledge gap further impedes comprehensive understanding of the aerosol water uptake property and resulted effects on air quality and the climate under varied synoptic conditions.

During the summer of 2022, a rare heatwave event raged throughout China, especially the Sichuan-Chongqing region of southwest China (Chen et al., 2024; Wang et al., 2024), with the daily maximum temperature exceeding 40 ℃ lasted for 29 days observed at Beibei meteorological station in Chongqing (Hao et al., 2023). This persistent heatwave not only impacted residents' daily lives significantly, but also affected the aerosol optical and hygroscopic properties likely through changed aerosol physicochemical characteristics and relevant atmospheric processing during the period. In this study, a field observation was conducted by using a combination of a home-built humidified nephelometer system and a scanning mobility particle sizer (SMPS), along with the total suspended particle (TSP) filter sampling. A main goal of this study is to investigate the influence of heatwaves on both aerosol optical hygroscopicity and the NPF with subsequent growth events, along with the related discrepancies. Furthermore, we aimed to explore the mechanisms behind the variability in *f*(RH) under different meteorological conditions and diverse NPF events. This study will further enrich insights into the potential environmental impacts due to variations in the aerosol optical hygroscopicity and size distribution, specifically under weather extremes (e.g., heatwaves) with the changing climate.

2 Data and Methods

2.1 Field observation

A continuous field observation on aerosol optical, hygroscopic and chemical properties was carried out from July 29 to August 19, 2022. The detailed description of the observation site is available in Supporting Information, S1. During the observation period, urban Chongqing suffered a rare heatwave (Fig. S1; Chen et al., 2024; Wang et al., 2024), which significantly affected the local transportation and industrial activities (Hao et al., 2023). China Meteorological Administration (CMA) defines heatwaves as three or more consecutive days with daily maximum temperature (T_{max}) above 35 °C (http://www.cmastd.cn/standardView.jspx?id=2103; Guo et al., 2016; Sun et al., 2014; Tan et al., 2007). Since no unified definition of heatwaves worldwide, the whole study period was categorized into two stages according to CMA's criteria of the daily T_{max} records and the Excess Heat Factor (EHF) metric proposed by Nairn and Fawcett (2014) (Fig. S2a): (1) the normally hot period from 29 July to 6 August (marked as P1); (2) the heatwave-dominated period from August 7-19 (marked as P2) characterized with the consistently occurrence of T_{max} exceeding 38 °C (approximately the last 25th percentile of temperature records for the whole observation period; Fig. S2b).

2.2 Instrumentation and methods

2.2.1 Measurements of aerosol optical hygroscopicity

The humidified nephelometer system, consisting of two three-wavelength (i.e., 450, 525, and 635 nm) nephelometers (Model Aurora 3000, Ecotech Inc.) and a humidification unit, was used to determine the aerosol light scattering enhancement factor, *f*(RH). Ambient air was firstly dried through a Nafion dryer (model MD-700, Perma Pure LLC) to ensure RH <35%, then split into two streams for both dry and humidified nephelometers operated in parallel. The flowrate for each nephelometer was 2.6 LPM. The aerosol scattering ($\sigma_{sca,\lambda}$) and backscattering coefficients ($\sigma_{bsca,\lambda}$) were detected in a dry state (RH <35%) and at a controlled RH level of 85 ± 1%,

166 respectively, with the humidification efficiency regulated automatically by a
167 temperature-controlled water bath. More details on the home-built humidified
168 nephelometer system are available in Kuang et al. (2017, 2020) and Xue et al. (2022).

169 Hence, *f*(RH) could be calculated as the ratio of the aerosol scattering coefficient
170 at a predefined RH ($\sigma_{sca,\ RH}$) to the dry ($\sigma_{sca,\ dry}$) state, i.e., *f*(RH) = $\sigma_{sca,\ RH}$ / $\sigma_{sca,\ dry}$
171 (Covert et al., 1972). In this study, the *f*(RH) discussed is mainly targeted for the 525
172 nm wavelength, unless otherwise specified. More information about the measurement
173 of humidified nephelometer system was illustrated in Sect. S2 of the supplement.

174 In additional to *f*(RH), aerosol optical parameters, such as scattering Ångström
175 exponent (SAE; Schuster et al., 2006) and hemispheric backscattering fraction (HBF;
176 Collaud Coen et al., 2007), were calculated as below:

177 $$SAE_{\lambda 1/\lambda 2} = \frac{-\ln\left(\sigma_{sca,\ \lambda 1}/\sigma_{sca,\ \lambda 2}\right)}{\ln\left(\lambda 1/\lambda 2\right)} \quad (1)$$

178 $$HBF_{\lambda} = \frac{\sigma_{bsca,\ \lambda}}{\sigma_{sca,\ \lambda}} \quad (2)$$

179 where $\sigma_{sca,\ \lambda}$ and $\sigma_{bsca,\ \lambda}$ represent the aerosol scattering and backscattering
180 coefficients at a specific wavelength λ (e.g., λ1, λ2), respectively.

181 Both HBF and SAE reflect crucial optical properties of aerosols, e.g., an elevated
182 HBF (or SAE) generally signifies a higher concentration (or a smaller particle size) of
183 fine particles within the aerosol population (Jefferson et al., 2017; Kuang et al., 2017;
184 Luoman et al., 2019). The HBF and SAE discussed in this study are targeted for the
185 dry condition, unless otherwise specified. Based on the measurements with the
186 humidified nephelometer system, the equivalent aerosol liquid water content (ALWC)
187 and the corresponding fraction of ALWC (f_W) can also be obtained (Kuang et al, 2018;
188 see Sect. S2 of the supplement).

189 The SMPS-measured concurrent particle number size distributions were further
190 utilized to calculate the aerosol effective radius (R_{eff}) and representative parameters
191 for NPF events, e.g., the formation rate (FR) and growth rate (GR) of new particle,
192 condensation sink (CS) and coagulation sink (CoagS) (Dal Maso et al., 2005; Kulmala
193 et al., 2012). More details are provided in the supplement (Sect. S5).

Results of the offline chemical analysis with TSP filter samples are provided in Sect. S3 and Fig. S3. It should be noted that certain secondary organics and crustal elements (e.g., Ca^{2+}, Mg^{2+}) that could exhibit a broader size distribution may contribute to the observed discrepancy in the total mass concentration between the 24-h TSP samples and daily mean $PM_{2.5}$ (of similar temporal variations; Fig.S3) (Duan et al., 2024; Kim et al., 2020; Xu et al., 2021). Nonetheless, previous studies reported that key components such as SNA (i.e., SO_4^{2-}, NO_3^-, and NH_4^+) and primary organics of $PM_{2.5}$ (or PM_{10}) were predominantly concentrated within the submicron size range (An et al., 2024; Bae et al., 2019; Chen et al., 2019; Duan et al., 2024; Kim et al., 2020; Xu et al., 2024). While the use of TSP samples contains some uncertainties, the bulk chemical information remains reasonable for characterizing the optical and hygroscopic properties of $PM_{2.5}$. The descriptions of simultaneous meteorological and air quality data can be found in Sect. S4, and the 48-h/72-h backward trajectory analysis was given in Sect. S5 of the supplement.

2.2.2 Determination of the aerosol direct radiative forcing (ADRF) enhancement factor

Given the high sensitivity of aerosol optical properties (e.g., f(RH)) to the changes in RH under real atmospheric conditions, the influence of RH, or rather the aerosol hygroscopicity, on ADRF can be quantitatively estimated with the radiative transfer model by the following equation (Chylek and Wong, 1995; Kotchenruther et al., 1999; L. Zhang et al., 2015):

$$\Delta F_R(RH) = -(S_0/4)\times[T_a^2\times(1-A_C)]\times[2\times(1-R_s)^2\times\beta(RH)\times\tau_s - 4\times R_s\times\tau_a] \quad (3)$$

where S_0 is the solar constant, T_a is the atmosphere transmittance, A_C is the fractional cloud amount, R_s is the albedo of the underlying surface, β(RH) is the upscattering fraction at a defined RH, τ_s and τ_a are the optical thicknesses of the aerosol layer due to light scattering and light absorption, respectively, which can be expressed as follows (Kotchenruther et al., 1999):

$$\tau_s = M\times\alpha_s\times f(RH), \tau_a = M\times\alpha_a \quad (4)$$

where M is the column burden of aerosol (unit: gm^{-2}), α_s is the mass scattering efficiency (MSE), and α_a is the mass absorption efficiency (MAE). The direct radiative forcing is usually calculated with the assumption that the absorption enhancement is negligible, in comparison to the aerosol scattering enhancement (Xia et al., 2023).

Hence, the dependence of ADRF on RH (i.e., $f_{RF}(RH)$) can be estimated by equation (5) (Chylek and Wong, 1995; Kotchenruther et al., 1999; L. Zhang et al., 2015):

$$f_{RF}(RH) = \frac{\Delta F_R(RH)}{\Delta F_R(dry)} = \frac{(1-R_s)^2 \times \beta(RH) \times \alpha_s \times f(RH) - 2 \times R_s \times \alpha_a}{(1-R_s)^2 \times \beta(dry) \times \alpha_s \times f(dry) - 2 \times R_s \times \alpha_a} \quad (5)$$

where the constant parameters used were $R_s = 0.15$, $\alpha_a = 0.3$ $m^2 \cdot g^{-1}$ (Hand and Malm, 2007; Fierz-Schmidhauser et al., 2010). It should be noted that the assumed constant α_a might introduce some uncertainty in the calculated $f_{RF}(RH)$, given the fact that the contribution of absorption by brown carbon was unknown, although the mass fraction of BC in TSP remained almost constant (i.e., 4.6% ± 1.1%, Fig. S3) during the observation period. The parameter α_s was calculated by dividing $\sigma_{sca,\,525}$ in the dry condition by the mass concentration of $PM_{2.5}$ (i.e., $\alpha_s = \sigma_{sca,\,525} / PM_{2.5}$). β could be calculated empirically from the measured HBF: $\beta = 0.0817 + 1.8495 \times HBF - 2.9682 \times HBF^2$ (Delene and Ogren, 2002).

3 Results and discussion

3.1 Overview of the aerosol optical hygroscopicity and PNSD measurements

Figure 1 displayed the time series of the measured aerosol scattering coefficients, *f*(RH), PNSD, and the corresponding meteorological conditions and air pollutants during the study period. A sharp decrease in aerosol scattering coefficients and $PM_{2.5}$, accompanied with the continuous excellent visibility over 20 km was observed after August 6, indicating a markedly cleaner environment during P2 in comparison to P1 in summer 2022 of Chongqing. This could be largely attributed to the reduction in anthropogenic emissions (e.g., NO_2, CO, except SO_2) from limited outdoor activities

influenced by the heatwaves in P2, as well as partly suspended industries and transportation to alleviate the power shortage issue (Chen et al., 2024). Notably, the increased wind speed and enhanced mixing layer height (MLH) also enabled a more favorable atmospheric diffusion condition in P2, facilitating the dilution of surface air pollutants (Zhang et al., 2008). However, a higher mass concentration of SO_2 was observed in the P2 period, likely due to a surge in electricity demand and resulted higher emissions from power plants operating almost at full capacity during the heatwave (Su, 2021; Teng et al., 2022). Moreover, significant discrepancies in the aerosol optical and hygroscopic properties were observed under different synoptic conditions (Table S2). Both HBF and SAE were higher during the P2 period, aligning with the smaller R_{eff} (Table S2). The f(RH) was found to be relatively higher (p <0.05) in heatwave days, with the mean values of 1.61 ± 0.12 and 1.71 ± 0.15 during the P1 and P2 periods, respectively. Differently, ALWC was more abundant during the normally hot P1 period than the heatwave-dominated P2 period. This is likely due to that the derivation algorithm of ALWC utilized in this study (Kuang et al., 2018) was partly dependent on (e.g., positively correlated) the dry aerosol scattering coefficient, or rather the aerosol volume concentration in the dry condition (refer to Sect. S3 and Fig. S11 of the supplement). The mean $\sigma_{sca,\,525}$ for P2 was about 46.8% of that for the P1 period, and the corresponding mean level of ALWC was approximately 55.8% of that for P1. This partly agrees with the stronger aerosol optical hygroscopicity with a marginally higher f_W during the P2 period, highlighting a complex interaction between the optical enhancement and aerosol physicochemical properties.

The particle number size distribution data suggested that NPF events appeared in about half the number of observation days (Fig. 1i), with an overall occurrence frequency of 52.4% (Fig. S4a). This suggests the rather frequent summer NPF events in Chongqing, notably higher than those observed in other regions of the world, e.g., Beijing (16.7%, Deng et al., 2020; ~20%, Wang et al., 2013), Dongguan (4%, Tao et al., 2023), Hyytiälä (<40%, Dada et al., 2017) and LiLLE (<20%, Crumeyrolle et al., 2023). Moreover, the frequent NPF events during heatwaves formed substantially ultrafine particles that are of less contribution to aerosol optical properties in

comparison to large particles (Fig. S13), partially explaining the significantly lower levels of total scattering coefficients observed during the P2 period. It should be noted that the hourly $\sigma_{sca,\,525}$ values during the P2 period were exclusively below 100 Mm^{-1} (approximately the last 10th percentile of $\sigma_{sca,\,525}$ data, regarded as the threshold value of relatively polluted cases; Fig. S2c), suggesting a much cleaner environment compared to the relatively polluted P1 period. Correspondingly, NPF events occurring during the relatively polluted P1 period (as detailed in section 3.2) were defined as ~~NPF$_P$~~NPF$_{polluted}$, while cases during the cleaner and heatwave-dominated P2 period were classified as ~~NPF$_{C,\,HW}$~~NPF$_{clean,\,HW}$.

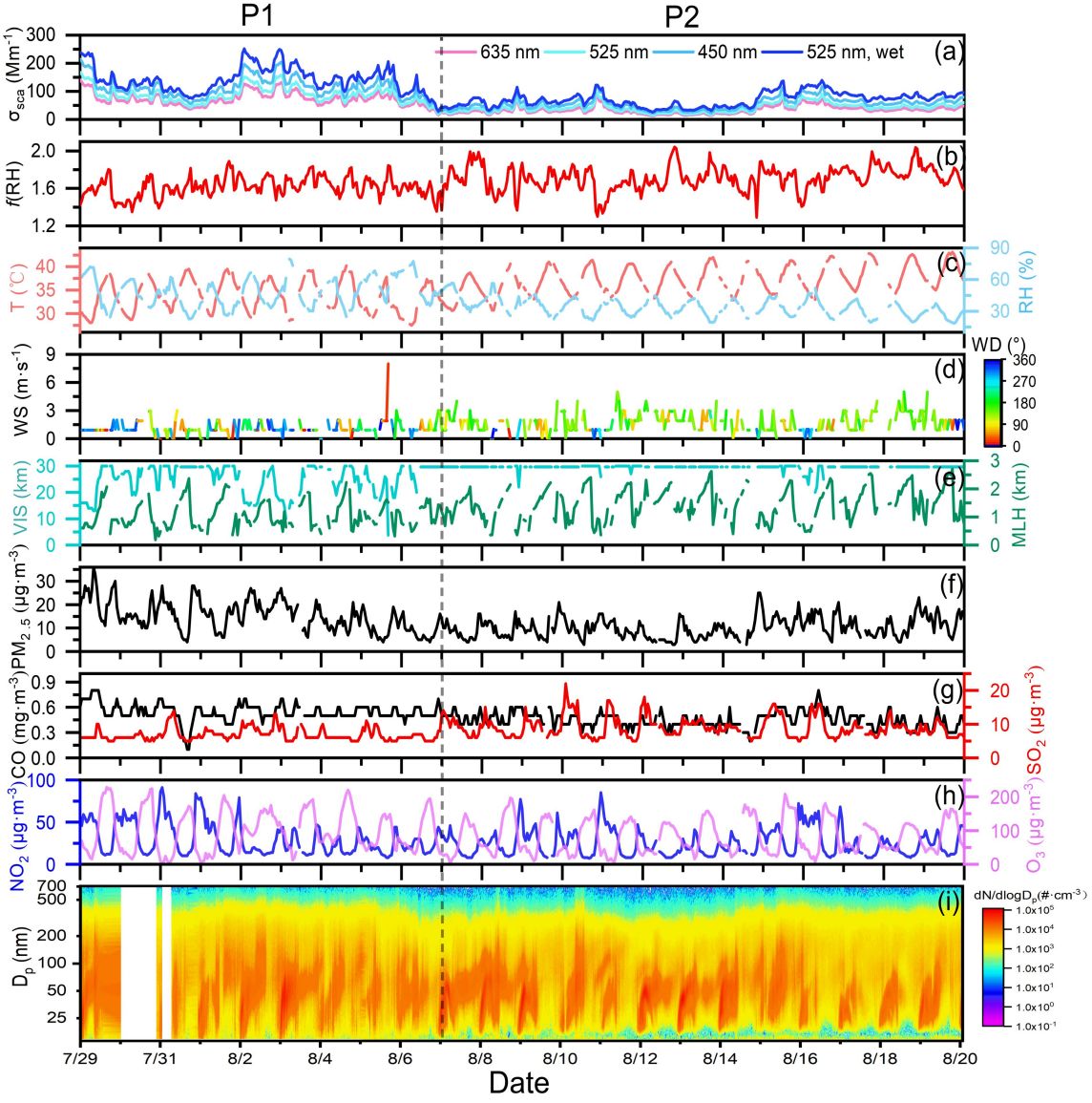

Figure 1. Time series of the measured aerosol scattering coefficients, *f*(RH), meteorological conditions, air pollutants, and particle number size distribution during the study period.

3.2 Characteristics of NPF events in different periods

Aside from gaseous precursors (e.g., SO_2, volatile organic compounds), meteorological conditions also play a key role in the occurrence of NPF events. In brief, NPF events are more likely to appear under sunny and clean conditions (Bousiotis et al., 2021; Crumeyrolle et al., 2023; Deng et al., 2021; Wang et al., 2017). The backward trajectory analysis revealed that the southerly breeze was predominant during the study period (Fig. S4b). Although the surface wind vector slightly varied between the P1 and P2 periods, this consistency in air mass origins suggests that some other factors (e.g., changes in environmental conditions and emissions of gaseous precursors under heatwaves) could have played a crucial role in modulating NPF events. To further explore the characteristics of NPF events in different periods, the time-averaged diurnal variations of meteorological parameters and air pollutant concentrations during both NPF events and non-event days are presented in Fig. 2.

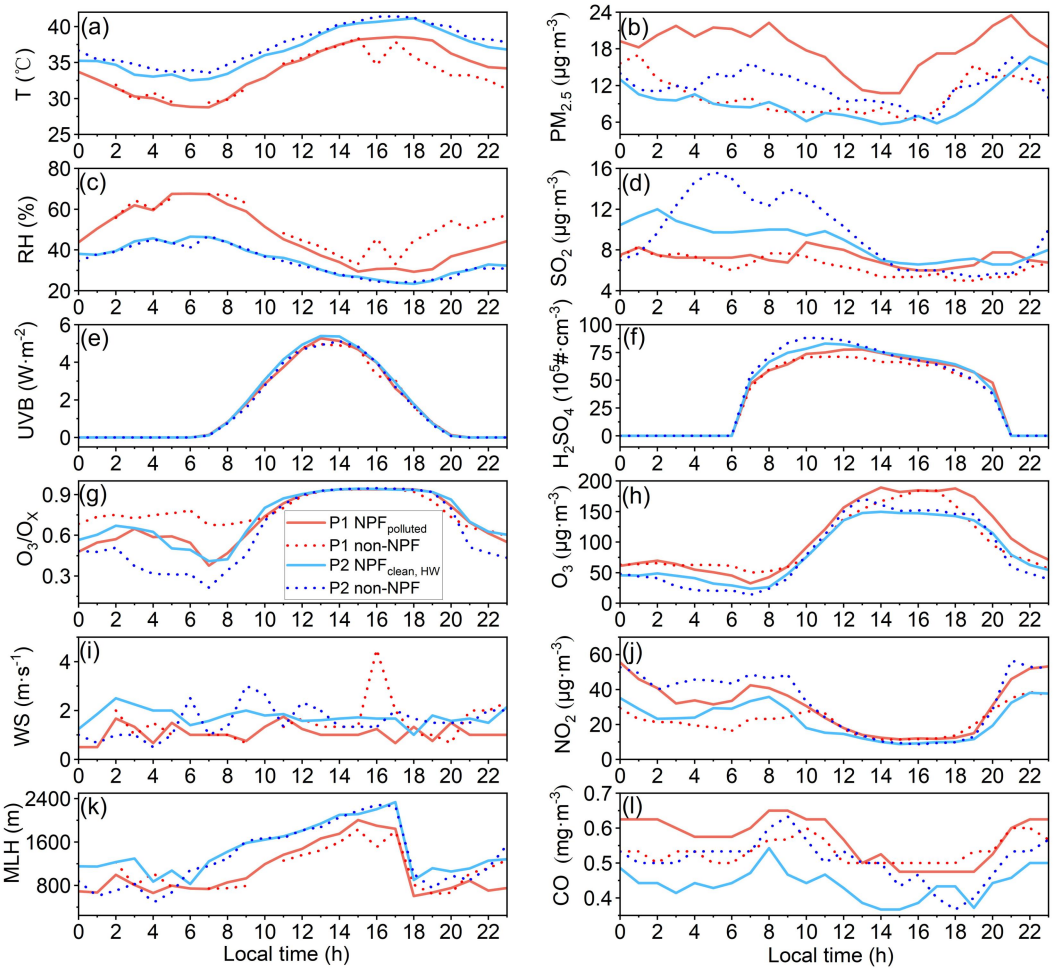
(a)
T (℃)
(b)
PM2.5 (μg·m-3)
(c)
RH (%)
(d)
SO2 (μg·m-3)
(e)
UVB (W·m-2)
(f)
H2SO4 (10^5#·cm-3)
(g)
O3/OX
P1 NPFpolluted
P1 non-NPF
P2 NPFclean, HW
P2 non-NPF
(h)
O3 (μg·m-3)
(i)
WS (m·s-1)
(j)
NO2 (μg·m-3)
(k)
MLH (m)
(l)
CO (mg·m-3)
Local time (h)
Local time (h)

305

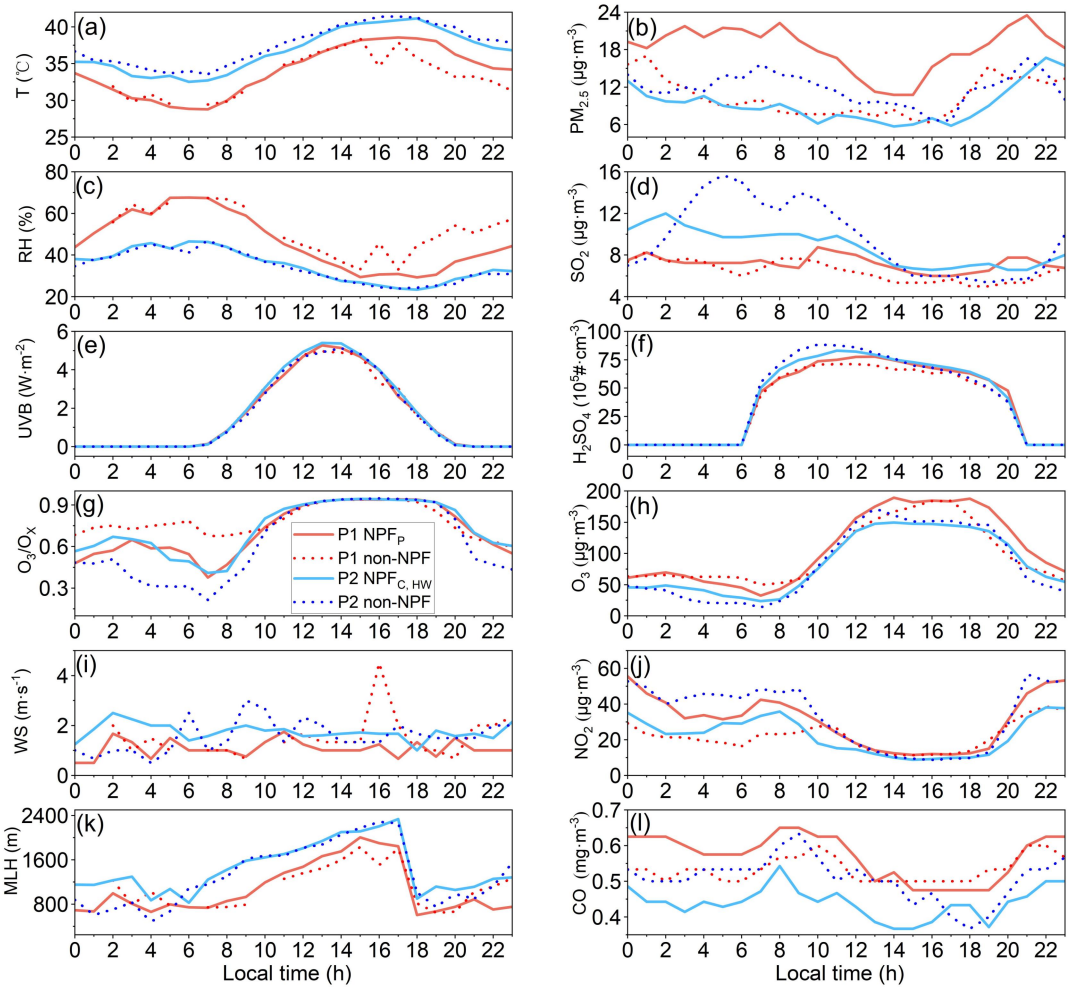

306

307 **Figure 2.** Diurnal variations of temperature **(a)**, $PM_{2.5}$ mass loading **(b)**, RH **(c)**, SO_2
308 **(d)**, UVB **(e)**, H_2SO_4 **(f)**, O_3/O_X **(g)**, O_3 **(h)**, WS **(i)**, NO_2 **(j)**, MLH **(k)** and CO **(l)**
309 during P1 (red) and P2 (blue) NPF days (solid line), as well as the corresponding
310 non-event days (dash line).

311 As stated in Sect.3.1, NPF events during the P1 period tended to occur in
312 relatively polluted environments compared to that of P2 ~~$NPF_{C,\ HW}$~~$NPF_{clean,\ HW}$ events,
313 as evidenced by the frequent occurrence of $\sigma_{sca,\ 525}$ >100 Mm^{-1}, increased air pollutant
314 concentrations and lower visibility levels during P1 (Table S2, Fig. 1). Additionally,
315 the mean CS of the ~~NPF_P~~$NPF_{polluted}$ events was above 0.015 s^{-1} (Table S2), which
316 could be considered as the "polluted" NPF cases (Shang et al., 2023). On P2 ~~$NPF_{C,\ HW}$~~
317 $NPF_{clean,\ HW}$ days, the overall mean $\sigma_{sca,\ 525}$ was 33.2 ± 11.7 Mm^{-1}, decreased by
318 68.0% (39.3%) in comparison to that for P1 ~~NPF_P~~$NPF_{polluted}$ days (P2 non-event days).
319 In addition, the mean $PM_{2.5}$ concentration was even lower than 10.0 $\mu g \cdot m^{-3}$, and the

corresponding visibility level was almost maintained at 30 km (Fig. 1e). All the above implies that the P2 ~~NPF$_{C,\ HW}$~~NPF$_{clean,\ HW}$ events were generally accompanied with a much cleaner environment. It is notable that the increase in SO_2 concentration after 9:00 LT (Fig. 2d), along with the significant decrease in $PM_{2.5}$ mass loadings after 8:00 LT during P1 ~~NPF$_P$~~NPF$_{polluted}$ events (Fig. 2b), likely favored the occurrence of NPF events. The higher gas-phase sulfuric acid (i.e., H_2SO_4, as estimated with the UVB and SO_2 concentration, Lu et al., 2019, Sect. S4) on the same NPF days (Fig. 2f), further suggesting that sulfuric acid concentration was a critical factor for the occurrence of P1 ~~NPF$_P$~~NPF$_{polluted}$ events.

The diurnal evolutions of meteorological conditions (e.g., T, RH, MLH) for NPF events were distinct between P1 and P2 periods, although relatively insignificant differences were observed for both NPF days and non-event days within a same period (Fig. 2). This likely suggests that meteorological factors might not be the predominant determining factor of NPF occurrence during the heatwaves of 2022 summer in urban Chongqing, while NPF could be accompanied with quite different meteorological conditions depending on gaseous precursors and preexisting condensation sinks. For instance, the ~~NPF$_{C,\ HW}$~~NPF$_{clean,\ HW}$ events were typically of clean-type NPF, characterized with lower background aerosol loading, higher temperature and favorable atmospheric dispersion capacity with the higher MLH. However, it is reported that excessive heat can increase the evaporation rate of critical acid-base clusters during the nucleation process and reduce the stability of initial molecular clusters (Bousiotis et al., 2021; Kurtén et al., 2007; Zhang et al., 2012), in line with a recent study that NPF events were weaker during heatwaves in Siberian boreal forest due to the unstable clusters (Garmash et al., 2024). On the other hand, the emission rate of biogenic VOCs ($BVOC_S$, e.g., isoprene, monoterpene) from nearby plants and trees would decrease when temperature exceeded around 40 °C (Guenther et al., 1993; Pierce and Waldruff, 1991), despite that BVOCs plays a key role in the nucleation mechanism of NPF (Wang et al., 2017; Zhang et al., 2004). Hence, the even higher temperature (e.g., T >40 °C) likely suppressed the nucleation

processes and the subsequent growth of nucleation mode particles on P2 non-event days (Fig. S6b2), in spite of higher concentrations of SO_2 and H_2SO_4.

To further investigate the effect of heatwave on NPF events, the diurnal variations of PNSD, R_{eff} and particle mode diameter (D_{mode}) were shown in Fig. S6. Aerosol number and volume concentrations, as well as R_{eff}, for different modes were illustrated in Figs. S7-8, and the relationship between temperature and the duration of NPF events was displayed in Fig. S9. Distinct particle size distributions were observed for different NPF event days. While the number concentrations of Aitken mode particles ($N_{Ait.}$) were comparable during NPF days of both periods, the corresponding number concentration of nucleation mode ($N_{Nuc.}$) was significantly higher on P1 $NPF_{polluted}$ days (1880.8 ± 2261.5 cm^{-3}) than that for P2 NPF cases (1132.0 ± 1333.5 cm^{-3}) (Fig. 1i, Fig. S7). The reduced $N_{Nuc.}$ during P2 period was likely attributed to the influence of transport on the local nucleation process (Fig. S4; Cai et al., 2023; Lee et al., 2019). Namely, some nucleation mode particles transported from upwind regions had undergone atmospheric aging thereby a certain degree of growth upon arrival (Cai et al., 2023), resulting in relatively lower concentrations of smaller-sized particles than the case of locally formed. However, t~~T~~he NPF events under heatwaves usually initiated earlier (Fig. S~~8~~9), with the ~~number concentration of nucleation mode particles (~~$N_{Nuc.}$~~)~~ in P2 ~~$NPF_{C, HW}$~~$NPF_{clean, HW}$ cases peaked about an hour earlier in comparison to ~~NPF_P~~$NPF_{polluted}$ days (Fig. S~~7~~8a). The D_{mode} on P2 ~~$NPF_{C, HW}$~~$NPF_{clean, HW}$ days also reached its minimum earlier than that on P1 ~~NPF_P~~$NPF_{polluted}$ days (Fig. S6). Since the sunrise and sunset time did not significantly vary within the study period (i.e., less than a half hour discrepancy), heatwaves likely provided more favorable conditions (e.g., enhanced volatile gaseous emissions, low RH; Bousiotis et al., 2021; Hamed et al., 2007; Wang et al., 2024) for the occurrence of NPF events in urban Chongqing. This is supported by the earlier start time of ~~$NPF_{C, HW}$~~$NPF_{clean, HW}$ corresponding to higher temperature ranges (Fig. S~~8~~9). Furthermore, the end time of subsequent particle growth during P2 period was even later (i.e., ~ 21:00 LT) than that of P1 cases (Fig. S~~8~~9). Given that the growth rates of new particles were generally lower during P2 ~~$NPF_{C, HW}$~~$NPF_{clean, HW}$ events

(Table S2), these explosively formed new particles could persist longer in the warmer atmosphere and probably undergo aging processes with a relatively higher oxidation degree. This is supported by the commonly higher ratios of secondary organic carbon (SOC) to organic carbon (OC) (i.e., SOC/OC >0.5) during the ~~NPF$_{C,\ HW}$~~NPF$_{clean,\ HW}$ days (Fig. S3b). In addition, aerosol R_{eff} was significantly smaller on the ~~NPF$_{C,\ HW}$~~NPF$_{clean,\ HW}$ days under heatwave conditions. The R_{eff} and D_{mode} nearly kept at a same level below/approaching 50 nm during the subsequent growth on the P2 ~~NPF$_{C,\ HW}$~~NPF$_{clean,\ HW}$ days, while the R_{eff} was generally above 50 nm and larger than D_{mode} for both P1 ~~NPF$_{P}$~~NPF$_{polluted}$ cases and non-event days (Fig. S6). The diurnal patterns of aerosol volume concentrations for different size modes were similar to that of aerosol number concentrations during NPF events (Fig. S~~7~~8b1-b3). However, both the R_{eff} of Aitken mode particles ($R_{Ait.}$) and accumulation mode particles ($R_{Acc.}$) were smaller during P2 ~~NPF$_{C,\ HW}$~~NPF$_{clean,\ HW}$ events than that of P1 ~~NPF$_{P}$~~NPF$_{polluted}$ events (Fig. S~~7~~8c2-c3), which may further influence size-dependent aerosol optical and hygroscopic properties (e.g., $\sigma_{sca,\ 525}$, HBF, SAE, *f*(RH)). The decrease in $R_{Ait.}$ and $R_{Acc.}$ during heatwaves could be attributed to three factors: (1) evaporation of the outer layer of particles and unstable clusters due to heatwaves (Bousiotis et al., 2021; Cusack et al., 2013; Deng et al., 2020; Garmash et al., 2024; Li et al., 2019); (2) lower FR and GR of particles under the cleaner environment (Table S2); (3) reduced emissions of larger primary particles during the P2 period.

3.3 Characteristics of the aerosol optical and hygroscopic properties on different types of NPF days

Diurnal variations of the aerosol optical and hygroscopic parameters during different NPF days were shown in Fig. 3, and the corresponding results for non-event days can refer to Fig. S~~9~~10. Generally, $\sigma_{sca,\ 525}$ possessed a similar bimodal diurnal pattern to that of the accumulation mode aerosol volume concentration ($V_{Acc.}$) (Fig. S~~7~~8b3), as supported by the positive correlation between $\sigma_{sca,\ 525}$ and SMPS-measured aerosol volume concentration (Fig. S1~~1~~2). This is also consistent with the Mie theory, with a stronger increase in the scattering efficiency for accumulation mode particles

(Titos et al., 2021). The diurnal pattern of $\sigma_{sca,\ 525}$ also varied distinctly between different NPF days. Specifically, a minor peak of $\sigma_{sca,\ 525}$ around 12:00 LT (Fig. 3a) was influenced by the newly formed particles during P2 ~~NPF$_{C,\ HW}$~~NPF$_{clean,\ HW}$ events, which contributed more significantly to the aerosol number and volume concentrations within 100 nm size ranges in markedly clean environments (Fig. S5c1, c2). Instead of a noontime peak, $\sigma_{sca,\ 525}$ was observed with an early peak around the morning rush hours and a maximum value similarly occurred at the nighttime on P1 ~~NPF$_{P}$~~NPF$_{polluted}$ days.

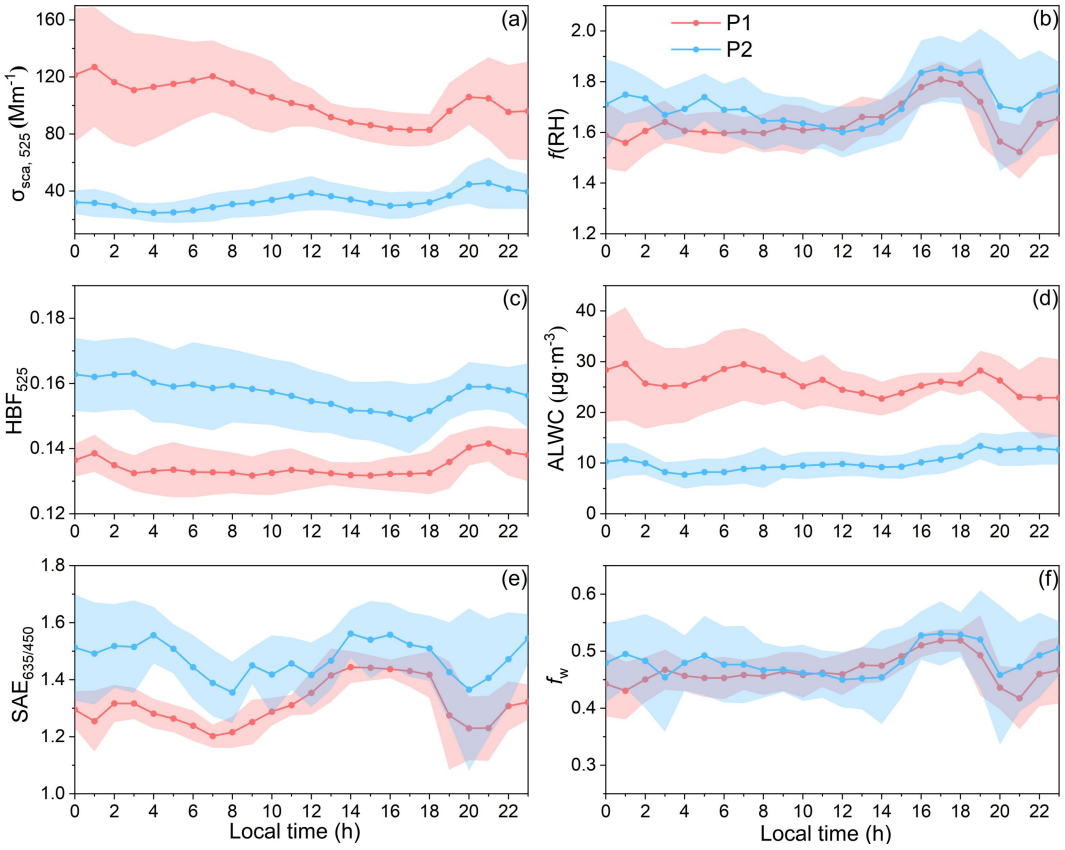

Figure 3. Diurnal variations of $\sigma_{sca,\ 525}$ **(a)**, *f*(RH) **(b)**, HBF$_{525}$ **(c)**, ALWC **(d)**, SAE$_{635/450}$ **(e)** and f_W **(f)** on NPF days during P1 (red line) and P2 (blue line) periods. The shaded areas stand for the corresponding ± 1σ standard deviations.

Both HBF and SAE on P2 ~~NPF$_{C,\ HW}$~~NPF$_{clean,\ HW}$ days were significantly higher than that of P1 ~~NPF$_{P}$~~NPF$_{polluted}$ cases (Fig. 3c, e), largely due to the smaller R_{eff} observed during heatwave-dominated period (Table S2). Moreover, the correlation between HBF (or SAE) and particle size in each mode was weaker on NPF days than

on non-event days, especially for ~~NPF$_{C,\ HW}$~~NPF$_{clean,\ HW}$ days (Fig. S1~~3~~4). A strongest negative correlation was found between HBF and R_{eff} of the accumulation mode in comparison to other modes, highlighting that HBF is more sensitive to the size distribution of accumulation mode particles (Collaud Coen et al., 2007). Given that NPF would largely enhance the abundance of both nucleation and Aitken mode aerosols (Fig. S7), no significant variation in HBF was observed during the daytime due to the weakened correlation between HBF and $R_{Acc.}$ of NPF events. SAE is commonly used as an indicator of particle size distribution, almost decreasing monotonously with the increase of aerosol size within 1 μm (Kuang et al., 2017, 2018; Luoma et al., 2019). Accordingly, SAE decreased over the morning and evening rush hours when coarse particles (e.g., aged particles, road dust, automobile exhaust) generated during anthropogenic activities, accompanied with an increase in CO that is taken as the proxy for primary emissions (Fig. 2l) (Yarragunta et al., 2020). On the contrary, the abundant ultrafine particles formed during NPF events led to a continuous increase in SAE during the day.

f(RH) exhibited a similar diurnal pattern on the P1 and P2 NPF days (Fig. 3b). During the daytime, *f*(RH) remained relatively stable and gradually increased until peaking around 16:00-18:00 LT, with a generally higher *f*(RH) particularly after 15:00 LT during P2 ~~NPF$_{C,\ HW}$~~NPF$_{clean,\ HW}$ days than that of P1 cases. The insignificant fluctuation of relatively lower *f*(RH) levels before the noon could be attributed to the continuous development of the mixing layer (Fig. 2k), leading to an efficient mixing of particles in the nocturnal residual layer with anthropogenic emissions near the ground. Additionally, photochemical reactions in the afternoon facilitated the formation of more hygroscopic secondary aerosols with a higher oxidation level (Liu et al., 2014; R. Zhang et al., 2015). The diurnal patterns of O_3 and the O_3/O_X ratio (i.e., an indicator of atmospheric oxidation capacity, where $O_X = O_3 + NO_2$, Tian et al., 2021) also showed similar trends (Fig. 2g, 2h). The presence of black carbon (BC) mixed with organic compounds (e.g., from traffic emissions and residential cooking activities) explained the rapid decrease in *f*(RH) during the evening rush hours (Liu et al., 2011). Furthermore, the daily mean *f*(RH) for NPF days was higher than that of

non-event days (Table S2), particularly after the ending of NPF events around 12:00 LT. Given that newly formed particles were too small to significantly impact the total light scattering (Fig. S1~~0~~1a), this indicates that the atmospheric conditions conducive to the occurrence of NPF may promote further growth (e.g., via photooxidation or atmospheric aging processes) of pre-existing particles and newly formed ones, leading to enhanced aerosol optical hygroscopicity as clued from the concurrent variations of ALWC and f_W in urban Chongqing during hot summer (Asmi et al., 2010; Wang et al., 2019; Wu et al., 2016). The diurnal pattern of ALWC closely mirrored the variation in $\sigma_{sca,\ 525}$, while f_W followed the similar evolution of f(RH). This suggests that ALWC was more sensitive to changes in the aerosol volume concentration, as determined by the corresponding retrieval algorithm (Kuang et al., 2018). The f_W levels were slightly higher during NPF days in comparison to that of non-event days (Table S2). This difference was more pronounced in the afternoon of NPF days (e.g., even exceeded 50%; Fig. 3f), verified the enhancement of aerosol hygroscopicity during the subsequent growth and atmospheric aging of both pre-existing and newly formed particles.

3.4 Heatwave-induced divergent changes in aerosol optical hygroscopicity

To further explore the impacts of heatwaves on f(RH) during diverse NPF events, data mainly within the time window of 08:00-22:00 LT (i.e., typically covered the complete process of NPF and subsequent growth, while excluded higher RH conditions at night) were utilized for the following discussion.

Although ultrafine particles exhibited higher number concentrations during the study period, accumulation mode particles dominated the aerosol volume concentration and contributed predominantly to the total light scattering (Figs. S7, S13). A positive correlation between f(RH), R_{eff} and the volume fraction of accumulation mode particles ($VF_{Acc.}$) was found on non-event days (Fig. 4c-d), when the aerosol size distribution was undisturbed by newly formed ultrafine particles and the corresponding $VF_{Acc.}$ maintained around a high level of 0.95 (Fig. 4a-b). The notably positive correlation between f(RH) and R_{eff} could be linked to the secondary

formation of hygroscopic particles within the accumulation mode, primarily via photochemical reactions and further intensified by heatwaves during the non-event day particularly of the P2 period (Gu et al., 2023; Liu et al., 2014; R. Zhang et al., 2015; Zhang et al., 2024). Consequently, *f*(RH) at a specific R_{eff} was generally higher during the P2 period in comparison to that of P1 (Fig. 4c-d), also with high *f*(RH) levels observed for smaller size cases of R_{eff} <110 nm under some extremely high temperature conditions (T >40 ℃, as highlighted by the red dashed circle in Fig. 4d). The higher SOC/OC on P2 non-event days further demonstrated the stronger secondary aerosol formation in comparison to P1 non-event days (Fig. S3b).

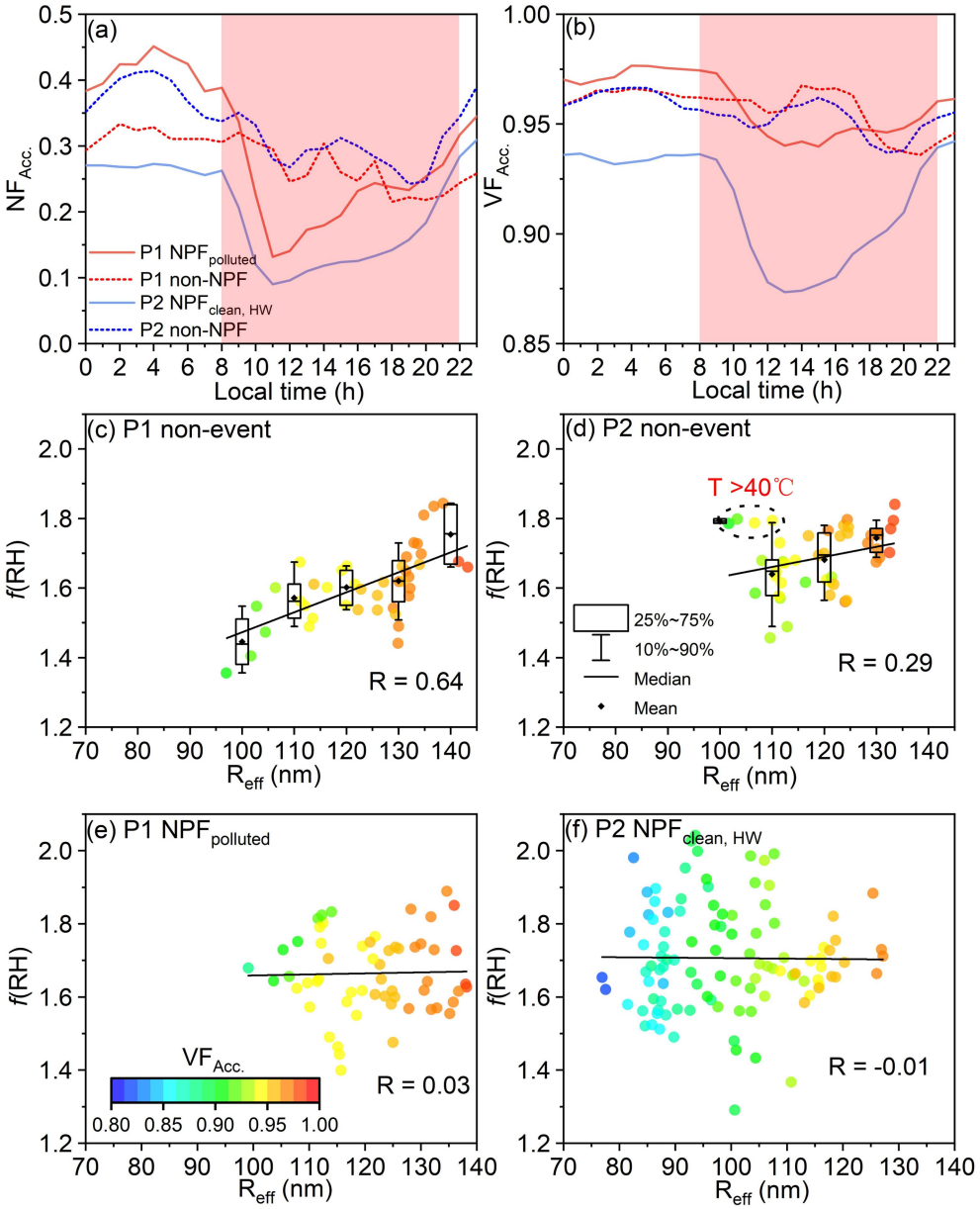

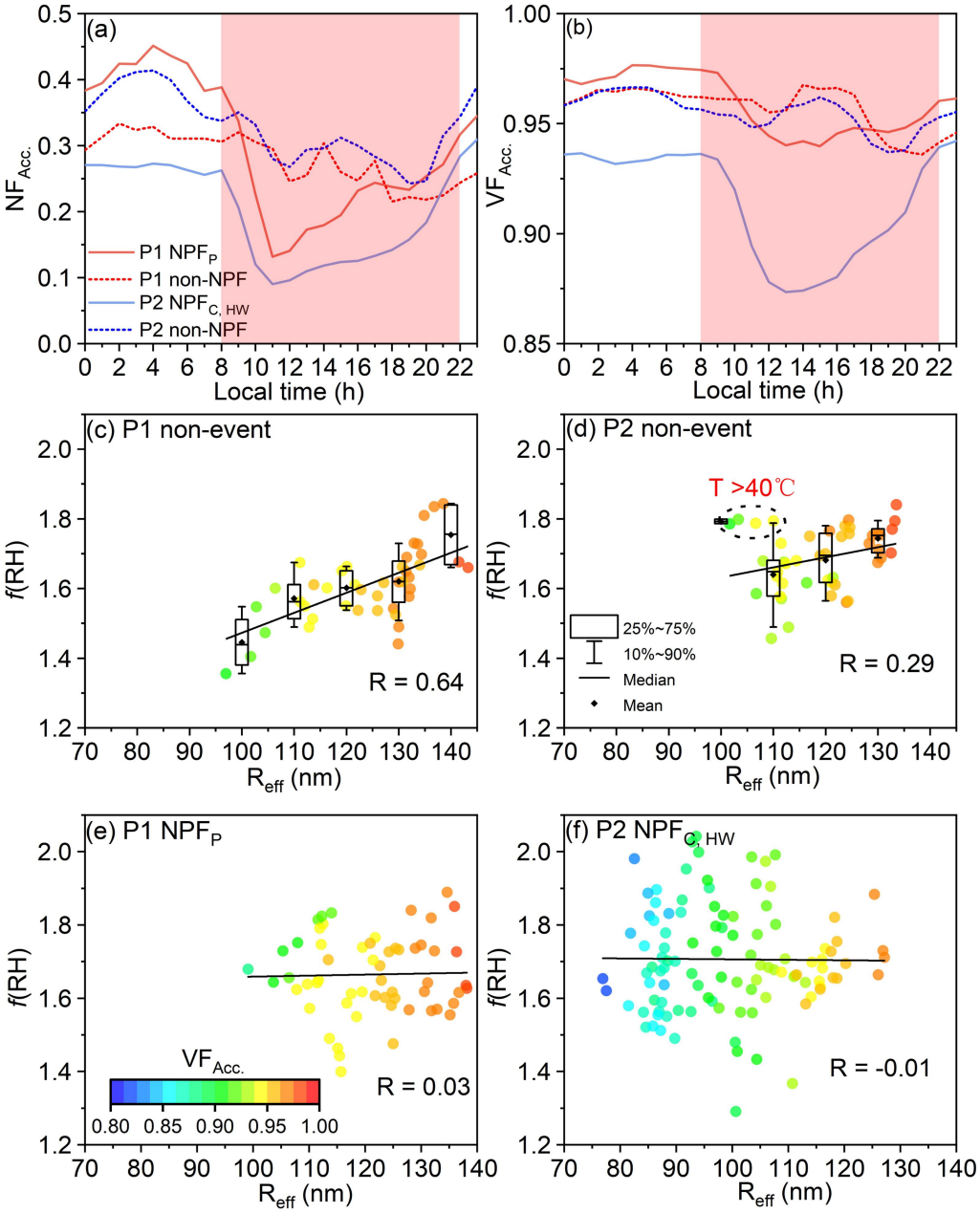

493

494 **Figure 4.** Diurnal variations of **(a)** the number fraction ($NF_{Acc.}$) and **(b)** volume
495 fraction of accumulation mode particles ($VF_{Acc.}$) on P1 (red) and P2 (blue) NPF days
496 (solid line), as well as non-event days (dash line). The time window of 08:00-22:00
497 LT was shaded in red. The relationship of *f*(RH) with R_{eff} and $VF_{Acc.}$ (as indicated by
498 the colored dots) on P1 **(c)** and P2 non-event days **(d)**, as well as on P1 **(e)** and P2 **(f)**
499 NPF days during the 08:00-22:00 LT time window.

500 Nevertheless, *f*(RH) was almost independent of the two parameters (i.e., R_{eff}
501 and $VF_{Acc.}$) for NPF events (Fig. 4e-f). This is mainly due to the explosive formation
502 of ultrafine particles and subsequent growth on NPF days, significantly altering

aerosol size distributions and inducing large fluctuations in the number and volume fractions of accumulation mode particles (as shaded in Fig. 4a-b). Therefore, characterizing *f*(RH) with the corresponding R_{eff} of aerosol populations was no longer applicable. Alternatively, SAE was commonly used to estimate or parameterize *f*(RH) (Titos et al., 2014; Xia et al., 2023; Xue et al., 2022), in line with the similar diurnal patterns of *f*(RH) and SAE observed in this study. Figure 5 demonstrated a significantly positive correlation between *f*(RH) and SAE during NPF days in comparison to non-event days, with a similar slope of approximately 0.65 suggesting the consistent variation of *f*(RH) with SAE across both periods. As larger particles contributed higher to the aerosol volume concentrations (Fig. S5), the decrease of SAE also corresponded to an increase in $\sigma_{sca,\ 525}$ (Fig. 5a3, b3). Given that larger $\sigma_{sca,\ 525}$ values typically indicate the condition of a higher aerosol loading, *f*(RH) increased with SAE whereas decreased with $\sigma_{sca,\ 525}$, or rather the pollution level, during NPF days. The cleaner environment of P2 period ~~generally possessed a lower CS (Table S2, as denoted by the size of circles in Fig. 5a2, b2), thereby~~may further ~~in favor of~~ the occurrence of NPF events. ~~Aerosol~~ Both *f*(RH) and SAE exhibited a higher level on P2 ~~$NPF_{C,\ HW}$~~$NPF_{clean,\ HW}$ days (as shown by the dash lines in Fig. 5), ~~the possible reasons can be~~likely attributed to the following two aspects. One is related to the smaller aerosol R_{eff} (with a larger SAE) due to the lower FR and GR, likely influenced by the evaporation of newly-formed unstable clusters and particle coatings under heatwaves (Bousiotis et al., 2021; Cusack et al., 2013; Deng et al., 2020) during the subsequent growth of aerosols. Secondly, the higher temperature was normally associated with stronger photochemical oxidation, which could intensify the formation of secondary aerosol components with a higher hygroscopicity (Asmi et al., 2010; Gu et al., 2023; Liu et al., 2014; Wu et al., 2016; R. Zhang et al., 2015; Zhang et al., 2024). This is further supported by the slightly higher levels of UVB (P1: 2.6 ± 1.9 $W \cdot m^{-2}$ versus P2: 2.7 ± 2.0 $W \cdot m^{-2}$) and O_3/O_X (P1: 0.81 ± 0.17 versus P2: 0.82 ± 0.17) during P2 heatwave days, also in line with a recent study which demonstrated that heatwaves affected secondary organic aerosols (SOA) formation and aging by accelerating photooxidation in Beijing (Zhang et al., 2024).

It is worth noting that *f*(RH) did not show a consistently higher level after the ~~NPF$_{C,\ HW}$~~NPF$_{clean,\ HW}$ occurrence during P2 period, and it was slightly higher within the first few hours of NPF occurrence (i.e., ~ 12:00 -15:00 LT) on P1 ~~NPF$_P$~~NPF$_{polluted}$ days (Fig. 3b). In fact, aerosol optical hygroscopicity not fully corresponds to the bulk hygroscopicity primarily determined by aerosol chemical components, and the variability in aerosol optical features also plays a key role in *f*(RH). Hence, the size-dependency of aerosol optical properties should be considered. The size-resolved $\sigma_{sca,\ 525}$ distribution and size-resolved cumulative frequency distribution (CFD) of $\sigma_{sca,\ 525}$ over different NPF days were calculated using the Mie theory, with good agreements between the theoretically calculated and measured $\sigma_{sca,\ 525}$ values (R^2 = 0.99). As shown in Fig. S1~~0~~1a and Fig. S1~~2~~3, new particles must grow into the accumulation mode size at least before they can exert a significant influence on the total scattering coefficient. The critical sizes corresponding to the cumulative frequency of 50% in $\sigma_{sca,\ 525}$ were 358.7 nm and 333.8 nm on P1 and P2 NPF days, respectively. This indicates that relatively smaller particles including the newly formed and grown ones mixed with pre-existing and aged particles contributed a slightly higher portion to $\sigma_{sca,\ 525}$ on P2 ~~NPF$_{C,\ HW}$~~NPF$_{clean,\ HW}$ days, while the $\sigma_{sca,\ 525}$ was mainly contributed by larger ones on P1 ~~NPF$_P$~~NPF$_{polluted}$ days. Nevertheless, the Mie theory suggests that these smaller particles generally have a weaker enhancement in total scattering after hygroscopic growth, in comparison to larger size particles (Collaud Coen et al., 2007, Fig. S1~~0~~1a). Consequently, the changes in aerosol optical and hygroscopic properties necessitate consideration of both aerosol optical and chemical characteristics during different NPF events. Newly formed ultrafine particles contributed minor to aerosol optical properties, resulting in a lower *f*(RH) during the initial hours of P2 ~~NPF$_{C,\ HW}$~~NPF$_{clean,\ HW}$ events compared to that of P1 ~~NPF$_P$~~NPF$_{polluted}$ events (Fig. 3b), as evidenced by a smaller R_{eff} for P2 ~~NPF$_{C,\ HW}$~~NPF$_{clean,\ HW}$ events (Fig. S6). In contrast, the growth of pre-existing and newly formed particles into larger sizes would subsequently affect bulk aerosol optical properties, which was evidenced by the enhancement in aerosol extinction coefficient observed after NPF occurrence in a recent study (Sun et al., 2024). Specifically, particles could undergo a

longer and more intensified photochemical aging process during ~~NPF$_{C, HW}$~~NPF$_{clean, HW}$ events as influenced by persistent heatwaves, which facilitated the secondary formation of hygroscopic aerosols and resulted in a higher *f*(RH) after 15:00 LT (Fig. 3b).

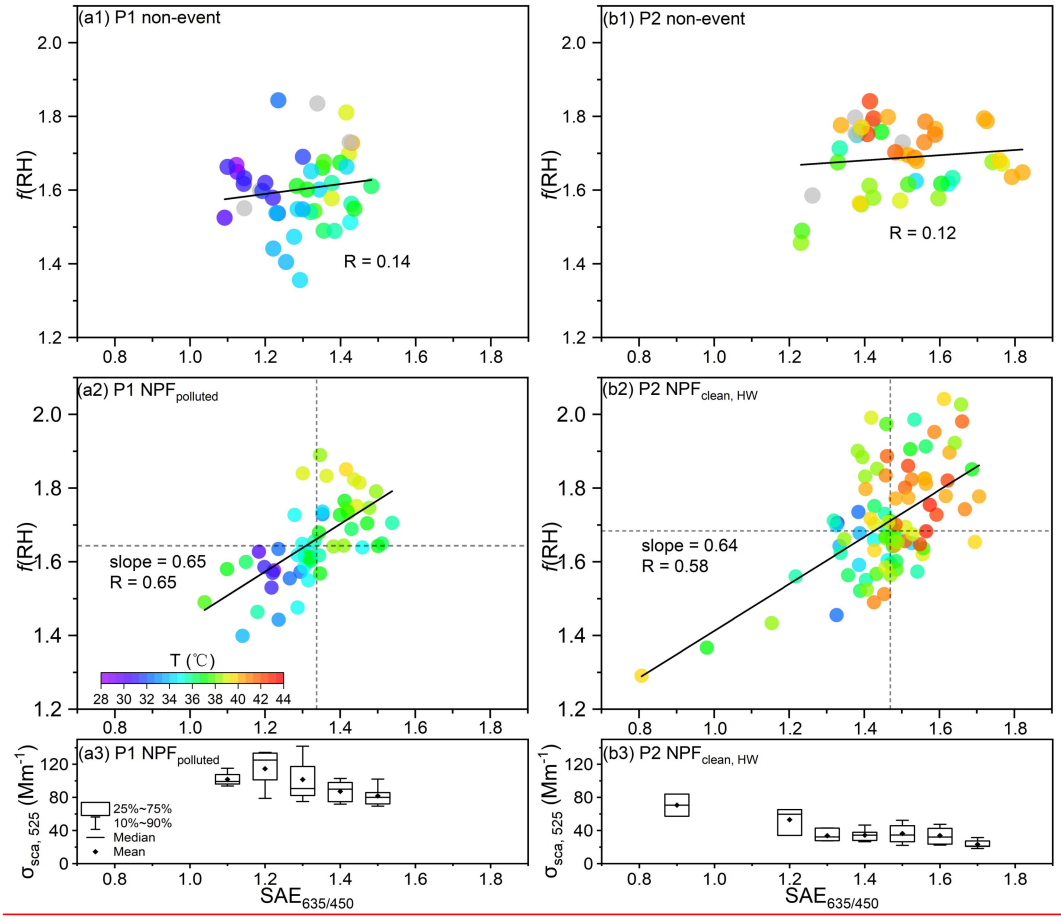

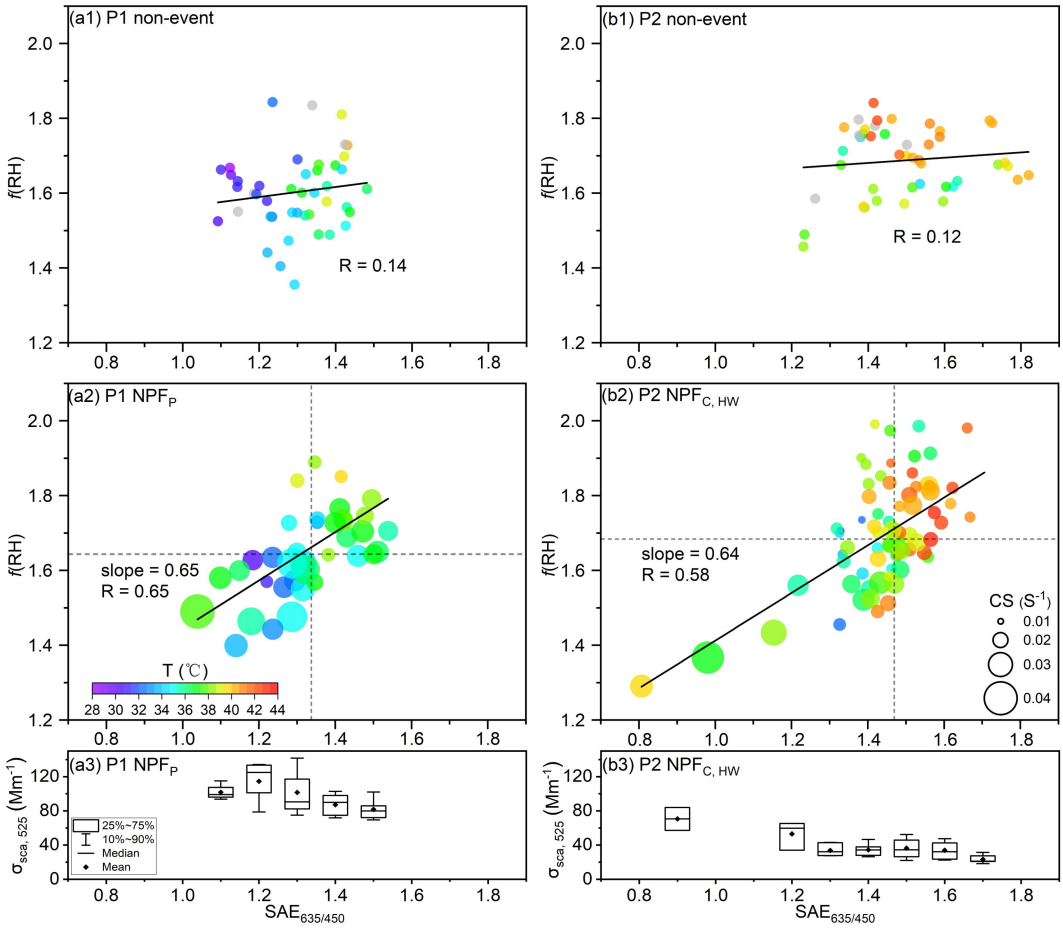

Figure 5. The relationship between *f*(RH) and $SAE_{635/450}$, as well as temperature (as indicated by the color of dots, missing values are represented in gray) ~~and CS (as denoted by the size of circles)~~, on P1 non-event days **(a1)**, ~~NPF_P~~$NPF_{polluted}$ days **(a2)** during the 08:00-22:00 LT time window. The vertical (horizontal) dash line represents the median value of $SAE_{635/450}$ (*f*(RH)). **(a3)** The corresponding $\sigma_{sca, 525}$ under different $SAE_{635/450}$ levels on P1 ~~NPF_P~~$NPF_{polluted}$ days. **(b1-b3)** The same but for P2 period.

3.5 *f*(RH)-induced changes in aerosol direct radiative forcing

The changes in *f*(RH) have significant implications for aerosol direct radiative forcing. Despite considerably lower $\sigma_{sca, 525}$ results during heatwaves, the corresponding mean f_{RF}(RH) levels particularly for P2 ~~$NPF_{C, HW}$~~$NPF_{clean, HW}$ days were higher than that of the P1 cases (Fig. 6a). A robust positive correlation ($R^2 = 0.68$) was observed between *f*(RH) and aerosol radiative forcing enhancement factor, f_{RF}(RH) (Fig. 6b). This is likely attributed to the enhanced f_{RF}(RH) with the larger forward scattering ratio β, or rather higher HBF for smaller particle sizes, as supported by a

generally negative correlation between f_{RF}(RH) and R_{eff}. Specifically, the highest f_{RF}(RH) value of 2.21 ± 0.23 was observed on P2 ~~NPF$_{C,\ HW}$~~NPF$_{clean,\ HW}$ days, characterized with the highest f(RH) and smallest R_{eff} (i.e., highest HBF) of the entire study period.

The definition of f_{RF}(RH) in Eq.(5) implies the dependences of f_{RF}(RH) on both f(RH) and HBF-derived β(RH) and β(dry), or rather the ratio of $HBF_{525,\ RH}/HBF_{525}$. The mean $HBF_{525,\ RH}$ was generally larger than HBF_{525} in this study, specifically with the $HBF_{525,\ RH}/HBF_{525}$ ratios centered around 1.8 and even approached 2.5 on P2 ~~NPF$_{C,\ HW}$~~NPF$_{clean,\ HW}$ days (Fig. 6c, Table S2). This could be different from the classical Mie theory with the spherical-particle premise, i.e., the observed light backscattering was enhanced after hydration likely resulted from the evolution in particle morphology that significantly influences their optical properties (Mishchenko 2009). Additionally, the predominant organic components when heterogeneously mixed with diverse chemical compositions (e.g., inorganics and black carbon) likely introduced the heterogeneity in aerosol hygroscopicity (Yuan and Zhao, 2023), which may alter particle morphology thereby optical properties upon water uptake (Giordano et al., 2015; Tan et al., 2020; Tritscher et al., 2011). ~~The organic-rich particles might remain non-spherical even after water uptake due to t~~The efficient evaporation of organic coatings under extremely hot conditions could also contribute to the change in particle morphology (e.g., non-spherical inregular shapes) upon humidification, as evidenced by a recent study that high temperature conditions could accelerate the evaporation rate of SOA (Li et al., 2019). Given that the backward scattering intensity of non-spherical particles is suggested to be much larger than its spherical counterparts at scattering angles between 90° and 150° (Mishchenko 2009; Yang et al., 2007) and that the HBF-derived asymmetry parameter (g) normally correlates positively with the aerosol forward scattering (Andrews et al., 2006; Marshall et al., 1995), the generally smaller g_{RH} results (in comparison to g) confirmed the decrease (increase) in the forward (backward) light scattering after water uptake (Fig. S1~~0~~1~~b~~c), likely implying the change in the morphological structure of particles. This is particularly evident for P2 ~~NPF$_{C,\ HW}$~~NPF$_{clean,\ HW}$ days, with a much lower level of g_{RH}

was observed (Fig. S10~~1~~1~~bc~~). Another possible reason is the distinct size dependences of both light scattering and backscattering efficiencies (Fig. S11a), with much more significant enhancements in the backscattering efficiency thereby HBF specifically of accumulation mode particles after hygroscopic growth (Fig. S11b). ~~that~~ As reflected by the Mie model, although the abundant newly formed particles were generally optically-insensitive (e.g., below 100 nm), their contributions to $\sigma_{sca,\ 525}$ and especially to $\sigma_{bsca,\ 525}$ could be amplified upon humidification (Fig. S11b). ~~Namely, even if these hydrated particles remained small (e.g., below 100 nm), their HBF was significantly higher than that of larger particles (Fig. S10a), thereby elevating the corresponding $HBF_{525,\ RH}$ levels during NPF events.~~ Besides, the shift of size distribution towards larger accumulation-mode particles could also result in a significant elevation in $HBF_{525,\ RH}/HBF_{525}$ ratios, especially under the condition of a smaller mode diameter and narrower distribution of ultrafine-mode particles (e.g., during NPF events) (Fig. S15a1-b2 for the theoretical sensitivity tests of Sect. S9 in the supplement). Furthermore, the $HBF_{525,\ RH}/HBF_{525}$ ratio exhibited a significant positive correlation with the real part of complex refractive index (n) of bulk aerosols (Fig. S16), and n tends to increase with the aging process of organic species (Moise et al., 2015; Zhao et al., 2021). In this sense, the evolution of both aerosol size distribution pattern and chemical compositions, combined with the heterogeneity in aerosol hygroscopicty,~~These combined effects~~ could potentially change particle morphology and optical properties (e.g., complex refractive index and elevated ~~the~~ $HBF_{525,\ RH}$) particularly during heatwave-influenced ~~$NPF_{C,\ HW}$~~$NPF_{clean,\ HW}$ days, characterized with the smallest aerosol R_{eff} (102.8 ± 12.4 nm) (Figure. S6), lowest number concentration (1897.0 ± 680.8 cm^{-3}) and fraction (0.20 ± 0.10) of accumulation mode particles ~~(0.20 ± 0.10)~~, intensified photooxidation, and a higher SOC/OC ratio. The higher $HBF_{525,\ RH}/HBF_{525}$ ratios increased the HBF-derived β(RH)/β(dry) levels, in combination of the elevated f(RH), further resulting in the highest f_{RF}(RH) observed during P2 ~~$NPF_{C,\ HW}$~~$NPF_{clean,\ HW}$ events. Given that previously observed $HBF_{525,\ RH}$ was typically lower than HBF_{525} (Titos et al., 2021; Xia et al., 2023; L. Zhang et al., 2015), the mean f_{RF}(RH) results of this study (f_{RF}(85%) = 2.05 ± 0.24) were significantly higher than

those observed in the Yangtze River Delta (f_{RF}(85%) = 1.5, L. Zhang et al., 2015), the North China Plain (f_{RF}(80%) = 1.6 ± 0.2, Xia et al., 2023), and some other regions in the world (Titos et al., 2021, Fig. 6d). It should be noted that the reported f_{RF}(RH) for the UGR site (Spain) was even higher, likely due to the higher R_s and α_s used in the derivation of f_{RF}(RH) in that area (Titos et al., 2021).

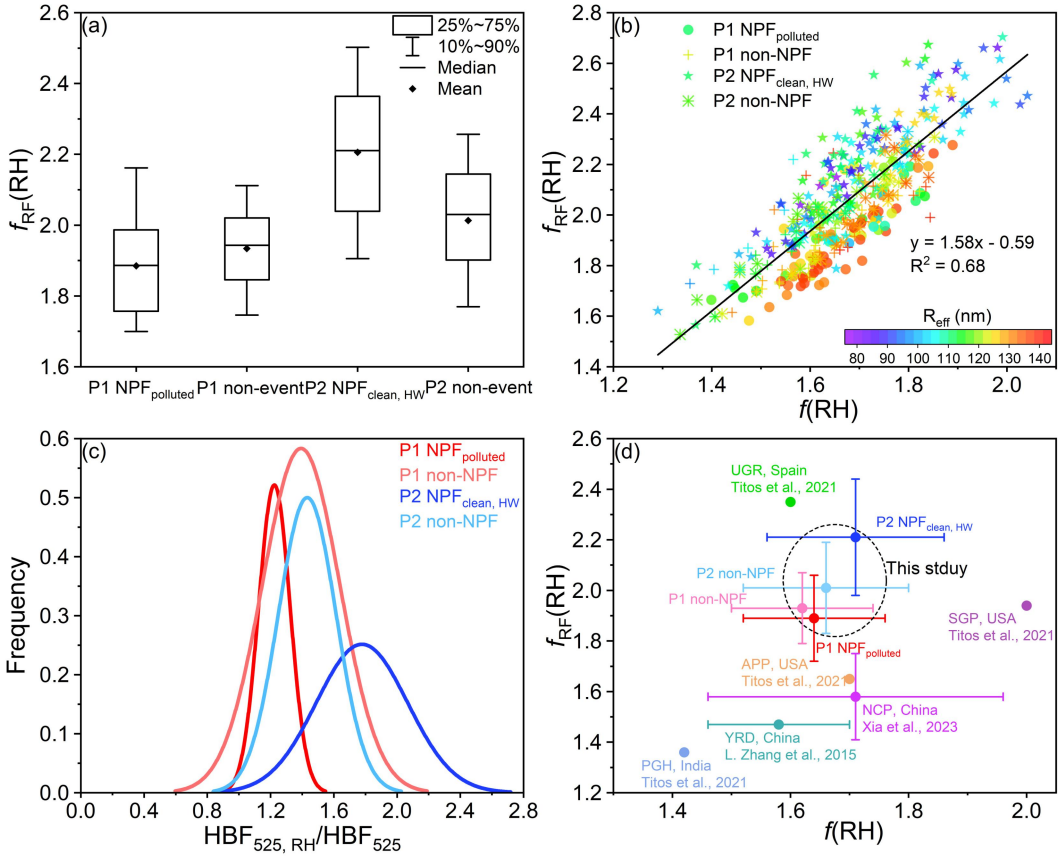
(a)
25%~75%
10%~90%
Median
Mean
f_{RF}(RH)
P1 NPF$_{polluted}$
P1 non-event
P2 NPF$_{clean, HW}$
P2 non-event
(b)
P1 NPF$_{polluted}$
P1 non-NPF
P2 NPF$_{clean, HW}$
P2 non-NPF
y = 1.58x - 0.59
R^2 = 0.68
R_{eff} (nm)
80 90 100 110 120 130 140
f(RH)
(c)
P1 NPF$_{polluted}$
P1 non-NPF
P2 NPF$_{clean, HW}$
P2 non-NPF
Frequency
HBF$_{525, RH}$/HBF$_{525}$
(d)
UGR, Spain
Titos et al., 2021
P2 NPF$_{clean, HW}$
This stduy
P2 non-NPF
P1 non-NPF
P1 NPF$_{polluted}$
SGP, USA
Titos et al., 2021
APP, USA
Titos et al., 2021
NCP, China
Xia et al., 2023
YRD, China
L. Zhang et al., 2015
PGH, India
Titos et al., 2021
f_{RF}(RH)
f(RH)

648

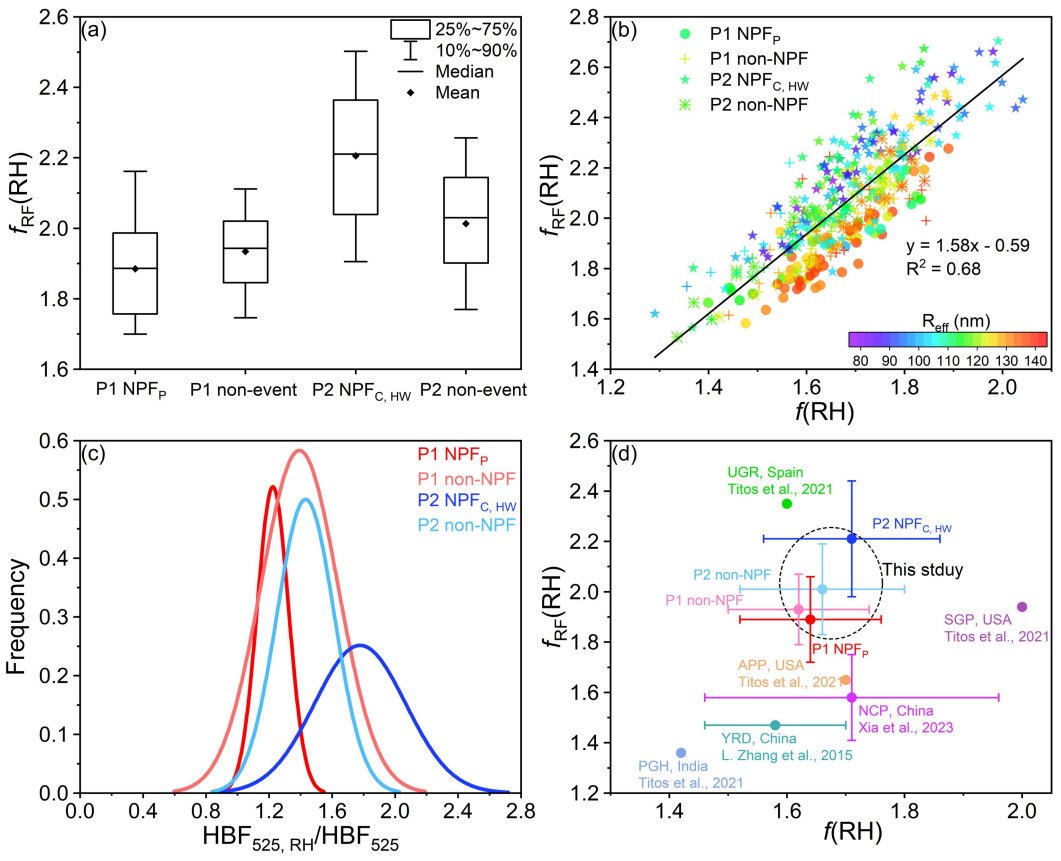
(a)
25%~75%
10%~90%
Median
Mean
f_{RF}(RH)
P1 NPF$_P$
P1 non-event
P2 NPF$_{C, HW}$
P2 non-event
(b)
P1 NPF$_P$
P1 non-NPF
P2 NPF$_{C, HW}$
P2 non-NPF
y = 1.58x - 0.59
R^2 = 0.68
R_{eff} (nm)
80 90 100 110 120 130 140
f(RH)
(c)
P1 NPF$_P$
P1 non-NPF
P2 NPF$_{C, HW}$
P2 non-NPF
Frequency
HBF$_{525, RH}$/HBF$_{525}$
(d)
UGR, Spain
Titos et al., 2021
P2 NPF$_{C, HW}$
This stduy
P2 non-NPF
P1 non-NPF
P1 NPF$_P$
SGP, USA
Titos et al., 2021
APP, USA
Titos et al., 2021
NCP, China
Xia et al., 2023
YRD, China
L. Zhang et al., 2015
PGH, India
Titos et al., 2021
f_{RF}(RH)
f(RH)

649

Figure 6. (a) The box-plot of f_{RF}(RH) during P1 or P2 NPF event and non-event days. **(b)** The relationship between f_{RF}(RH) and f(RH), as colored by the corresponding R_{eff}, during P1 or P2 NPF and non-event days (shown in different symbols). **(c)** Occurrence frequency of the $HBF_{525,\ RH}/HBF_{525}$ ratios during P1 or P2 NPF and non-event days. **(d)** The mean f_{RF}(RH) under different f(RH) levels (the error bars stand for ± one standard deviations corresponding to f_{RF}(RH) and f(RH), respectively), along with the reported f_{RF}(RH) and f(RH) data for other regions in the world.

A recent study has indicated that continuous reduction of $PM_{2.5}$ mass loadings can increase the net solar radiation, thereby promoting NPF events (Zhao et al., 2021). Given the complexity and dynamic evolution of the atmospheric environment, these can further alter the intrinsic properties of aerosol particles (e.g., f(RH), HBF, morphology), potentially feeding back into aerosol-radiation interactions. Our findings suggest that NPF and growth events may elevate aerosol optical hygroscopicity in rather hot environments, e.g., the Basin area and tropical regions. Meanwhile, NPF serves as a crucial secondary transformation process in the atmosphere (Zhu et al., 2021). The favorable atmospheric diffusion capability ensured the mixing of newly formed particles into the upper boundary layer, where is colder and more humid than that near the surface during heatwaves (Jin et al., 2022). Hence, the enhancement of aerosol optical hygroscopicity during the subsequent growth of pre-existing and newly formed particles possibly exacerbates secondary pollution and even triggers haze events (Hao et al., 2024; Kulmala et al., 2021). On the other hand, a large number of studies have demonstrated that the new particles of higher hygroscopicity could contribute more to the activation of CCN (Ma et al., 2016; Ren et al., 2021; Rosati et al., 2022; Sun et al., 2024; Wu et al., 2015), thereby modulating the aerosol-cloud interactions and further the global climate (Fan et al., 2016; Merikanto et al., 2006; Westervelt et al., 2013). Additionally, the simultaneous decrease in aerosol effective radius and possibly evaporation-induced non-spherical particle morphology further enhance the aerosol direct radiative forcing enhancement factor, potentially amplifying the cooling effect mainly caused by light scattering

aerosols. This highlights the needs for further in-depth exploration on aerosol radiative impacts at weather extremes (e.g., heatwaves) with the changing climate, given the continuous reductions of anthropogenic emissions and more intense emissions of biogenic origins with the global warming. Besides, more detailed information on the evolution of particle morphology with the changing environment (e.g., varied temperature and RH) would enrich insights into the aerosol radiative forcing.

4 Conclusions and implications

A rare heatwave event raged throughout urban Chongqing of southwest China in the summer of 2022, which significantly influenced aerosol physicochemical properties and atmospheric processes (e.g., NPF and subsequent growth). Concurrent measurements of aerosol optical and hygroscopic properties, PNSD, and bulk chemical compositions were conducted to explore the mechanisms behind the variations in aerosol optical hygroscopicity during different NPF days under diverse weather conditions.

NPF events exhibited distinct characteristics during the normally hot (P1, relatively polluted) and heatwaves-dominated (P2, quite clean) periods. ~~NPF$_P$~~NPF$_{polluted}$ within P1 period was favored by the decrease in background aerosol loading and the higher abundance of H_2SO_4. ~~NPF$_{C,\ HW}$~~NPF$_{clean,\ HW}$ events that occurred during the heatwave P2 period were characterized with lower CS, CoagS, FR and GR, as well as smaller R_{eff} and D_{mode}, than P1 ~~NPF$_P$~~NPF$_{polluted}$ cases. In comparison to the P1 ~~NPF$_P$~~NPF$_{polluted}$ events, ~~NPF$_{C,\ HW}$~~NPF$_{clean,\ HW}$ occurred approximately one hour earlier and the subsequent growth was longer during P2, likely intensifying the photochemical oxidation due to heatwave-influenced aging processes and modulating the evolution of aerosol size distributions differently. Furthermore, significant differences in aerosol optical and hygroscopic properties were observed between the normally hot and heatwave-dominated NPF days. The newly formed and grown

particles mixed with pre-existing aerosols contributed a minor $\sigma_{sca,\ 525}$ noontime peak occurred on the much cleaner P2 ~~NPF$_{C,\ HW}$~~NPF$_{clean,\ HW}$ days, while the $\sigma_{sca,\ 525}$ peaked earlier around the morning rush hours on P1 ~~NPF$_{P}$~~NPF$_{polluted}$ days. HBF and SAE were significantly higher on P2 ~~NPF$_{C,\ HW}$~~NPF$_{clean,\ HW}$ days, primarily due to the smaller R_{eff} for heatwave-influenced ~~NPF$_{C,\ HW}$~~NPF$_{clean,\ HW}$ cases. *f*(RH) remained relatively stable during the daytime of NPF days and peaked around 16:00-18:00 LT. Specifically, aerosol optical hygroscopicity tended to be higher during the subsequent growth and aging of both pre-existing particles and newly formed ones on P2 ~~NPF$_{C,\ HW}$~~NPF$_{clean,\ HW}$ days than that for P1 ~~NPF$_{P}$~~NPF$_{polluted}$ days, which aligned with the higher f_W levels.

Compared with non-event cases, the generally higher levels of daily mean *f*(RH) suggested that the aerosol optical hygroscopicity was enhanced on NPF days in hot summer of urban Chongqing. A significantly positive (negative) correlation between *f*(RH) and SAE (~~CS,~~ $\sigma_{sca,\ 525}$, or rather the pollution level) was observed on NPF days for both periods, accompanied by higher *f*(RH) and SAE values on ~~NPF$_{C,\ HW}$~~NPF$_{clean,\ HW}$ days. This was likely due to the evaporation of both unstable clusters and particle coatings under heatwaves (Bousiotis et al., 2021; Cusack et al., 2013; Deng et al., 2020; Garmash et al., 2024), thereby reducing aerosol sizes (e.g., R_{eff}, D_{mode}) whereas increasing SAE. Moreover, heatwave-influenced stronger photooxidation enhanced the formation of more hygroscopic secondary components during the subsequent growth/aging processes of both pre-existing and newly formed particles on P2 ~~NPF$_{C,\ HW}$~~NPF$_{clean,\ HW}$ days in comparison to that of P1 ~~NPF$_{P}$~~NPF$_{polluted}$ cases. The aerosol light scattering or volume concentration was mainly contributed by the larger accumulation-mode particles, while more ultrafine particles dominated the size distribution especially for the initial stage of heatwave-influenced ~~NPF$_{C,\ HW}$~~NPF$_{clean,\ HW}$ events, further leading to a lower *f*(RH) following the NPF occurrence (i.e., ~ 12:00 -15:00 LT) in comparison to P1 ~~NPF$_{P}$~~NPF$_{polluted}$ days.

Changes in *f*(RH) could potentially impact the aerosol direct radiative forcing. A robust positive (negative) correlation existed between f_{RF}(RH) and *f*(RH) (R_{eff}). Despite a lower $\sigma_{sca,\ 525}$ during heatwaves, the corresponding mean f_{RF}(RH) was

relatively higher and the maximum value of 2.21 ± 0.23 was observed on P2 ~~NPF$_{C,\ HW}$~~NPF$_{clean,\ HW}$ days, associated with the highest *f*(RH) (1.71 ± 0.13), smallest R_{eff} (102.8 ± 12.4 nm), and highest $HBF_{525,\ RH}/HBF_{525}$ ratios (1.78 ± 0.29). The above highlights that heatwaves could influence the NPF (e.g., the evolution in the aerosol size distribution pattern and chemical composition) and atmospheric processing (although with a decreased aerosol R_{eff} and D_{mode} likely due to evaporation-resulted non-spherical particle morphology under persistently high temperature conditions), thereby enhancing aerosol optical hygroscopic growth and potentially reducing the net solar radiation directly especially in hot summer. Further explorations on detailed molecular-scale characterizations (e.g., molecular structures and compositions of newly and secondary formed particles, as well as particle morphology) and aerosol radiative impacts including the aerosol-cloud interactions of weather extremes (e.g., heatwaves) with the changing climate are highly recommended.

Data availability. Data will be available upon request.

Author contributions. YH and PL: Methodology, Investigation, Data analysis, Formal analysis, Visualization, Validation, Writing – original draft & editing. YG and ZW: Methodology, Investigation, Formal analysis. MT, YC, HX and WH: Data curation, Methodology. FW and YL: Investigation. YK: Methodology, Data analysis, Writing – review & editing. JC: Conceptualization, Methodology, Funding acquisition, Data curation, Writing – review & editing, Supervision.

Competing interests. The authors declare no competing financial interest.

Acknowledgement. This work was supported by the National Natural Science Foundation of China (No. 42105075), Venture and Innovation Support Program for Chongqing Overseas Returnees (No. cx2021021). We thank Biao Xue for the

technical support on the utilization and maintenance of the humidified nephelometer system. We also thank Ziqian Wang for the TSP filter sample collection and Jiawei Zhou for the corresponding offline chemical analysis.

References

An, J., Lu, Y., Huang, D. D., Ding, X., Hu, Q., Yan, R., Qiao, L., Zhou, M., Huang, C., Wang, H., Fu, Q., Yu, F., and Wang, L.: Sectoral Size - Resolved Particle Number Emissions With Speciation: Emission Profile - Based Quantification and a Case Study in the Yangtze River Delta Region, China, J. Geophys. Res. Atmos., 1–22, https://doi.org/10.1029/2024JD041234, 2024.

Andrews, E., Sheridan, P. J., Fiebig, M., McComiskey, A., Ogren, J. A., Arnott, P., Covert, D., Elleman, R., Gasparini, R., Collins, D., Jonsson, H., Schmid, B., and Wang, J.: Comparison of methods for deriving aerosol asymmetry parameter, J. Geophys. Res. Atmos., 111, 1–16, https://doi.org/10.1029/2004JD005734, 2006.

Asmi, E., Frey, A., Virkkula, A., Ehn, M., Manninen, H. E., Timonen, H., Tolonen-Kivimäki, O., Aurela, M., Hillamo, R., and Kulmala, M.: Hygroscopicity and chemical composition of antarctic sub-micrometre aerosol particles and observations of new particle formation, Atmos. Chem. Phys., 10, 4253–4271, https://doi.org/10.5194/acp-10-4253-2010, 2010.

Bae, M. S., Lee, T., Schauer, J. J., Park, G., Son, Y. B., Kim, K. H., Cho, S. S., Park, S. S., Park, K., and Shon, Z. H.: Chemical Characteristics of Size-Resolved Aerosols in Coastal Areas during KORUS-AQ Campaign; Comparison of Ion Neutralization Model, Asia-Pacific J. Atmos. Sci., 55, 387–399, https://doi.org/10.1007/s13143-018-00099-1, 2019.

Bousiotis, D., Brean, J., Pope, F. D., Dall'Osto, M., Querol, X., Alastuey, A., Perez, N., Petäjä, T., Massling, A., Klenø Nøjgaard, J., Nordstrøm, C., Kouvarakis, G., Vratolis, S., Eleftheriadis, K., Niemi, J. V., Portin, H., Wiedensohler, A., Weinhold,

792 K., Merkel, M., Tuch, T., and Harrison, R. M.: The effect of meteorological
793 conditions and atmospheric composition in the occurrence and development of new
794 particle formation (NPF) events in Europe, Atmos. Chem. Phys., 21, 3345–3370,
795 https://doi.org/10.5194/acp-21-3345-2021, 2021.

796 Brooke Anderson, G. and Bell, M. L.: Heat waves in the United States: Mortality risk
797 during heat waves and effect modification by heat wave characteristics in 43 U.S.
798 communities, Environ. Health Perspect., 119, 210–218,
799 https://doi.org/10.1289/ehp.1002313, 2011.

800 Cai, R., Chandra, I., Yang, D., Yao, L., Fu, Y., Li, X., Lu, Y., Luo, L., Hao, J., Ma, Y.,
801 Wang, L., Zheng, J., Seto, T., and Jiang, J.: Estimating the influence of transport on
802 aerosol size distributions during new particle formation events, Atmos. Chem. Phys.,
803 18, 16587–16599, https://doi.org/10.5194/acp-18-16587-2018, 2018.

804 Chen, J., Zhao, C. S., Ma, N., and Yan, P.: Aerosol hygroscopicity parameter derived
805 from the light scattering enhancement factor measurements in the North China Plain,
806 Atmos. Chem. Phys., 14, 8105–8118, https://doi.org/10.5194/acp-14-8105-2014,
807 2014.

808 Chen, Q., Mu, Z., Song, W., Wang, Y., Yang, Z., Zhang, L., and Zhang, Y. L.:
809 Size-Resolved Characterization of the Chromophores in Atmospheric Particulate
810 Matter From a Typical Coal-Burning City in China, J. Geophys. Res. Atmos., 124,
811 10546–10563, https://doi.org/10.1029/2019JD031149, 2019.

812 Chen, T., Wang, T., Xue, L., and Brasseur, G.: Heatwave exacerbates air pollution in
813 China through intertwined climate-energy-environment interactions, Sci. Bull., 69,
814 2765–2775, https://doi.org/10.1016/j.scib.2024.05.018, 2024.

815 China Meteorological Administration, 2022. China Climate Bulletin 2022.
816 https://www.cma.gov.cn/zfxxgk/gknr/qxbg/202303/t20230324_5396394.html.
817 Accessed on 23 March 2023. (in Chinese).

Cho Cheung, H., Chung-Kuang Chou, C., Siu Lan Lee, C., Kuo, W. C., and Chang, S. C.: Hygroscopic properties and cloud condensation nuclei activity of atmospheric aerosols under the influences of Asian continental outflow and new particle formation at a coastal site in eastern Asia, Atmos. Chem. Phys., 20, 5911–5922, https://doi.org/10.5194/acp-20-5911-2020, 2020.

Chylek, P. and Wong, J.: Effect of absorbing aerosols on global radiation budget, Geophys. Res. Lett., 22, 929–931, https://doi.org/10.1029/95GL00800, 1995.

Collaud Coen, M., Weingartner, E., Nyeki, S., Cozic, J., Henning, S., Verheggen, B., Gehrig, R., and Baltensperger, U.: Long-term trend analysis of aerosol variables at the high-alpine site Jungfraujoch, J. Geophys. Res. Atmos., 112, https://doi.org/10.1029/2006JD007995, 2007.

Covert, D. S., Charlson, R. J., and Ahlquist, N. C.: A Study of the Relationship of Chemical Composition and Humidity to Light Scattering by Aerosols, J. Appl. Meteorol., 11, 968–976, https://doi.org/10.1175/1520-0450(1972)011<0968:asotro>2.0.co;2, 1972.

Crumeyrolle, S., Kontkanen, J. S. S., Rose, C., Velazquez Garcia, A., Bourrianne, E., Catalfamo, M., Riffault, V., Tison, E., Ferreira De Brito, J., Visez, N., Ferlay, N., Auriol, F., and Chiapello, I.: Measurement report: Atmospheric new particle formation at a peri-urban site in Lille, northern France, Atmos. Chem. Phys., 23, 183–201, https://doi.org/10.5194/acp-23-183-2023, 2023.

Cusack, M., Alastuey, A., and Querol, X.: Case studies of new particle formation and evaporation processes in the western Mediterranean regional background, Atmos. Environ., 81, 651–659, https://doi.org/10.1016/j.atmosenv.2013.09.025, 2013.

Dada, L., Paasonen, P., Nieminen, T., Buenrostro Mazon, S., Kontkanen, J., Peräkylä, O., Lehtipalo, K., Hussein, T., Petäjä, T., Kerminen, V. M., Bäck, J., and Kulmala, M.: Long-term analysis of clear-sky new particle formation events and nonevents in

Hyytiälä, Atmos. Chem. Phys., 17, 6227–6241, https://doi.org/10.5194/acp-17-6227-2017, 2017.

Dal Maso, M., Kulmala, M., Riipinen, I., Wagner, R., Hussein, T., Aalto, P. P., and Lehtinen, K. E. J.: Formation and growth of fresh atmospheric aerosols: Eight years of aerosol size distribution data from SMEAR II, Hyytiälä, Finland, Boreal Environ. Res., 10, 323–336, 2005.

Delene, D. J. and Ogren, J. A.: Variability of aerosol optical properties at four North American surface monitoring sites, J. Atmos. Sci., 59, 1135–1150, https://doi.org/10.1175/1520-0469(2002)059<1135:VOAOPA>2.0.CO;2, 2002.

Deng, C., Cai, R., Yan, C., Zheng, J., and Jiang, J.: Formation and growth of sub-3 nm particles in megacities: Impact of background aerosols, Faraday Discuss., 226, 348–363, https://doi.org/10.1039/d0fd00083c, 2021.

Deng, C., Fu, Y., Dada, L., Yan, C., Cai, R., Yang, D., Zhou, Y., Yin, R., Lu, Y., Li, X., Qiao, X., Fan, X., Nie, W., Kontkanen, J., Kangasluoma, J., Chu, B., Ding, A., Kerminen, V. M., Paasonen, P., Worsnop, D. R., Bianchi, F., Liu, Y., Zheng, J., Wang, L., Kulmala, M., and Jiang, J.: Seasonal characteristics of new particle formation and growth in urban Beijing, Environ. Sci. Technol., 54, 8547–8557, https://doi.org/10.1021/acs.est.0c00808, 2020.

Duan, J., Huang, R. J., Wang, Y., Xu, W., Zhong, H., Lin, C., Huang, W., Gu, Y., Ovadnevaite, J., Ceburnis, D., and O'Dowd, C.: Measurement report: Size-resolved secondary organic aerosol formation modulated by aerosol water uptake in wintertime haze, Atmos. Chem. Phys., 24, 7687–7698, https://doi.org/10.5194/acp-24-7687-2024, 2024.

Fan, J., Wang, Y., Rosenfeld, D., and Liu, X.: Review of aerosol-cloud interactions: Mechanisms, significance, and challenges, J. Atmos. Sci., 73, 4221–4252, https://doi.org/10.1175/JAS-D-16-0037.1, 2016.

Fierz-Schmidhauser, R., Zieger, P., Gysel, M., Kammermann, L., Decarlo, P. F., Baltensperger, U., and Weingartner, E.: Measured and predicted aerosol light scattering enhancement factors at the high alpine site Jungfraujoch, Atmos. Chem. Phys, 10, 2319–2333, 2010.

Garmash, O., Ezhova, E., Arshinov, M., Belan, B., Lampilahti, A., Davydov, D., Räty, M., Aliaga, D., Baalbaki, R., Chan, T., Bianchi, F., Kerminen, V. M., Petäjä, T., and Kulmala, M.: Heatwave reveals potential for enhanced aerosol formation in Siberian boreal forest, Environ. Res. Lett., 19, https://doi.org/10.1088/1748-9326/ad10d5, 2024.

Giordano, M., Espinoza, C., and Asa-Awuku, A.: Experimentally measured morphology of biomass burning aerosol and its impacts on CCN ability, Atmos. Chem. Phys., 15, 1807–1821, https://doi.org/10.5194/acp-15-1807-2015, 2015.

Gu, Y., Huang, R. J., Duan, J., Xu, W., Lin, C., Zhong, H., Wang, Y., Ni, H., Liu, Q., Xu, R., Wang, L., and Li, Y. J.: Multiple pathways for the formation of secondary organic aerosol in the North China Plain in summer, Atmos. Chem. Phys., 23, 5419–5433, https://doi.org/10.5194/acp-23-5419-2023, 2023.

Guenther, A. B., Monson, R. K., and Fall, R.: Isoprene and monoterpene emission rate variability: Observations with eucalyptus and emission rate algorithm development, J. Geophys. Res. Atmos., 96, 10799–10808, https://doi.org/10.1029/91jd00960, 1991.

Guo, X., Huang, J., Luo, Y., Zhao, Z., and Xu, Y.: Projection of heat waves over China for eight different global warming targets using 12 CMIP5 models, Theor. Appl. Climatol., 128, 507–522, https://doi.org/10.1007/s00704-015-1718-1, 2016.

Hamed, A., Joutsensaari, J., Mikkonen, S., Sogacheva, L., Dal Maso, M., Kulmala, M., Cavalli, F., Fuzzi, S., Facchini, M. C., Decesari, S., Mircea, M., Lehtinen, K. E. J.,

and Laaksonen, A.: Nucleation and growth of new particles in Po Valley, Italy, Atmos. Chem. Phys., 7, 355–376, https://doi.org/10.5194/acp-7-355-2007, 2007.

Hamed, A., Korhonen, H., Sihto, S. L., Joutsensaari, J., Jrvinen, H., Petäjä, T., Arnold, F., Nieminen, T., Kulmala, M., Smith, J. N., Lehtinen, K. E. J., and Laaksonen, A.: The role of relative humidity in continental new particle formation, J. Geophys. Res. Atmos., 116, 1–12, https://doi.org/10.1029/2010JD014186, 2011.

Hand, J. L. and Malm, W. C.: Review of aerosol mass scattering efficiencies from ground-based measurements since 1990, J. Geophys. Res. Atmos., 112, https://doi.org/10.1029/2007JD008484, 2007.

Hao, Y., Gou, Y., Wang, Z., Huang, W., Wan, F., Tian, M., and Chen, J.: Current challenges in the visibility improvement of urban Chongqing in Southwest China: From the perspective of PM2.5-bound water uptake property over 2015–2021, Atmos. Res., 300, 107215, https://doi.org/10.1016/j.atmosres.2023.107215, 2024.

Hao, Z., Chen, Y., Feng, S., Liao, Z., An, N., and Li, P.: The 2022 Sichuan-Chongqing spatio-temporally compound extremes: a bitter taste of novel hazards, Sci. Bull., 68, 1337–1339, https://doi.org/10.1016/j.scib.2023.05.034, 2023.

Hauser, M., Orth, R., and Seneviratne, S. I.: Role of soil moisture versus recent climate change for the 2010 heat wave in western Russia, Geophys. Res. Lett., 43, 2819–2826, https://doi.org/10.1002/2016GL068036, 2016.

Jefferson, A., Hageman, D., Morrow, H., Mei, F., and Watson, T.: Seven years of aerosol scattering hygroscopic growth measurements from SGP: Factors influencing water uptake, J. Geophys. Res. Atmos., 122, 9451–9466, https://doi.org/10.1002/2017JD026804, 2017.

Jin, X., Li, Z., Wu, T., Wang, Y., Cheng, Y., Su, T., Wei, J., Ren, R., Wu, H., Li, S., Zhang, D., and Cribb, M.: The different sensitivities of aerosol optical properties to particle concentration, humidity, and hygroscopicity between the surface level and the

upper boundary layer in Guangzhou, China, Sci. Total Environ., 803, 150010, https://doi.org/10.1016/j.scitotenv.2021.150010, 2022.

Kerminen, V. M., Chen, X., Vakkari, V., Petäjä, T., Kulmala, M., and Bianchi, F.: Atmospheric new particle formation and growth: Review of field observations, Environ. Res. Lett., 13, https://doi.org/10.1088/1748-9326/aadf3c, 2018.

Kim, N., Yum, S. S., Park, M., Park, J. S., Shin, H. J., and Ahn, J. Y.: Hygroscopicity of urban aerosols and its link to size-resolved chemical composition during spring and summer in Seoul, Korea, Atmos. Chem. Phys., 20, 11245–11262, https://doi.org/10.5194/acp-20-11245-2020, 2020.

Kotchenruther, R. A., Hobbs, P. V., and Hegg, D. A.: Humidification factors for atmospheric aerosols off the mid-Atlantic coast of the United States, J. Geophys. Res. Atmos., 104, 2239–2251, https://doi.org/10.1029/98JD01751, 1999.

Kuang, Y., He, Y., Xu, W., Zhao, P., Cheng, Y., Zhao, G., Tao, J., Ma, N., Su, H., Zhang, Y., Sun, J., Cheng, P., Yang, W., Zhang, S., Wu, C., Sun, Y., and Zhao, C.: Distinct diurnal variation in organic aerosol hygroscopicity and its relationship with oxygenated organic aerosol, Atmos. Chem. Phys., 20, 865–880, https://doi.org/10.5194/acp-20-865-2020, 2020.

Kuang, Y., Zhao, C. S., Zhao, G., Tao, J. C., Xu, W., Ma, N., and Bian, Y. X.: A novel method for calculating ambient aerosol liquid water content based on measurements of a humidified nephelometer system, Atmos. Meas. Tech., 11, 2967–2982, https://doi.org/10.5194/amt-11-2967-2018, 2018.

Kuang, Y., Zhao, C., Tao, J., Bian, Y., Ma, N., and Zhao, G.: A novel method for deriving the aerosol hygroscopicity parameter based only on measurements from a humidified nephelometer system, Atmos. Chem. Phys., 17, 6651–6662, https://doi.org/10.5194/acp-17-6651-2017, 2017.

946 Kulmala, M., Dada, L., Daellenbach, K. R., Yan, C., Stolzenburg, D., Kontkanen, J.,
947 Ezhova, E., Hakala, S., Tuovinen, S., Kokkonen, T. V., Kurppa, M., Cai, R., Zhou, Y.,
948 Yin, R., Baalbaki, R., Chan, T., Chu, B., Deng, C., Fu, Y., Ge, M., He, H., Heikkinen,
949 L., Junninen, H., Liu, Y., Lu, Y., Nie, W., Rusanen, A., Vakkari, V., Wang, Y., Yang, G.,
950 Yao, L., Zheng, J., Kujansuu, J., Kangasluoma, J., Petaja, T., Paasonen, P., Jarvi, L.,
951 Worsnop, D., Ding, A., Liu, Y., Wang, L., Jiang, J., Bianchi, F., and Kerminen, V. M.:
952 Is reducing new particle formation a plausible solution to mitigate particulate air
953 pollution in Beijing and other Chinese megacities?, Faraday Discuss., 226, 334–347,
954 https://doi.org/10.1039/d0fd00078g, 2021.

955 Kulmala, M., Petäjä, T., Nieminen, T., Sipilä, M., Manninen, H. E., Lehtipalo, K., Dal
956 Maso, M., Aalto, P. P., Junninen, H., Paasonen, P., Riipinen, I., Lehtinen, K. E. J.,
957 Laaksonen, A., and Kerminen, V. M.: Measurement of the nucleation of atmospheric
958 aerosol particles, Nat. Protoc., 7, 1651–1667, https://doi.org/10.1038/nprot.2012.091,
959 2012.

960 Kulmala, M.: How Particles Nucleate and Grow, Science, 302, 1000–1001,
961 https://doi.org/10.1126/science.1090848, 2003.

962 Kurtén, T., Torpo, L., Ding, C. G., Vehkamäki, H., Sundberg, M. R., Laasonen, K.,
963 and Kulmala, M.: A density functional study on water-sulfuric acid-ammonia clusters
964 and implications for atmospheric cluster formation, J. Geophys. Res. Atmos., 112, 1–7,
965 https://doi.org/10.1029/2006JD007391, 2007.

966 Lee, K., Chandra, I., Seto, T., Inomata, Y., Hayashi, M., Takami, A., Yoshino, A., and
967 Otani, Y.: Aerial observation of atmospheric nanoparticles on Fukue Island, Japan,
968 Aerosol Air Qual. Res., 19, 981–994, https://doi.org/10.4209/aaqr.2018.03.0077,
969 2019.

970 Li, Y., Ding, Y., and Li, W.: Observed trends in various aspects of compound heat
971 waves across China from 1961 to 2015, J. Meteorol. Res., 31, 455–467,
972 https://doi.org/10.1007/s13351-017-6150-2, 2017.

973 Li, Z., Tikkanen, O. P., Buchholz, A., Hao, L., Kari, E., Yli-Juuti, T., and Virtanen, A.:
974 Effect of Decreased Temperature on the Evaporation of α-Pinene Secondary Organic
975 Aerosol Particles, ACS Earth Sp. Chem., 3, 2775–2785,
976 https://doi.org/10.1021/acsearthspacechem.9b00240, 2019.

977 Liu, H. J., Zhao, C. S., Nekat, B., Ma, N., Wiedensohler, A., Van Pinxteren, D.,
978 Spindler, G., Müller, K., and Herrmann, H.: Aerosol hygroscopicity derived from
979 size-segregated chemical composition and its parameterization in the North China
980 Plain, Atmos. Chem. Phys., 14, 2525–2539, https://doi.org/10.5194/acp-14-2525-2014,
981 2014.

982 Liu, P. F., Zhao, C. S., Göbel, T., Hallbauer, E., Nowak, A., Ran, L., Xu, W. Y., Deng,
983 Z. Z., Ma, N., Mildenberger, K., Henning, S., Stratmann, F., and Wiedensohler, A.:
984 Hygroscopic properties of aerosol particles at high relative humidity and their diurnal
985 variations in the north China plain, Atmos. Chem. Phys., 11, 3479–3494,
986 https://doi.org/10.5194/acp-11-3479-2011, 2011.

987 Lu, Y., Yan, C., Fu, Y., Chen, Y., Liu, Y., Yang, G., Wang, Y., Bianchi, F., Chu, B.,
988 Zhou, Y., Yin, R., Baalbaki, R., Garmash, O., Deng, C., Wang, W., Liu, Y., Petäjä, T.,
989 Kerminen, V. M., Jiang, J., Kulmala, M., and Wang, L.: A proxy for atmospheric
990 daytime gaseous sulfuric acid concentration in urban Beijing, Atmos. Chem. Phys., 19,
991 1971–1983, https://doi.org/10.5194/acp-19-1971-2019, 2019.

992 Luoma, K., Virkkula, A., Aalto, P., Petäjä, T., and Kulmala, M.: Over a 10-year record
993 of aerosol optical properties at SMEAR II, Atmos. Chem. Phys., 19, 11363–11382,
994 https://doi.org/10.5194/acp-19-11363-2019, 2019.

995 Ma, C. Sen, Ma, G., and Pincebourde, S.: Survive a Warming Climate: Insect
996 Responses to Extreme High Temperatures, Annu. Rev. Entomol., 66, 163–184,
997 https://doi.org/10.1146/annurev-ento-041520-074454, 2021.

998 Ma, N., Zhao, C., Tao, J., Wu, Z., Kecorius, S., Wang, Z., Groß, J., Liu, H., Bian, Y.,
999 Kuang, Y., Teich, M., Spindler, G., Muller, K., Van Pinxteren, D., Herrmann, H., Hu,
1000 M., and Wiedensohler, A.: Variation of CCN activity during new particle formation
1001 events in the North China Plain, Atmos. Chem. Phys., 16, 8593–8607,
1002 https://doi.org/10.5194/acp-16-8593-2016, 2016.

1003 Marshall, S. F., Covert, D. S., and Charlson, R. J.: Relationship between asymmetry
1004 parameter and hemispheric backscatter ratio: implications for climate forcing by
1005 aerosols, Appl. Opt., 34, 5–6, 1995.

1006 Merikanto, J., Spracklen, D. V, Mann, G. W., Pickering, S. J., and Carslaw, K. S.:
1007 Atmospheric Chemistry and Physics Impact of nucleation on global CCN, Atmos.
1008 Chem. Phys, 9, 8601–8616, 2009.

1009 Mishchenko, M. I.: Electromagnetic scattering by nonspherical particles: A tutorial
1010 review, J. Quant. Spectrosc. Radiat. Transf., 110, 808–832,
1011 https://doi.org/10.1016/j.jqsrt.2008.12.005, 2009.

1012 Moise, T., Flores, J. M., and Rudich, Y.: Optical Properties of Secondary Organic
1013 Aerosols and Their Changes by Chemical Processes, Chem. Rev., 115, 4400–4439,
1014 https://doi.org/10.1021/cr5005259, 2015.

1015 Nairn, J. R. and Fawcett, R. J. B.: The excess heat factor: A metric for heatwave
1016 intensity and its use in classifying heatwave severity, Int. J. Environ. Res. Public
1017 Health, 12, 227–253, https://doi.org/10.3390/ijerph120100227, 2014.

1018 Petters, M. D. and Kreidenweis, S. M.: A single parameter representation of
1019 hygroscopic growth and cloud condensation nucleus activity, Atmos. Chem. Phys., 7,
1020 1961–1971, https://doi.org/10.5194/acp-7-1961-2007, 2007.

1021 Pierce, T. E. and Waldruff, P. S.: Pc-beis: A personal computer version of the biogenic
1022 emissions inventory system, J. Air Waste Manag. Assoc., 41, 937–941,
1023 https://doi.org/10.1080/10473289.1991.10466890, 1991.

1024 Qi, X. M., Ding, A. J., Nie, W., Petäjä, T., Kerminen, V. M., Herrmann, E., Xie, Y. N.,
1025 Zheng, L. F., Manninen, H., Aalto, P., Sun, J. N., Xu, Z. N., Chi, X. G., Huang, X.,
1026 Boy, M., Virkkula, A., Yang, X. Q., Fu, C. B., and Kulmala, M.: Aerosol size
1027 distribution and new particle formation in the western Yangtze River Delta of China:
1028 2 years of measurements at the SORPES station, Atmos. Chem. Phys., 15,
1029 12445–12464, https://doi.org/10.5194/acp-15-12445-2015, 2015.

1030 Quinn, P. K., Bates, T. S., Baynard, T., Clarke, A. D., Onasch, T. B., Wang, W., Rood,
1031 M. J., Andrews, E., Allan, J., Carrico, C. M., Coffman, D., and Worsnop, D.: Impact
1032 of particulate organic matter on the relative humidity dependence of light scattering: A
1033 simplified parameterization, Geophys. Res. Lett., 32, 1–4,
1034 https://doi.org/10.1029/2005GL024322, 2005.

1035 Ren, J., Chen, L., Fan, T., Liu, J., Jiang, S., and Zhang, F.: The NPF Effect on CCN
1036 Number Concentrations: A Review and Re-Evaluation of Observations From 35 Sites
1037 Worldwide, Geophys. Res. Lett., 48, 1–12, https://doi.org/10.1029/2021GL095190,
1038 2021.

1039 Rosati, B., Isokääntä, S., Christiansen, S., Jensen, M. M., Moosakutty, S. P., De Jonge,
1040 R. W., Massling, A., Glasius, M., Elm, J., Virtanen, A., and Bilde, M.:
1041 Hygroscopicity and CCN potential of DMS-derived aerosol particles, Atmos. Chem.
1042 Phys., 22, 13449–13466, https://doi.org/10.5194/acp-22-13449-2022, 2022.

1043 Salma, I., Thén, W., Aalto, P., Kerminen, V. M., Kern, A., Barcza, Z., Petäjä, T., and
1044 Kulmala, M.: Influence of vegetation on occurrence and time distributions of regional
1045 new aerosol particle formation and growth, Atmos. Chem. Phys., 21, 2861–2880,
1046 https://doi.org/10.5194/acp-21-2861-2021, 2021.

1047 Schuster, G. L., Dubovik, O., and Holben, B. N.: Angstrom exponent and bimodal
1048 aerosol size distributions, J. Geophys. Res. Atmos., 111, 1–14,
1049 https://doi.org/10.1029/2005JD006328, 2006.

Shang, D., Hu, M., Tang, L., Fang, X., Liu, Y., Wu, Y., Du, Z., Cai, X., Wu, Z., Lou, S., Hallquist, M., Guo, S., and Zhang, Y.: Significant effects of transport on nanoparticles during new particle formation events in the atmosphere of Beijing, Particuology, 80, 1–10, https://doi.org/10.1016/j.partic.2022.12.006, 2023.

Sharma, S. and Mujumdar, P.: Increasing frequency and spatial extent of concurrent meteorological droughts and heatwaves in India, Sci. Rep., 7, 1–9, https://doi.org/10.1038/s41598-017-15896-3, 2017.

Shen, X. J., Sun, J. Y., Zhang, Y. M., Wehner, B., Nowak, A., Tuch, T., Zhang, X. C., Wang, T. T., Zhou, H. G., Zhang, X. L., Dong, F., Birmili, W., and Wiedensohler, A.: First long-term study of particle number size distributions and new particle formation events of regional aerosol in the North China Plain, Atmos. Chem. Phys., 11, 1565–1580, https://doi.org/10.5194/acp-11-1565-2011, 2011.

Su, Y. W.: The effects of extreme high temperature day off on electricity conservation, Weather. Clim. Soc., 13, 769–782, https://doi.org/10.1175/WCAS-D-20-0176.1, 2021.

Sun, J., Hermann, M., Weinhold, K., Merkel, M., Birmili, W., Yang, Y., Flentje, H., Ries, L., Couret, C., Elsasser, M., Sohmer, R., Wirtz, K., Meinhardt, F., Schü, M., Bath, O., Hellack, B., Kerminen, V., Kulmala, M., Ma, N., and Wiedensohler, A.: Measurement report : Contribution of atmospheric new particle formation to ultrafine particle concentration , cloud condensation nuclei and radiative forcing : Results from five-year observations in Central Europe, Atmos. Chem. Phys., 1–34, https://doi.org/10.5194/acp-24-10667-2024, 2024.

Sun, X., Sun, Q., Zhou, X., Li, X., Yang, M., Yu, A., and Geng, F.: Heat wave impact on mortality in Pudong New Area, China in 2013, Sci. Total Environ., 493, 789–794, https://doi.org/10.1016/j.scitotenv.2014.06.042, 2014.

Sun, Y., Song, L., Yin, H., Zhang, X., Stott, P., Zhou, B., and Hu, T.: 20. Human influence on the 2015 extreme high temperature events in Western China, Bull. Am. Meteorol. Soc., 97, S102–S106, https://doi.org/10.1175/BAMS-D-16-0158.1, 2016.

Tan, J., Zheng, Y., Song, G., Kalkstein, L. S., Kalkstein, A. J., and Tang, X.: Heat wave impacts on mortality in Shanghai, 1998 and 2003, Int. J. Biometeorol., 51, 193–200, https://doi.org/10.1007/s00484-006-0058-3, 2007.

Tan, W., Yu, Y., Li, C., Li, J., Kang, L., Dong, H., Zeng, L., and Zhu, T.: Profiling Aerosol Liquid Water Content Using a Polarization Lidar, Environ. Sci. Technol., 54, 3129–3137, https://doi.org/10.1021/acs.est.9b07502, 2020.

Tang, M., Chan, C. K., Li, Y. J., Su, H., Ma, Q., Wu, Z., Zhang, G., Wang, Z., Ge, M., Hu, M., He, H., and Wang, X.: A review of experimental techniques for aerosol hygroscopicity studies, Atmos. Chem. Phys., 19, 12631–12686, https://doi.org/10.5194/acp-19-12631-2019, 2019.

Tao, L., Zhou, Z., Tao, J., Zhang, L., Wu, C., Li, J., Yue, D., Wu, Z., Zhang, Z., Yuan, Z., Huang, J., and Wang, B.: High contribution of new particle formation to ultrafine particles in four seasons in an urban atmosphere in south China, Sci. Total Environ., 889, https://doi.org/10.1016/j.scitotenv.2023.164202, 2023.

Teng, M., Liao, H., Burke, P. J., Chen, T., and Zhang, C.: Adaptive responses: the effects of temperature levels on residential electricity use in China, Clim. Change, 172, https://doi.org/10.1007/s10584-022-03374-3, 2022.

Tian, J., Wang, Q., Zhang, Y., Yan, M., Liu, H., Zhang, N., Ran, W., and Cao, J.: Impacts of primary emissions and secondary aerosol formation on air pollution in an urban area of China during the COVID-19 lockdown, Environ. Int., 150, 106426, https://doi.org/10.1016/j.envint.2021.106426, 2021.

Titos, G., Burgos, M. A., Zieger, P., Alados-Arboledas, L., Baltensperger, U., Jefferson, A., Sherman, J., Weingartner, E., Henzing, B., Luoma, K., O'Dowd, C.,

Wiedensohler, A., and Andrews, E.: A global study of hygroscopicity-driven light-scattering enhancement in the context of other in situ aerosol optical properties, Atmos. Chem. Phys., 21, 13031–13050, https://doi.org/10.5194/acp-21-13031-2021, 2021.

Titos, G., Cazorla, A., Zieger, P., Andrews, E., Lyamani, H., Granados-Muñoz, M. J., Olmo, F. J., and Alados-Arboledas, L.: Effect of hygroscopic growth on the aerosol light-scattering coefficient: A review of measurements, techniques and error sources, Atmos. Environ., 141, 494–507, https://doi.org/10.1016/j.atmosenv.2016.07.021, 2016.

Titos, G., Jefferson, A., Sheridan, P. J., Andrews, E., Lyamani, H., Alados-Arboledas, L., and Ogren, J. A.: Aerosol light-scattering enhancement due to water uptake during the TCAP campaign, Atmos. Chem. Phys., 14, 7031–7043, https://doi.org/10.5194/acp-14-7031-2014, 2014.

Tritscher, T., Jurnyi, Z., Martin, M., Chirico, R., Gysel, M., Heringa, M. F., Decarlo, P. F., Sierau, B., Prévt, A. S. H., Weingartner, E., and Baltensperger, U.: Changes of hygroscopicity and morphology during ageing of diesel soot, Environ. Res. Lett., 6, https://doi.org/10.1088/1748-9326/6/3/034026, 2011.

Wang, N., Du, Y., Chen, D., Meng, H., Chen, X., Zhou, L., Shi, G., Zhan, Y., Feng, M., Li, W., Chen, M., Li, Z., and Yang, F.: Spatial disparities of ozone pollution in the Sichuan Basin spurred by extreme, hot weather, Atmos. Chem. Phys., 24, 3029–3042, https://doi.org/10.5194/acp-24-3029-2024, 2024.

Wang, Y., Li, Z., Zhang, R., Jin, X., Xu, W., Fan, X., Wu, H., Zhang, F., Sun, Y., Wang, Q., Cribb, M., and Hu, D.: Distinct Ultrafine- and Accumulation-Mode Particle Properties in Clean and Polluted Urban Environments, Geophys. Res. Lett., 46, 10918–10925, https://doi.org/10.1029/2019GL084047, 2019.

Wang, Z. B., Hu, M., Sun, J. Y., Wu, Z. J., Yue, D. L., Shen, X. J., Zhang, Y. M., Pei, X. Y., Cheng, Y. F., and Wiedensohler, A.: Characteristics of regional new particle formation in urban and regional background environments in the North China Plain, Atmos. Chem. Phys., 13, 12495–12506, https://doi.org/10.5194/acp-13-12495-2013, 2013.

Wang, Z., Wu, Z., Yue, D., Shang, D., Guo, S., Sun, J., Ding, A., Wang, L., Jiang, J., Guo, H., Gao, J., Cheung, H. C., Morawska, L., Keywood, M., and Hu, M.: New particle formation in China: Current knowledge and further directions, Sci. Total Environ., 577, 258–266, https://doi.org/10.1016/j.scitotenv.2016.10.177, 2017.

Westervelt, D. M., Pierce, J. R., Riipinen, I., Trivitayanurak, W., Hamed, A., Kulmala, M., Laaksonen, A., Decesari, S., and Adams, P. J.: Formation and growth of nucleated particles into cloud condensation nuclei: Model-measurement comparison, Atmos. Chem. Phys., 13, 7645–7663, https://doi.org/10.5194/acp-13-7645-2013, 2013.

Wu, Z. J., Poulain, L., Birmili, W., Größ, J., Niedermeier, N., Wang, Z. B., Herrmann, H., and Wiedensohler, A.: Some insights into the condensing vapors driving new particle growth to CCN sizes on the basis of hygroscopicity measurements, Atmos. Chem. Phys., 15, 13071–13083, https://doi.org/10.5194/acp-15-13071-2015, 2015.

Wu, Z. J., Zheng, J., Shang, D. J., Du, Z. F., Wu, Y. S., Zeng, L. M., Wiedensohler, A., and Hu, M.: Particle hygroscopicity and its link to chemical composition in the urban atmosphere of Beijing, China, during summertime, Atmos. Chem. Phys., 16, 1123–1138, https://doi.org/10.5194/acp-16-1123-2016, 2016.

Xia, C., Sun, J., Hu, X., Shen, X., Zhang, Y., Zhang, S., Wang, J., Liu, Q., Lu, J., Liu, S., and Zhang, X.: Effects of hygroscopicity on aerosol optical properties and direct radiative forcing in Beijing: Based on two-year observations, Sci. Total Environ., 857, 159233, https://doi.org/10.1016/j.scitotenv.2022.159233, 2023.

Xu, W. Y., Zhao, C. S., Ran, L., Deng, Z. Z., Liu, P. F., Ma, N., Lin, W. L., Xu, X. B., Yan, P., He, X., Yu, J., Liang, W. D., and Chen, L. L.: Characteristics of pollutants and their correlation to meteorological conditions at a suburban site in the North China Plain, Atmos. Chem. Phys., 11, 4353–4369, https://doi.org/10.5194/acp-11-4353-2011, 2011.

Xu, W., Chen, C., Qiu, Y., Xie, C., Chen, Y., Ma, N., Xu, W., Fu, P., Wang, Z., Pan, X., Zhu, J., Ngcg, N. L., and Sun, Y.: Size-resolved characterization of organic aerosol in the North China Plain: New insights from high resolution spectral analysis, Environ. Sci. Atmos., 1, 346–358, https://doi.org/10.1039/d1ea00025j, 2021.

Xu, W., Kuang, Y., Xu, W., Zhang, Z., Luo, B., Zhang, X., Tao, J., Qiao, H., Liu, L., and Sun, Y.: Hygroscopic growth and activation changed submicron aerosol composition and properties in the North China Plain, Atmos. Chem. Phys., 24, 9387–9399, https://doi.org/10.5194/acp-24-9387-2024, 2024.

Xue, B., Kuang, Y., Xu, W., and Zhao, P.: Joint increase of aerosol scattering efficiency and aerosol hygroscopicity aggravate visibility impairment in the North China Plain, Sci. Total Environ., 839, 141163, https://doi.org/10.1016/j.scitotenv.2022.156279, 2022.

Yang, P., Feng, Q., Hong, G., Kattawar, G. W., Wiscombe, W. J., Mishchenko, M. I., Dubovik, O., Laszlo, I., and Sokolik, I. N.: Modeling of the scattering and radiative properties of nonspherical dust-like aerosols, J. Aerosol Sci., 38, 995–1014, https://doi.org/10.1016/j.jaerosci.2007.07.001, 2007.

Yarragunta, Y., Srivastava, S., Mitra, D., and Chandola, H. C.: Source apportionment of carbon monoxide over India: a quantitative analysis using MOZART-4, Environ. Sci. Pollut. Res., 28, 8722–8742, https://doi.org/10.1007/s11356-020-11099-y, 2021.

Yuan, L. and Zhao, C.: Quantifying particle-To-particle heterogeneity in aerosol hygroscopicity, Atmos. Chem. Phys., 23, 3195–3205, https://doi.org/10.5194/acp-23-3195-2023, 2023.

Zhang, L., Sun, J. Y., Shen, X. J., Zhang, Y. M., Che, H., Ma, Q. L., Zhang, Y. W., Zhang, X. Y., and Ogren, J. A.: Observations of relative humidity effects on aerosol light scattering in the Yangtze River Delta of China, Atmos. Chem. Phys., 15, 8439–8454, https://doi.org/10.5194/acp-15-8439-2015, 2015.

Zhang, R., Khalizov, A. F., Pagels, J., Zhang, D., Xue, H., and McMurry, P. H.: Variability in morphology, hygroscopicity, and optical properties of soot aerosols during atmospheric processing, Proc. Natl. Acad. Sci. U. S. A., 105, 10291–10296, https://doi.org/10.1073/pnas.0804860105, 2008.

Zhang, R., Khalizov, A., Wang, L., Hu, M., and Xu, W.: Nucleation and growth of nanoparticles in the atmosphere, Chem. Rev., 112, 1957–2011, https://doi.org/10.1021/cr2001756, 2012.

Zhang, R., Suh, I., Zhao, J., Zhang, D., Fortner, E. C., Tie, X., Molina, L. T., and Molina, M. J.: Atmospheric new particle formation enhanced by organic acids, Science (80-.)., 304, 1487–1490, https://doi.org/10.1126/science.1095139, 2004.

Zhang, R., Wang, G., Guo, S., Zamora, M. L., Ying, Q., Lin, Y., Wang, W., Hu, M., and Wang, Y.: Formation of Urban Fine Particulate Matter, Chem. Rev., 115, 3803–3855, https://doi.org/10.1021/acs.chemrev.5b00067, 2015.

Zhang, Z., Xu, W., Zeng, S., Liu, Y., Liu, T., Zhang, Y., Du, A., Li, Y., Zhang, N., Wang, J., Aruffo, E., Han, P., Li, J., Wang, Z., and Sun, Y.: Secondary Organic Aerosol Formation from Ambient Air in Summer in Urban Beijing: Contribution of S/IVOCs and Impacts of Heat Waves, Environ. Sci. Technol. Lett., https://doi.org/10.1021/acs.estlett.4c00415, 2024.

Zhao, C., Yu, Y., Kuang, Y., Tao, J., and Zhao, G.: Recent Progress of Aerosol Light-scattering Enhancement Factor Studies in China, Adv. Atmos. Sci., 36, 1015–1026, https://doi.org/10.1007/s00376-019-8248-1, 2019.

Zhao, G., Hu, M., Fang, X., Tan, T., Xiao, Y., Du, Z., Zheng, J., Shang, D., Wu, Z., Guo, S., and Zhao, C.: Larger than expected variation range in the real part of the refractive index for ambient aerosols in China, Sci. Total Environ., 779, 146443, https://doi.org/10.1016/j.scitotenv.2021.146443, 2021.

Zhao, S., Yu, Y., Li, J., Yin, D., Qi, S., and Qin, D.: Response of particle number concentrations to the clean air action plan: Lessons from the first long-term aerosol measurements in a typical urban valley in western China, Atmos. Chem. Phys., 21, 14959–14981, https://doi.org/10.5194/acp-21-14959-2021, 2021.

Zhu, Y., Shen, Y., Li, K., Meng, H., Sun, Y., Yao, X., Gao, H., Xue, L., and Wang, W.: Investigation of Particle Number Concentrations and New Particle Formation With Largely Reduced Air Pollutant Emissions at a Coastal Semi-Urban Site in Northern China, J. Geophys. Res. Atmos., 126, 1–20, https://doi.org/10.1029/2021JD035419, 2021.

Zieger, P., Weingartner, E., Henzing, J., Moerman, M., De Leeuw, G., Mikkilä, J., Ehn, M., Petäjä, T., Clémer, K., Van Roozendael, M., Yilmaz, S., Frieß, U., Irie, H., Wagner, T., Shaiganfar, R., Beirle, S., Apituley, A., Wilson, K., and Baltensperger, U.: Comparison of ambient aerosol extinction coefficients obtained from in-situ, MAX-DOAS and LIDAR measurements at Cabauw, Atmos. Chem. Phys., 11, 2603–2624, https://doi.org/10.5194/acp-11-2603-2011, 2011.

Supporting Information for

Divergent changes in aerosol optical hygroscopicity and new particle formation ~~induced by~~ during heatwaves of summer 2022

Yuhang Hao[1, a], Peizhao Li[1, a], Yafeng Gou[1], Zhenshuai Wang[1], Mi Tian[1], Yang Chen[2], Ye Kuang[3], Hanbing Xu[4], Fenglian Wan[1], Yuqian Luo[1], Wei Huang[5], Jing Chen[1, 6, *]

[1] College of Environment and Ecology, Chongqing University, Chongqing 400045, China

[2] Center for the Atmospheric Environment Research, Chongqing Institute of Green and Intelligent Technology, Chinese Academy of Sciences, Chongqing 400714, China

[3] Institute for Environmental and Climate Research, Jinan University, Guangzhou 511443, China

[4] Experimental Teaching Center, Sun Yat-sen University, Guangzhou 510275, China

[5] National Meteorological Center, China Meteorological Administration, Beijing 100081, China

[6] Key Laboratory of Three Gorges Reservoir Region's Eco-Environment, Ministry of Education, Chongqing University, Chongqing 400045, China

[a] These authors contributed equally

Correspondence to: Jing Chen (chen.jing@cqu.edu.cn)

Contents of this file

S1. Site description

The observation site was located on the rooftop of a building (~15 m above the ground) in the main campus of Chongqing University (29.57°N, 106.46°E) in the urban center of Chongqing, southwest China. The site is characterized by a typical residential and commercial environment, mainly influenced by local emissions (e.g., traffic, cooking). All instruments were installed in an air-conditioned room, with the room temperature maintained about 25℃. The ambient air was sampled at a flowrate of 16.7 LPM through a $PM_{2.5}$ impactor (model 2000-30EH, URG Inc.) and dried with a Nafion dryer (model MD-700, Perma Pure LLC), to achieve a low relative humidity level (RH <35%) prior to the online aerosol size distribution, optical and hygroscopic measurements. During the observation period, urban Chongqing suffered a rare heatwave. The mean temperature and relative humidity during the study period and the same period from 2011 to 2021 in urban Chongqing are given in Figure S1. Based on the method proposed by Nairn and Fawcett (2014), the Excess Heat Factor (EHF) metric was accordingly calculated for this study (Figure S2a).

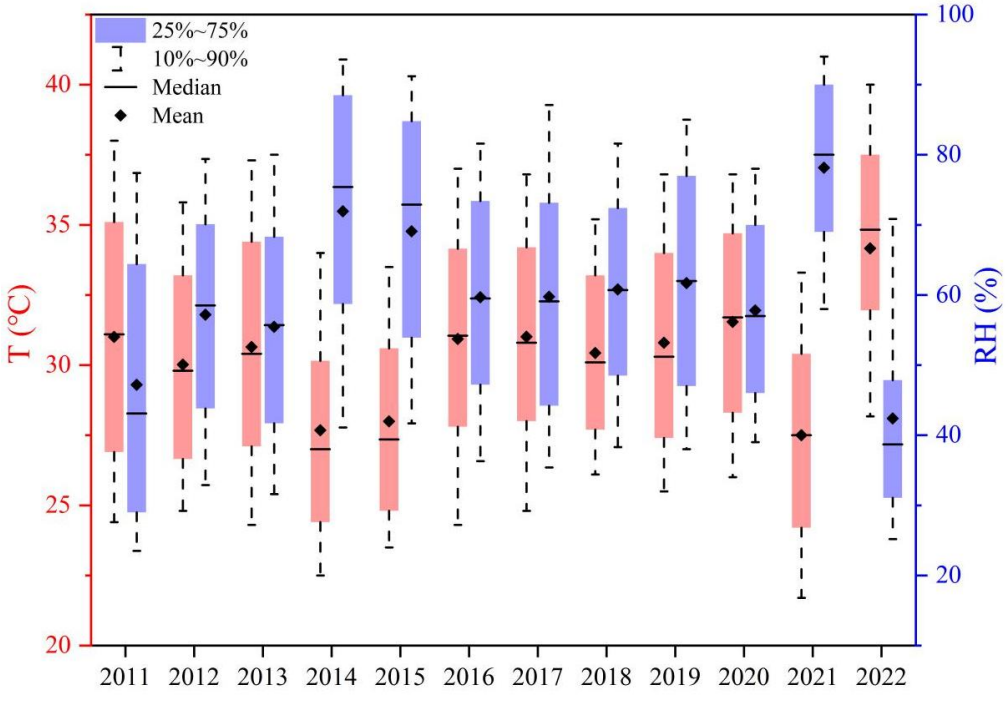

Figure S1. The variation trends of annual temperature and RH during the study period in 2022 and the same period from 2011 to 2021 in urban Chongqing.

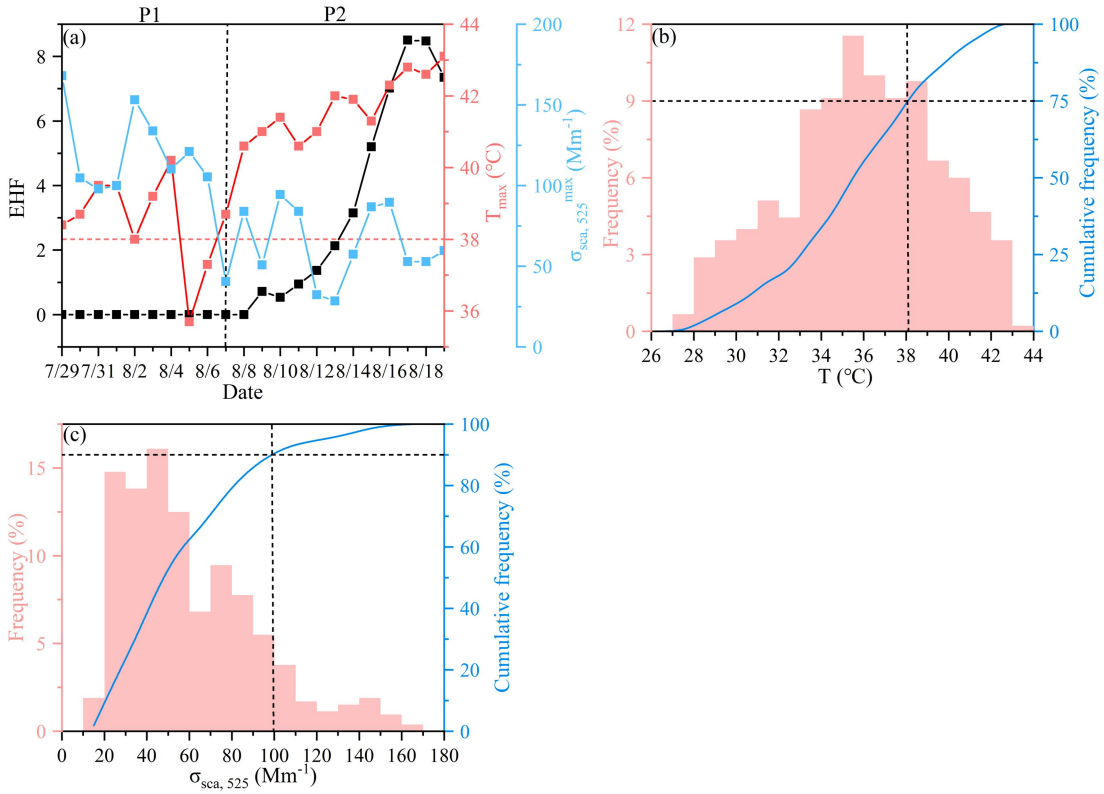

Figure S2. (a) Time series of calculated EHF, along with the daily maximum temperature (T_{max}) and dry $\sigma_{sca,525}$ results, during the study period. The corresponding occurrence frequency and cumulative frequency of hourly **(b)** temperature and **(c)** $\sigma_{sca,525}$ data records.

S2. Derivation of aerosol liquid water content (ALWC)

In this study, ALWC was determined as the discrepancy in aerosol volume concentration between the humidified and dry particles:

$$\mathrm{ALWC} = \mathrm{V_{dry}} \times \left(f_{\mathrm{v}}(\mathrm{RH}) - 1 \right) \quad (1)$$

where the dry aerosol volume concentration ($\mathrm{V_{dry}}$) was estimated with the dry scattering coefficients at three wavelengths utilizing a machine learning method (Kuang et al., 2018). Given the dependence on aerosol hygroscopicity and size distribution, the aerosol volume growth factor ($f_{\mathrm{V}}(\mathrm{RH})$) can be obtained from the observed $f(\mathrm{RH})$ and SAE (a proxy of aerosol size distribution) with the humidified nephelometer system (Kuang et al., 2018). Accordingly, the fraction of aerosol water content (f_{W}) upon hydration could be expressed as:

$$f_{\mathrm{W}} = \frac{\mathrm{ALWC}}{\mathrm{ALWC} + \mathrm{V_{dry}}} \quad (2)$$

Both dry and humidified nephelometers were calibrated before the measurement for the zero/span check with the particle-free air/standard gas (R134a), following standard calibration procedures. More detailed descriptions about the home-built humidified nephelometer system can refer to Kuang et al. (2017, 2020) and Xue et al. (2022).

S3. Offline particle sampling and chemical analysis

Total suspended particle (TSP) filter samples were collected by a moderate volume air sampler at a flow rate of 200 L/min from August 5 to 19, 2022. Daily (from 9:30 a.m. to 9:00 a.m. of the next day) integrated ambient TSP samples were collected on prebaked (600℃, 5h) quartz-fiber filters (90 mm, Whatman) for water-soluble ions, organic carbon (OC), and elemental carbon (EC) analysis.

Water-soluble inorganic anions (i.e., SO_4^{2-}, NO_3^-, Cl^- and F^-) and cations (i.e., NH_4^+, Na^+, Mg^{2+}, $Ca^{2+}$and K^+) were quantified using an ion chromatograph analyzer (Dionex 600, Dionex, USA) following standard procedures (Peng et al., 2019; Wang et al., 2018). Elemental carbon (EC) and organic carbon (OC) in the collected TSP samples were analyzed using a DRI Model 2015 Multi-wavelength Carbon Analyzer (Magee Scientific, USA). The methodology for OC/EC analysis was based on the thermal-optical reflectance (TOR) method following the Interagency Monitoring of Protected Visual Environments (IMPROVE-A) protocol, as shown in Chow et al. (2007, 2011) and Peng et al. (2020). The secondary organic carbon (SOC) can be estimated with the obtained OC and EC data according to the EC-tracer method (Castro et al., 1999; Strader et al., 1999), details of which was also available in our previous study (Hao et al., 2024).

The chemical components mass concentration and mass fraction in TSP, as well as the $PM_{2.5}$ (PM_{10}) mass concentration and the ratio of SOC/TOC during the study period are depicted in Figure S3.

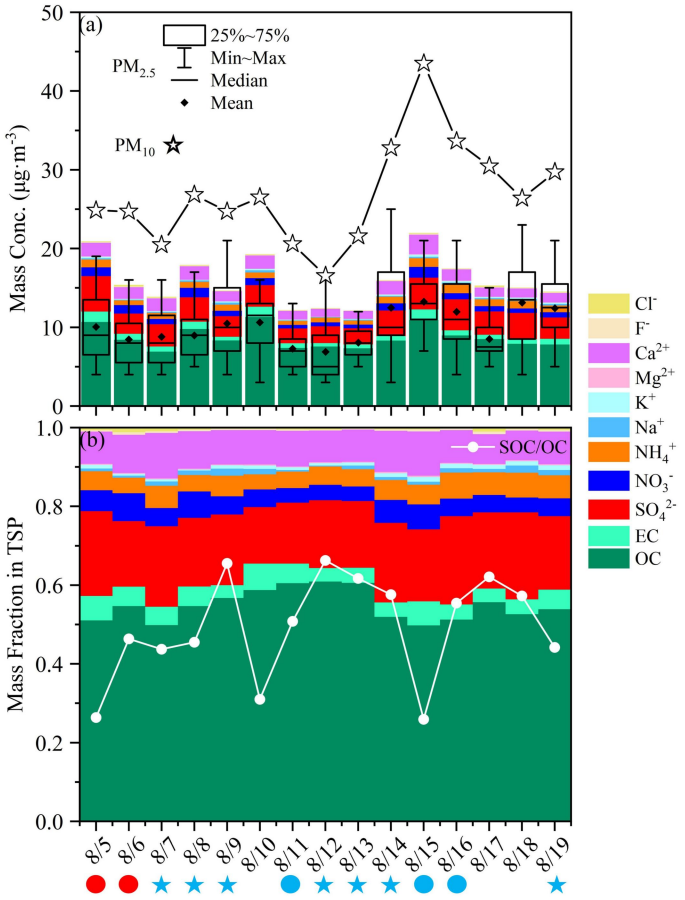

Figure S3. The mass concentration **(a)** and mass fraction **(b)** of chemical components in TSP (total suspended particulates) during the study period. The black stars, box plots and white line stands for daily mean PM_{10}, $PM_{2.5}$ and SOC/OC, respectively. The red or blue circle symbols below specific dates represent the P1 or P2 non-event days, and the blue stars represent the P2 ~~$NPF_{C,\ HW}$~~ $NPF_{clean,\ HW}$ days.

S4. Meteorological and air quality data

All the contemporary hourly meteorological datasets including relative humidity (RH), temperature (T), visibility (VIS), wind speed (WS), wind direction (WD), precipitation were obtained from the Integrated Surface Database from the U.S. National Centers for Environmental Information (https://ncdc.noaa.gov/isd) (Wan et al., 2023; Xu et al., 2020), and the mixing layer height (MLH) data were achieved from China Meteorological Administration in this study. Ultraviolet (UV) radiation data were downloaded from European Centre for Medium-Range Weather Forecasts (https://cds.climate.copernicus.eu/).

Hourly air pollutant datasets including $PM_{2.5}$, PM_{10}, NO_2, SO_2, CO and O_3 were achieved from the China National Environmental Monitoring Center (http://www.cnemc.cn/en). The gas-phase sulfuric acid, known as the most ubiquitous and key precursor for NPF, was estimated with the UVB (UVB = 5%UV, Fitsiou et al., 2021) and SO_2 concentration (Lu et al., 2019):

$$H_2SO_4 = 280.05 \times UVB^{0.14} \times SO_2{}^{0.40} \quad (3)$$

S5. Particle number size distribution measurements

During the field observation, every 3-min PNSD and particle volume size distribution (PVSD) was measured by a SMPS, which consisted of a soft X-Ray neutralizer (model 3088, TSI Inc.), a differential mobility analyzer (model 3081, TSI Inc.), and a condensation particle counter (model 3775, TSI Inc.) (Dominick et al., 2018; Rissler et al., 2006). The SMPS was operated at a sheath/sample flow rate of 3.0/0.3 LPM, and the detected size range was 14.1-710.5 nm with 110 size bins. Data inversion of measured particle size distributions was achieved with the Aerosol Instrument Manager software (AIM, TSI Inc.), including the multiple charge and diffusion corrections (Denjean et al., 2015; Rosati et al., 2022).

The aerosol effective radius (R_{eff}) is a crucial parameter regulating optical properties (e.g., light scattering) of the aerosol population (Hansen and Travis, 1974; Grainger et al., 1995). It can be calculated with the measured size distribution as below (Hansen and Travis, 1974; Grainger et al., 1995):

$$R_{eff} = \frac{\int D_P^3 n(\log D_P)\, d\log D_P}{\int D_P^2 n(\log D_P)\, d\log D_P} \quad (4)$$

where $n(\log D_P)$ is the particle number size distribution in log scale.

Using the measured PNSD data, NPF events were identified according to the criteria raised by Dal Maso et al. (2005), and the key parameters related to NPF events (e.g., formation rate (FR) and growth rate (GR) of new particles, condensation sink (CS) and coagulation sink (CoagS)) could be derived following the methodologies introduced by Dal Maso et al. (2005) and Kulmala et al. (2012).

The specific dates for NPF and non-event classifications were summarized in Table S1, and the frequencies of NPF, non-event and Undefined days during both periods were shown in Figure S4a. By using the HYSPLIT (Hybrid Single-Particle Lagrangian Integrated Trajectory) 4 model developed by NOAA (Stein et al., 2015), the 48-h and 72-h back trajectories of air masses at 500 or 1000 m altitude above the observation site during this study period were calculated and visualized by MeteoInfoMap (version 3.9.9; Figure S4b) (Chen et al., 2021; Tian et al., 2021; Wang, 2014).

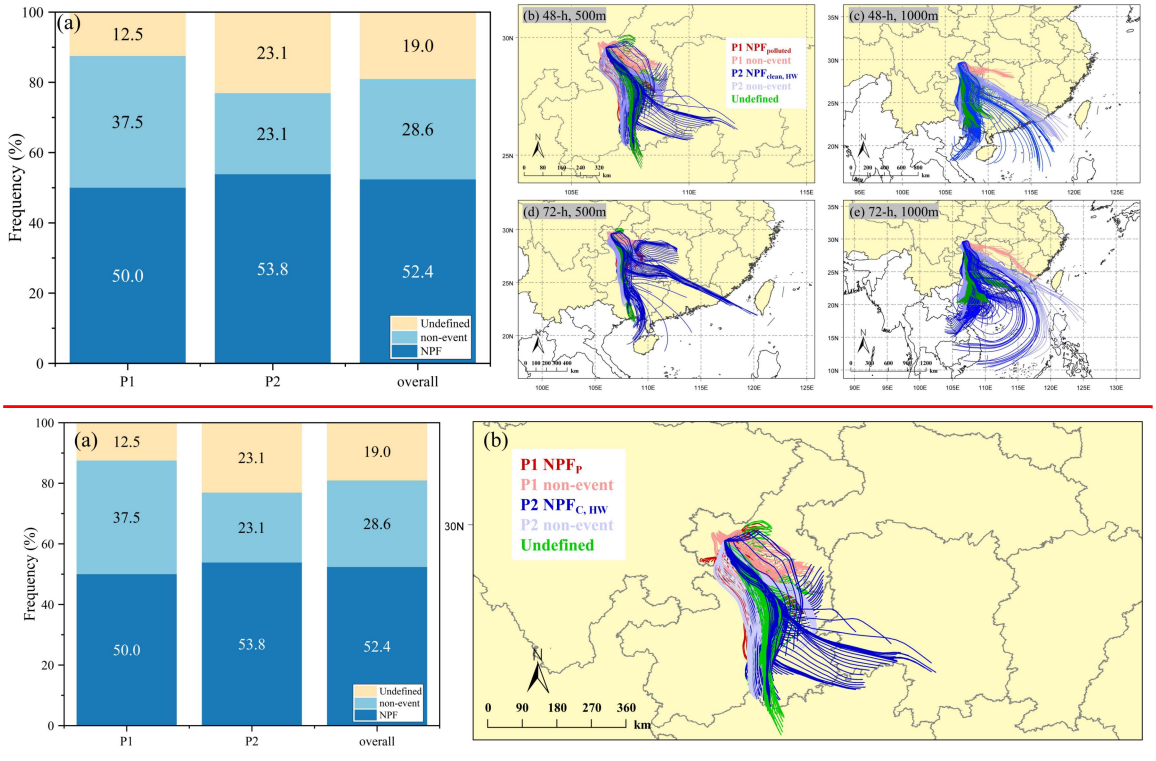

Figure S4. (a) The occurrence frequencies of NPF, non-event and Undefined days during P1, P2 and the whole observation periods. **(b-e)** The 48-h and 72-h air-mass back trajectories at 500 or 1000 m altitude during the study period.

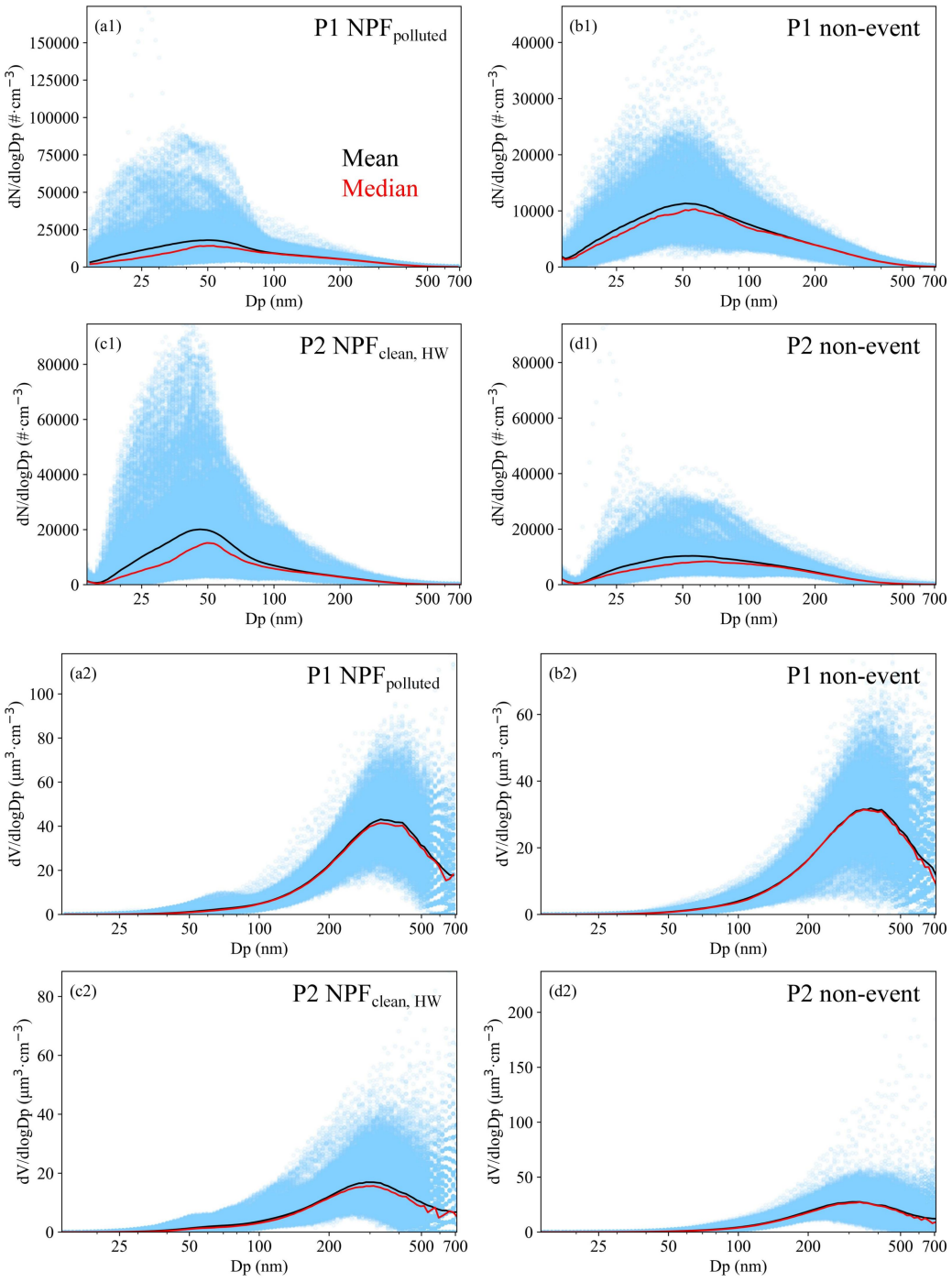
(a1)
P1 NPF$_{polluted}$
Mean
Median
dN/dlogDp (#·cm^{-3})
Dp (nm)
(b1)
P1 non-event
(c1)
P2 NPF$_{clean, HW}$
(d1)
P2 non-event
(a2)
dV/dlogDp (μm^3·cm^{-3})
(b2)
(c2)
(d2)
25
50
100
200
500
700

144

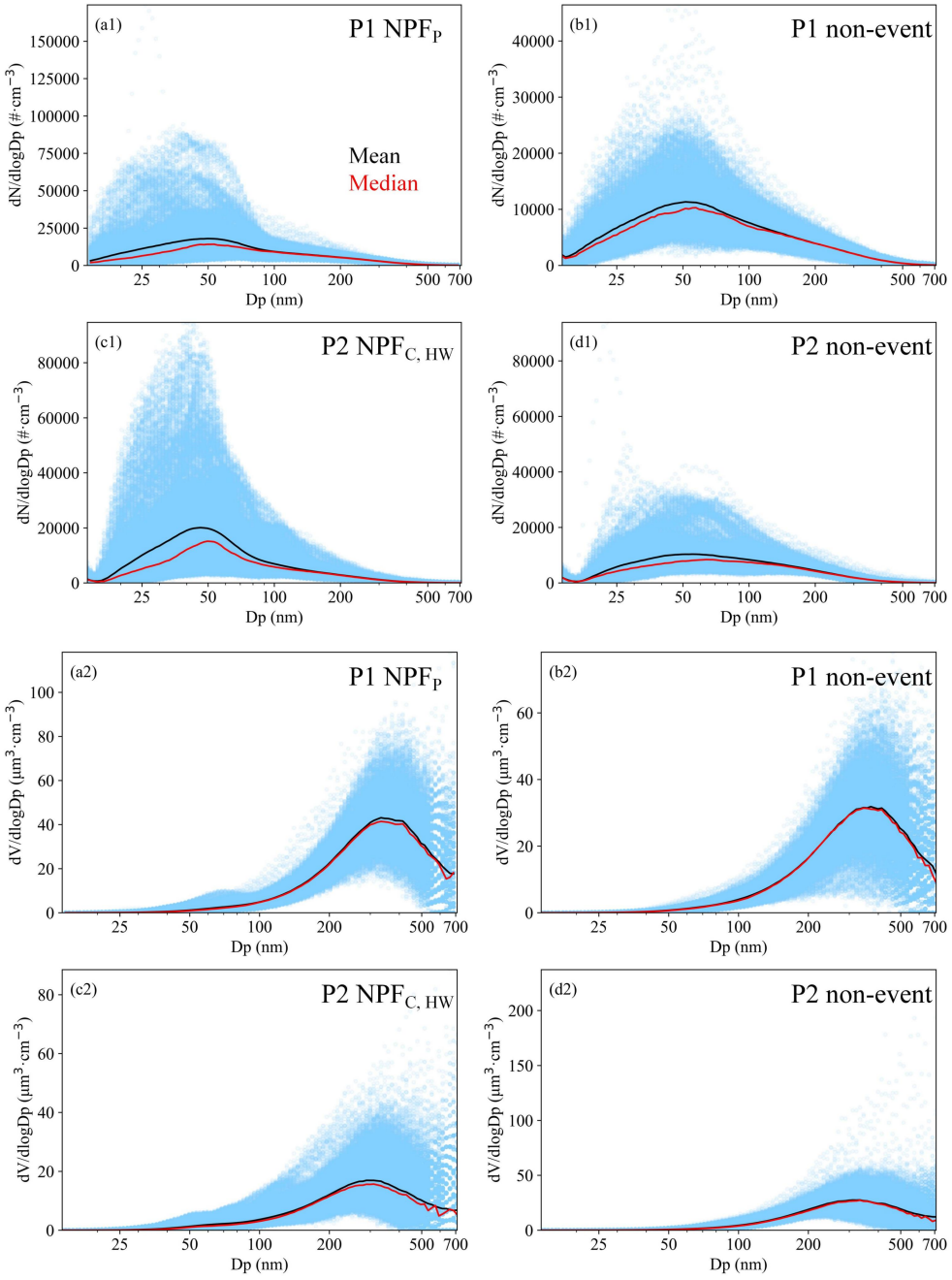

145

146 **Figure S5.** The PNSDs **(a1-d1)** and PVSDs **(a2-d2)** for different event categories. The

147 black~~red~~ and red~~blue~~ lines represent the mean and median values, respectively.

The diurnal variations of PNSD, R_{eff}, particle mode diameter (D_{mode}), as well as CS, were given in Figure S6.

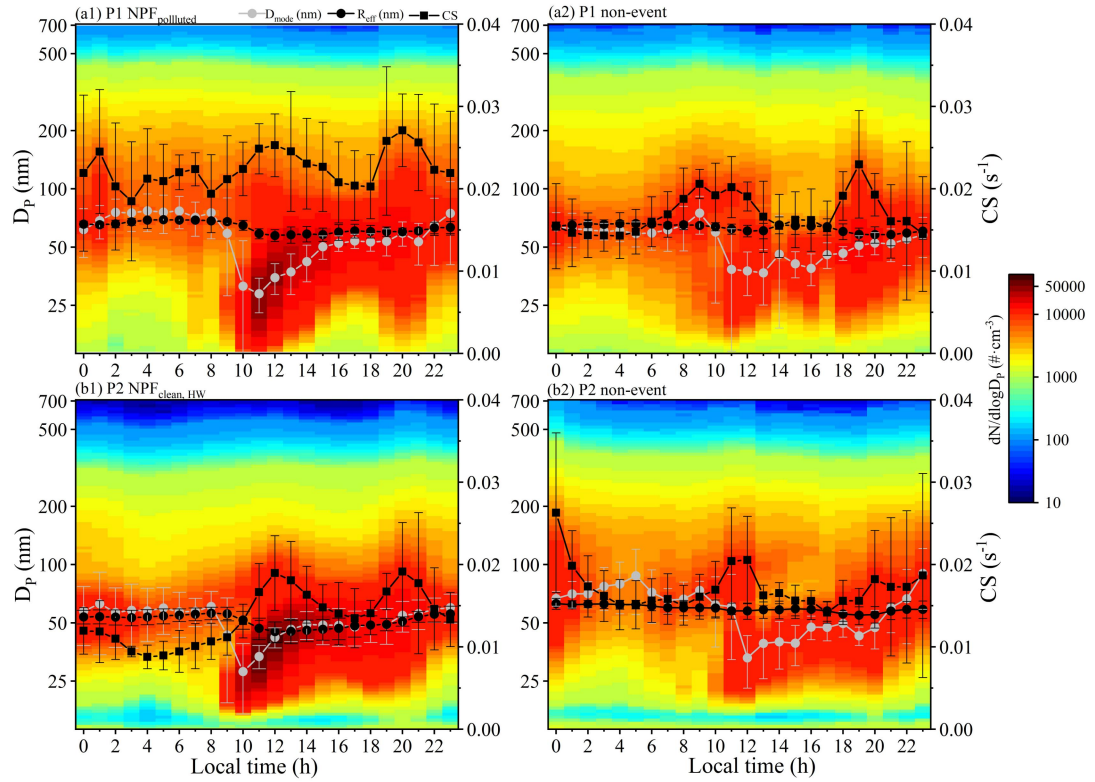

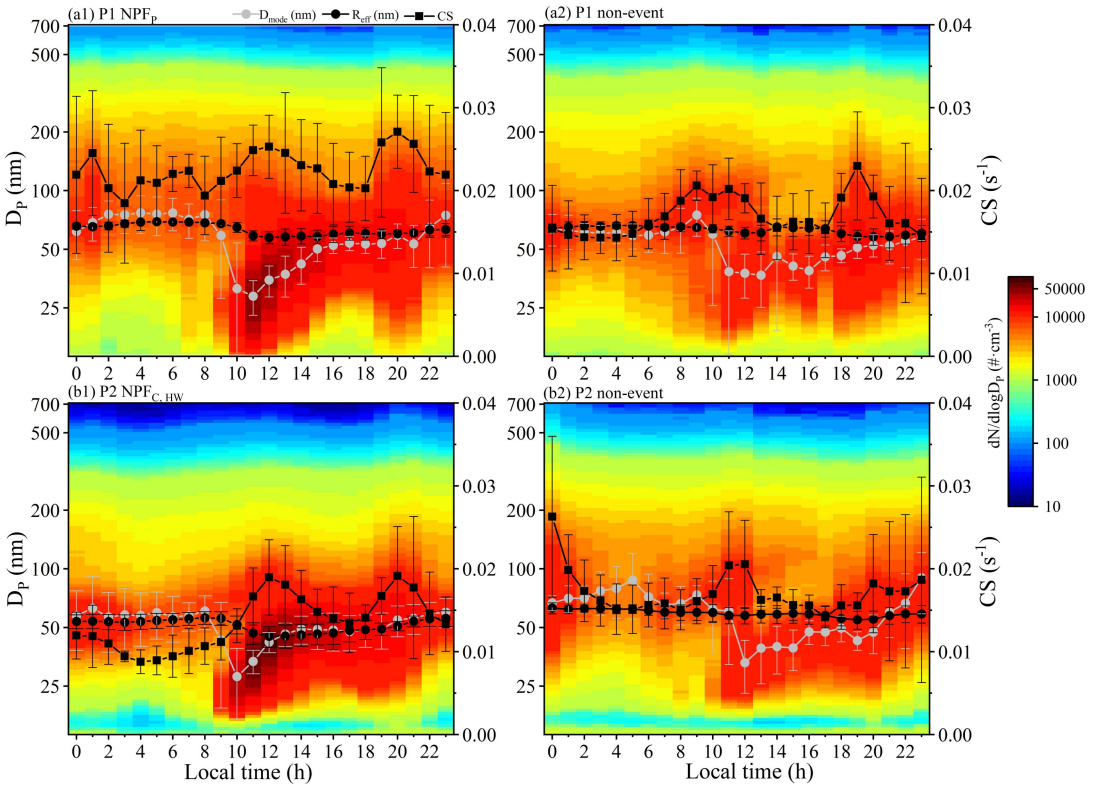

Figure S6. Diurnal variations of PNSDs, D_{mode}, R_{eff}, and CS during P1 and P2 NPF days **(a1, b1)** and non-event days **(a2, b2)**, the error bars stand for ± one standard deviations.

The PNSD is typically categorized into three modes: the nucleation mode (D_p <25 nm), Aitken mode (25-100 nm), and accumulation mode (D_p >100 nm) (Zhu et al., 2021). The number concentrations and volume concentrations of different mode particles for different event categories are shown in Figure S7. The diurnal variations of aerosol number and volume concentrations, as well as R_{eff}, for different modes on NPF event days are illustrated in Figure S~~7~~8.

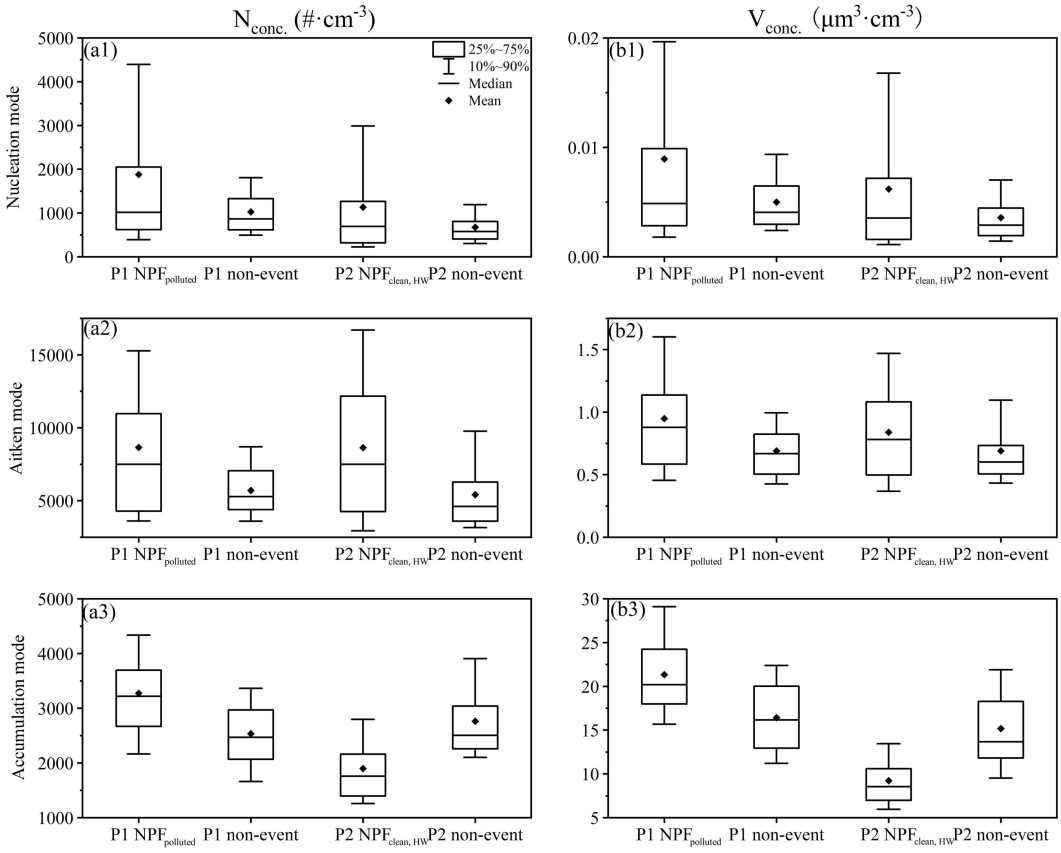

Figure S7. The number concentrations (left column: a1-a3) and volume concentrations (right column: b1-b3) of different mode particles for different event categories.

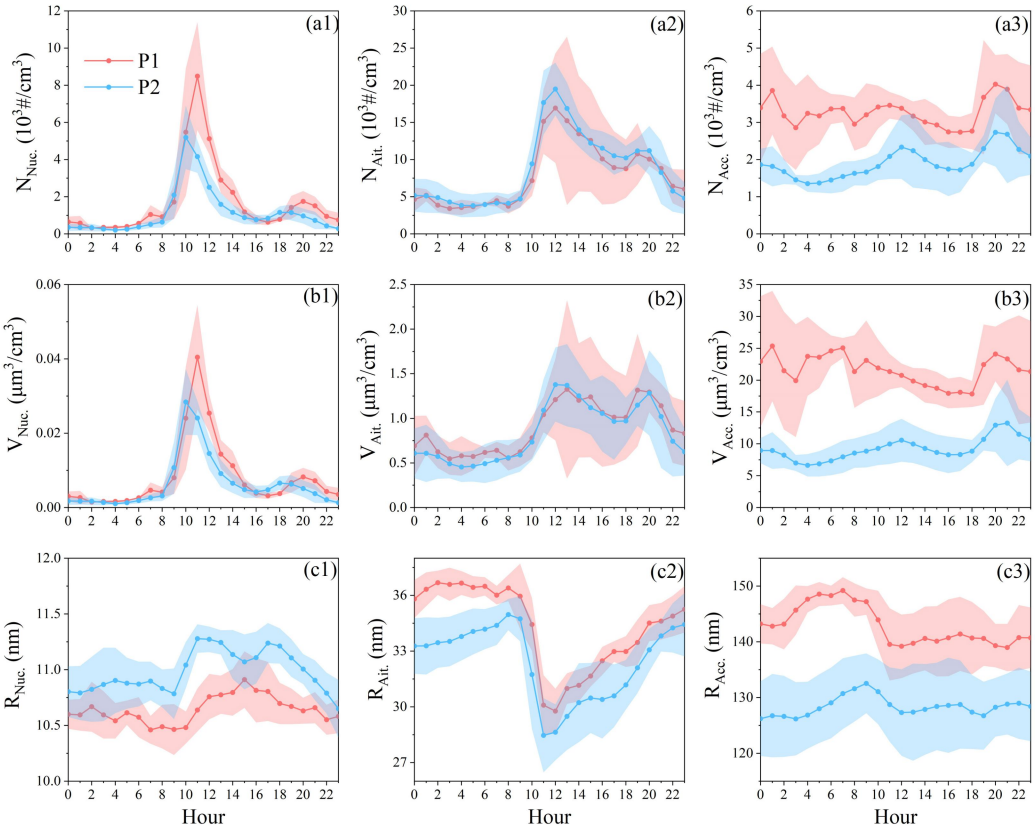

Figure S~~7~~8. Diurnal variations of the number (**a1-a3**), volume (**b1-b3**) concentration and effective radius (**c1-c3**) of nucleation mode (left column), Aitken mode (middle column), and accumulation mode (right column) particles on NPF event days during P1 (red line) and P2 (blue line) periods. The shaded areas stand for the corresponding ± 1σ standard deviations.

The specific start and end time of NPF, along with the subsequent growth end time during NPF events were displayed in Figure S~~8~~9. The NPF event end time is defined as the moment when the formation of new nucleation-mode particles (diameter <25 nm) ceases, specifically identified by the absence of a notable increase in sub-25 nm particles (Dal Maso et al., 2005; Hamed et al., 2007; Kerminen et al., 2018). The growth event end time refers to the time when the newly formed particles stop growing, typically due to the depletion of low-volatility vapors or particle coagulation (Dal Maso et al., 2005; Kerminen et al., 2018). This can be observed as the stabilization of particle diameters in the Aitken/accumulation mode, marked by a flattening of the growth trajectory in the PNSD plot (Figure 1i).

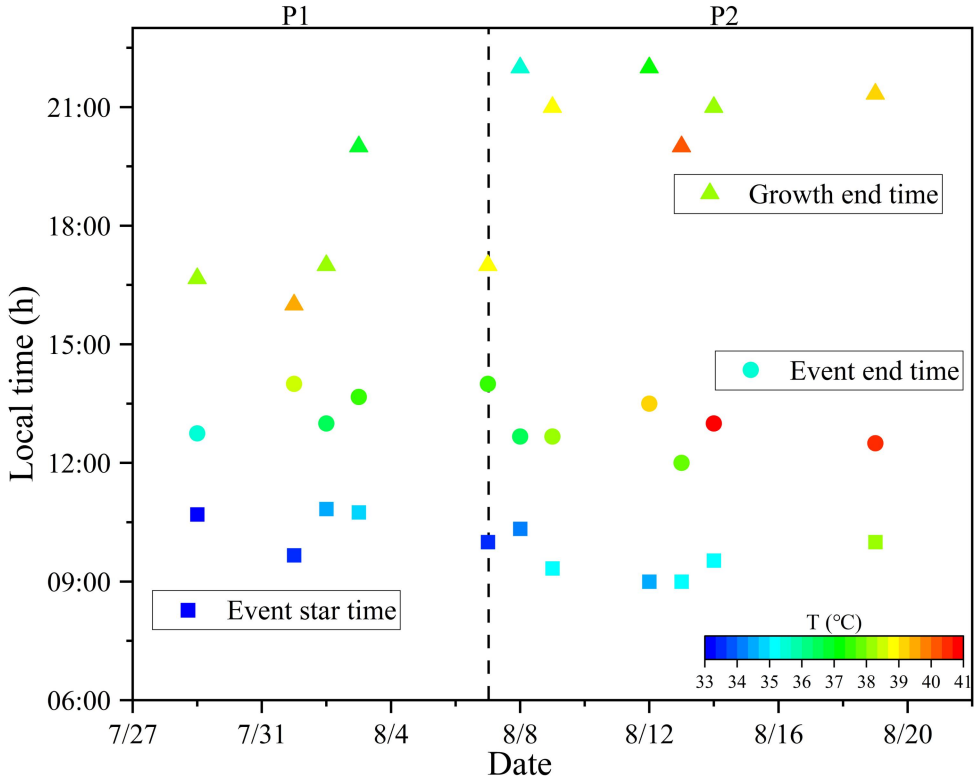

Figure S~~8~~9. The start and end time of NPF, along with the subsequent growth end time and their corresponding temperature levels during NPF events.

S6. Diurnal variations of humidified nephelometer system related parameters on non-event days during both P1 and P2 periods

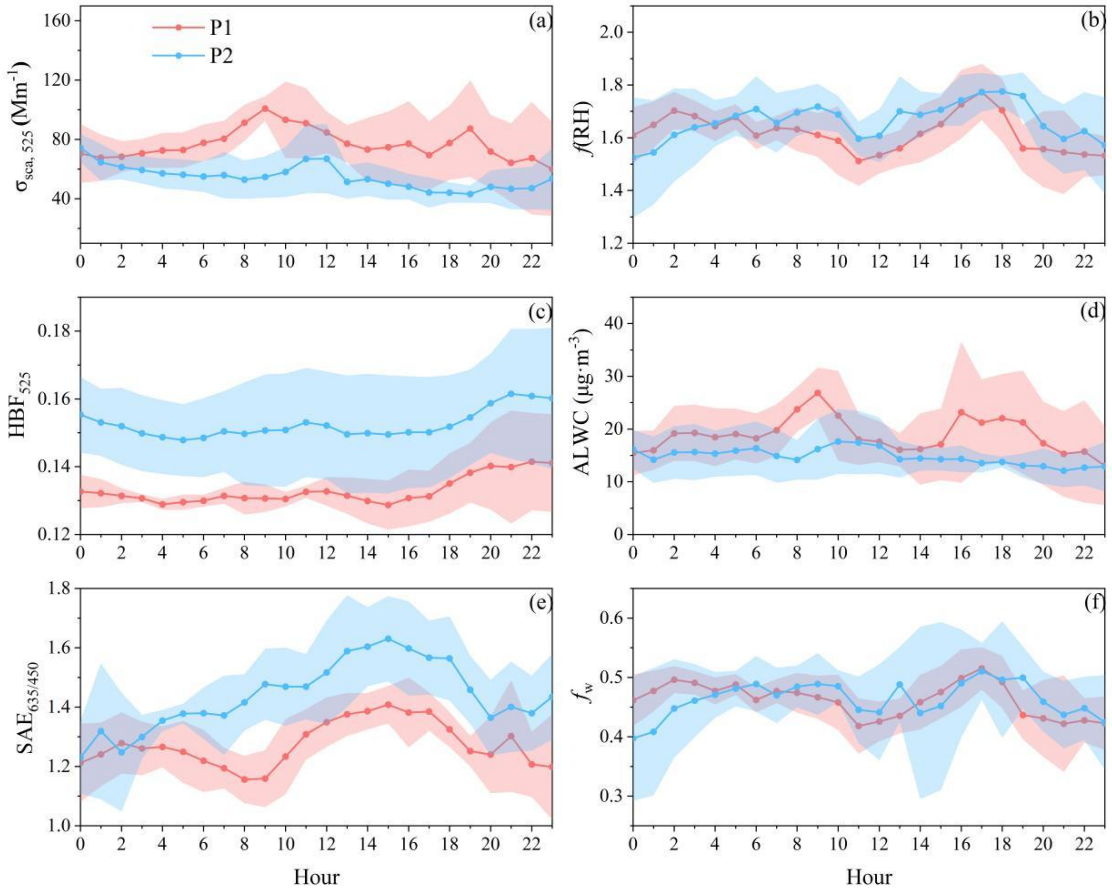

Figure S910. Diurnal variations of $\sigma_{sca,\ 525}$ **(a)**, f(RH) **(b)**, HBF$_{525}$ **(c)**, ALWC **(d)**, SAE$_{635/450}$ **(e)** and f_W **(f)** on non-event days during P1 (red line) and P2 (blue line) periods. The shaded areas stand for the corresponding ± 1σ standard deviations.

S7. Calculation of $\sigma_{sca,\ 525}$ and HBF with the Mie theory and measured PNSD

The size-dependent efficiencies of σ_{sca}, σ_{bsca} and HBF in dry conditions, as well as the corresponding enhancements in these efficiencies of a single particle upon hydration at λ = 525 nm could be simulated using the Mie model. Aerosol diameter growth factor (g(RH)) is normally determined by the aerosol hygroscopicity parameter κ (Brock et al., 2016; Tan et al., 2024). The bulk aerosol $\kappa_{f(RH)}$ of this study could be derived from the f(RH) measurements based on the method proposed by Kuang et al. (2017). The aerosol population was typically divided into the ultrafine (D_p <100 nm; Uf.) and accumulation (D_p ≥100 nm; Acc.) modes (Fig. S5). Although the size-resolved κ results were unavailable, the mean κ_i for both Uf. and Acc. mode particles could be roughly estimated assuming that $\kappa_{f(RH)}$ is a linear combination of volume-weighted κ_i for different modes (Hong et al., 2024). Since the hygroscopicity for Uf. mode was generally weaker (Chen et al., 2012; Petters and Kreidenweis, 2007), the mean $\kappa_{Uf.}$ was defined to be half of the measured bulk $\kappa_{f(RH)}$, and $\kappa_{Acc.}$ can be derived from the bulk $\kappa_{f(RH)}$ with the measured $VF_{Uf.}$ and $VF_{Acc.}$. Consequently, the corresponding g(RH) for both Uf. and Acc. modes can be calculated with the κ-Köhler theory. The complex refractive index is another critical input parameter for the Mie model, with the real part of complex refractive index (n) determining the aerosol light scattering ability. Under the assumption of a fixed n for dry aerosols (n_{dry} = 1.53) in this study, the volume-weighted n of hydrated particles can be derived with n_{dry} and f(RH)-derived volume fractions of uptake water, f_W and the n of pure water (1.33; Jung et al., 2016) (Chen et al., 2012). Hence, the efficiencies of σ_{sca}, σ_{bsca} and HBF after hygroscopic growth could be simulated with the time-averaged dry PNSD, the mean g(RH) of Uf. Mode (1.15) and Acc. mode (1.27), and the mean n of humidified aerosols (1.44) for the observation period. The theoretically simulated results are displayed in Figure S11.

~~Based on the Mie theory and measured PNSD, the σ_{sca} and σ_{bsca} for λ = 525 nm and a fixed refractive index of 1.53 + 0.1i were calculated, with good agreements between the theoretically calculated and measured values (R^2 = 0.99 for $\sigma_{sca,\ 525}$; R^2 = 0.98 for $\sigma_{bsca,\ 525}$). The size-dependent σ_{sca}, σ_{bsca} and HBF efficiencies simulated from Mie theory are shown in Figure S10~~1a. A good correlation between SMPS-determined particle volume concentration and the measured $\sigma_{sca,\ 525}$ is also observed in Figure S1~~1~~2. The size-

resolved $\sigma_{sca,\ 525}$ distributions and size-resolved $\sigma_{sca,\ 525}$ cumulative frequency distribution on NPF event (non-event) days during P1 and P2 periods are displayed in Figure S1~~2~~3.

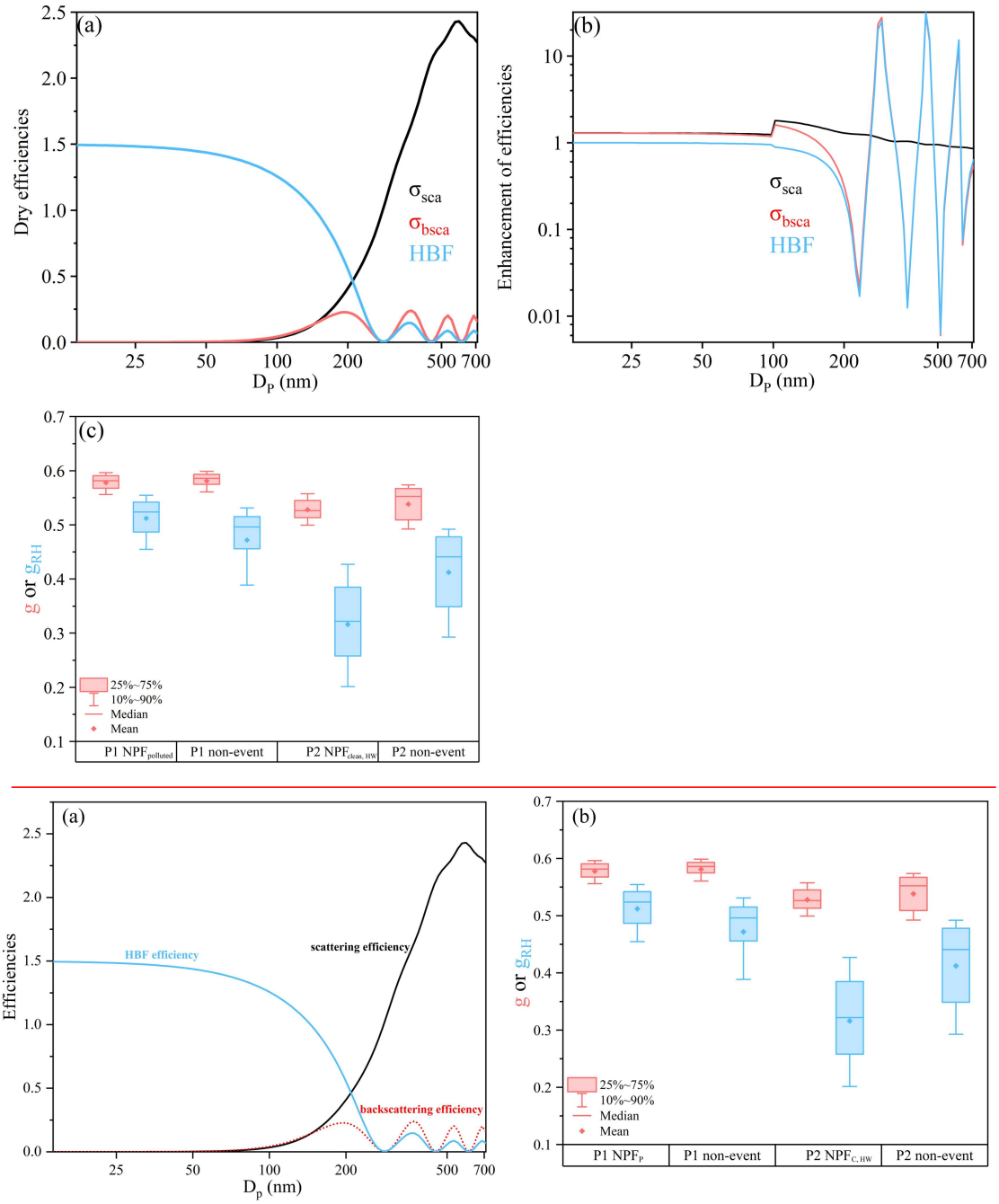

Figure S1~~0~~1. ~~(a)~~ Size-dependent efficiencies of **(a)** light scattering (the black line), backscattering (~~dashed~~ the red line) and HBF (the blue line) ~~efficiencies~~in dry conditions, as well as **(b)** the enhancements in corresponding efficiencies of light scattering (the black line), backscattering (the red line) and HBF (the blue line) at λ = 525 nm simulated

fromwith the Mie theory for the case of λ = 525 nm and refractive index of 1.53 + 0.1i.

(bc) The box plots of the HBF_{525} ($HBF_{525,\,RH}$) derived asymmetry factor g (g_{RH}).

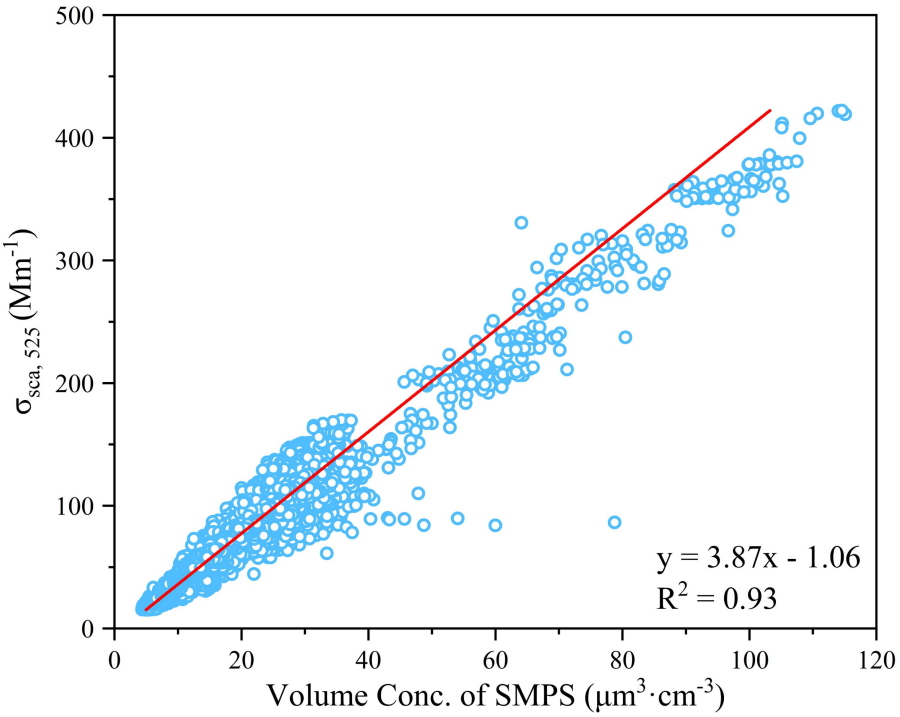

Figure S1~~1~~2. Correlation between the particle volume concentration determined by SMPS and $\sigma_{sca,\ 525}$ measured by the humidified nephelometer system during the study period. The solid line represents the fitting line.

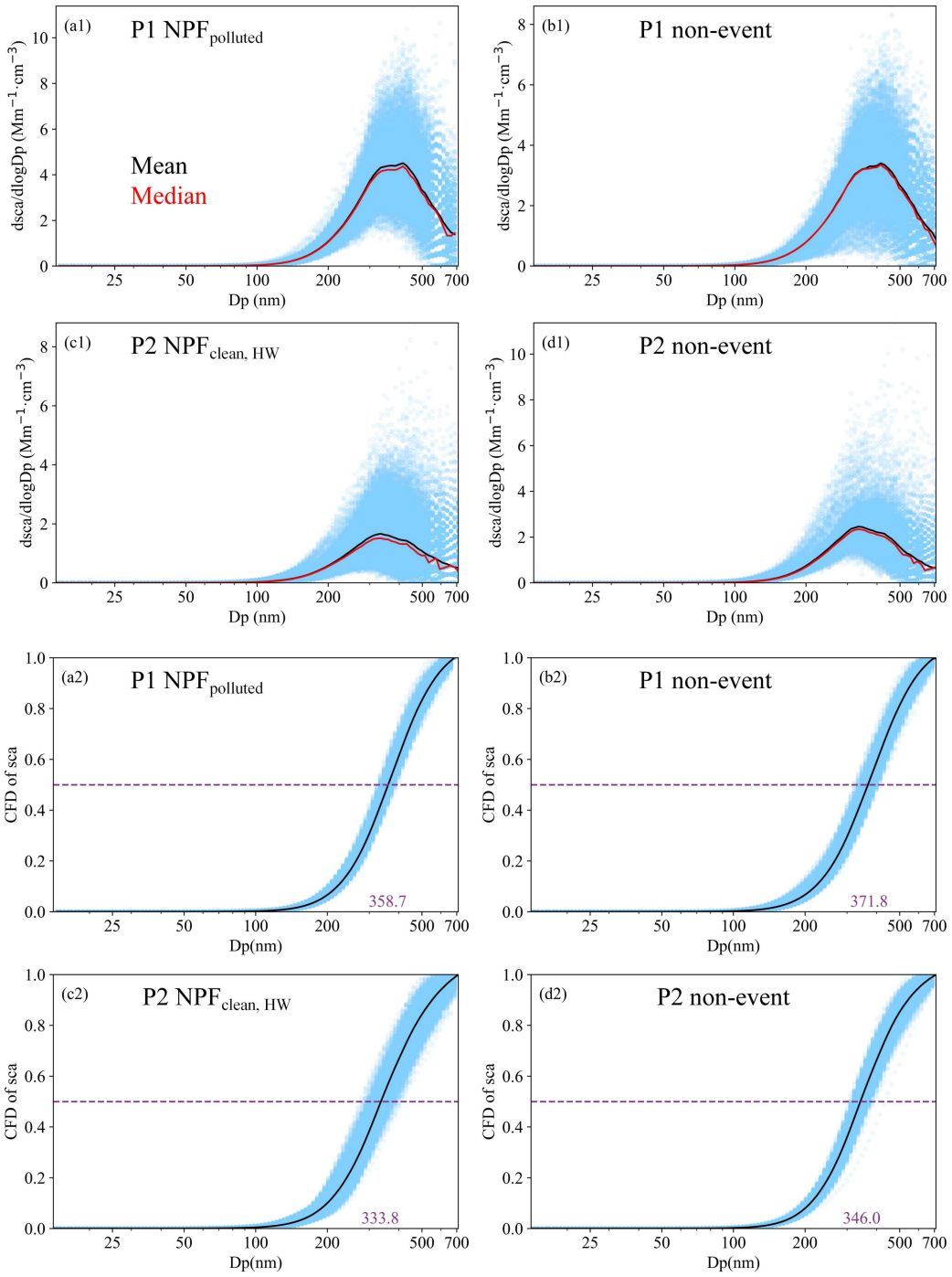
(a1)
P1 NPF$_{polluted}$
Mean
Median
dsca/dlogDp (Mm^{-1}·cm^{-3})
Dp (nm)
(b1)
P1 non-event
(c1)
P2 NPF$_{clean, HW}$
(d1)
P2 non-event
(a2)
CFD of sca
Dp(nm)
358.7
(b2)
371.8
(c2)
333.8
(d2)
346.0

234

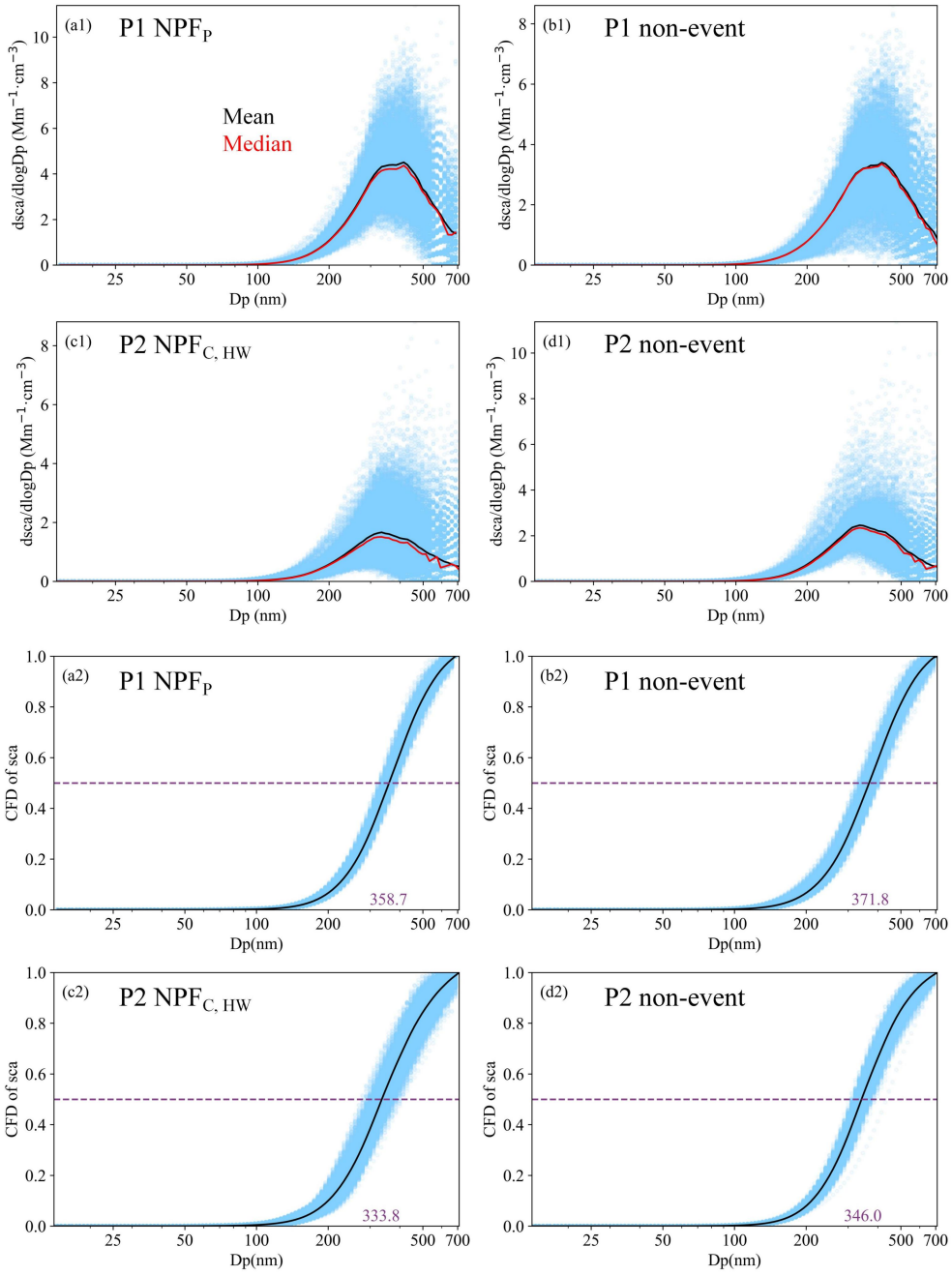

Figure S1~~2~~3. The size-resolved $\sigma_{sca,\ 525}$ distributions **(a1-d1)** and size-resolved $\sigma_{sca,\ 525}$ cumulative frequency distribution **(a2-d2)** for different event categories. The ~~red~~black and red~~blue~~ lines represent the mean and median values, the purple dashed line and the purple numbers on the abscissa represent the 50% cumulative frequency and the corresponding particle size (D_{50}), respectively.

S8. Correlation coefficients between different PNSD-related parameters, temperature, O_3/O_X, aerosol optical and hygroscopic properties on NPF (non-event) days during either P1 or P2 period

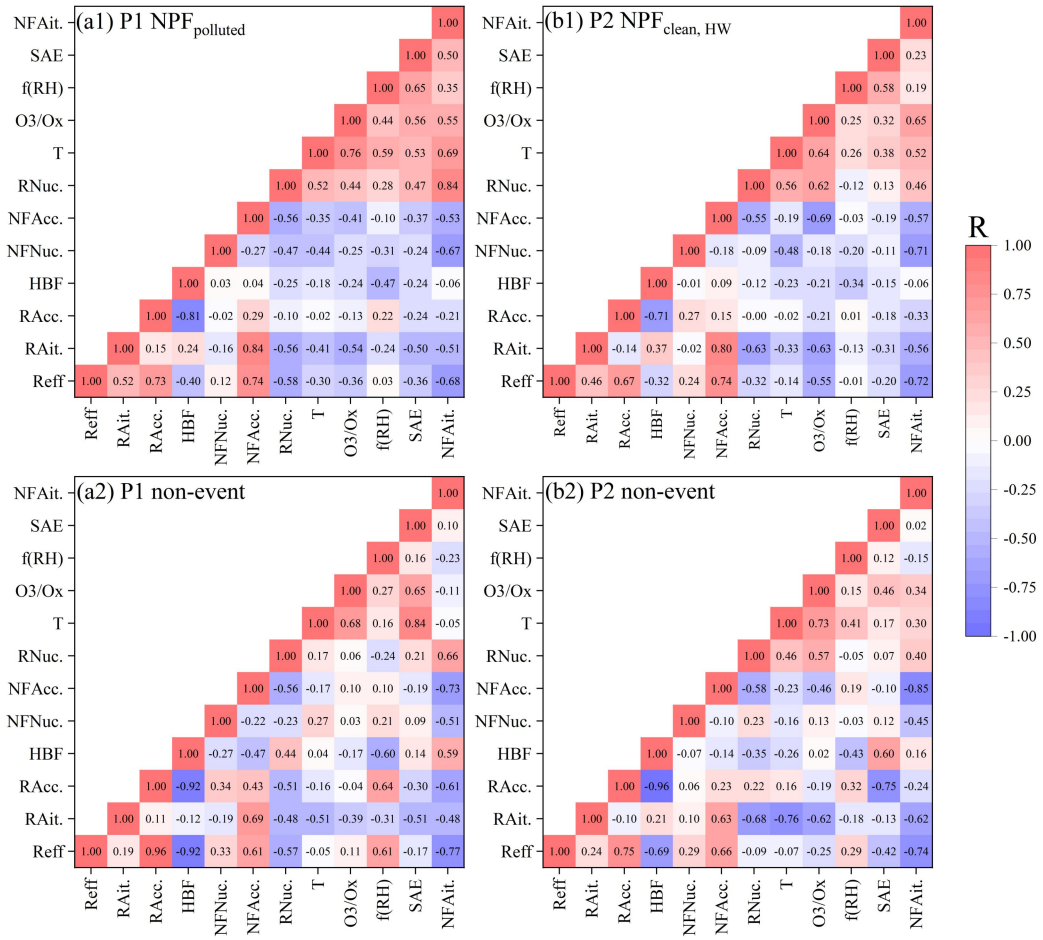
(a1) P1 NPF polluted
(b1) P2 NPF clean, HW
(a2) P1 non-event
(b2) P2 non-event
NFAit.
SAE
f(RH)
O3/Ox
T
RNuc.
NFAcc.
NFNuc.
HBF
RAcc.
RAit.
Reff
R
1.00
0.75
0.50
0.25
0.00
-0.25
-0.50
-0.75
-1.00

244

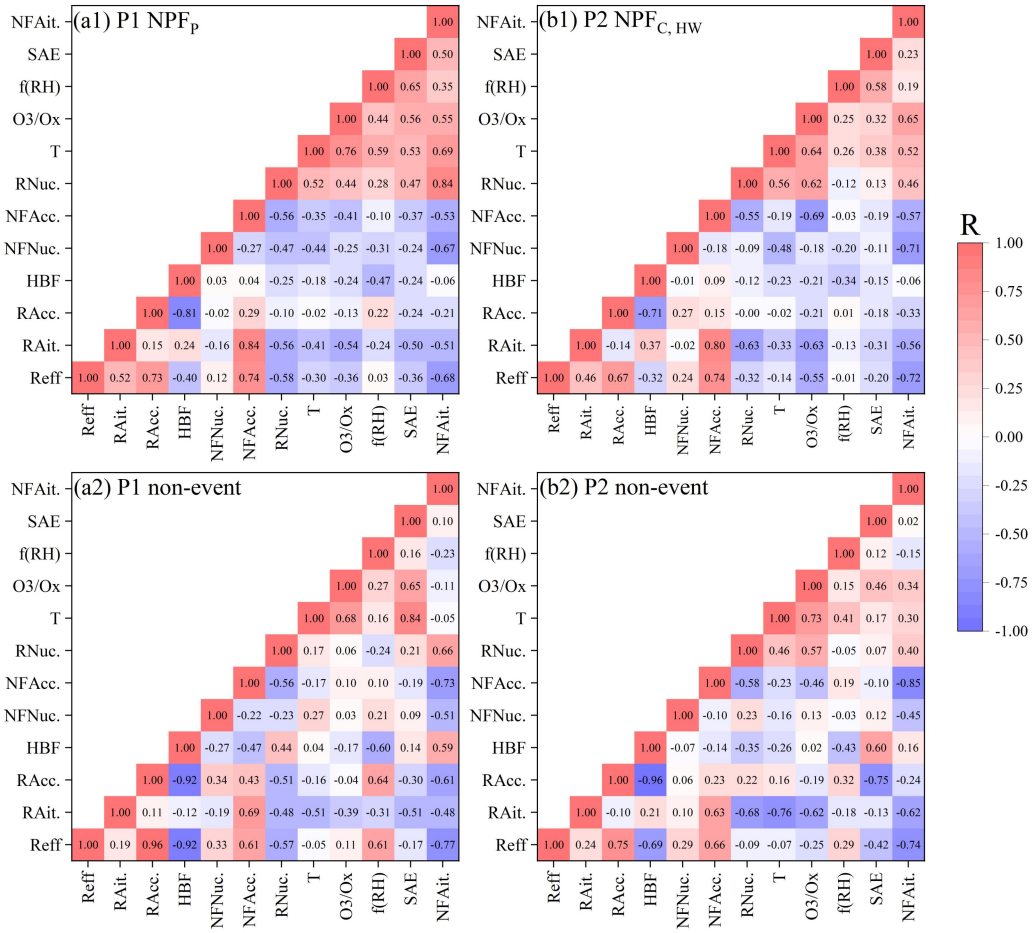

Figure S134. Correlation coefficients between different PNSD-related parameters (R_{eff}, $R_{Nuc.}$, $R_{Ait.}$, $R_{Acc.}$, $NF_{Nuc.}$, $NF_{Ait.}$, $NF_{Acc.}$), temperature (T), O_3/O_X, HBF, SAE, and *f*(RH) during NPF events **(a1, b1)** and non-event days **(a2, b2)** over the 08:00-22:00 LT time window.

S9.The sensitive test on dependences of the $HBF_{525,\ RH}/HBF_{525}$ ratio on the aerosol size distribution, hygroscopic growth, and complex refractive index

To investigate the distinct influences of PNSD, optical and hygroscopic properties on the $HBF_{525,\ RH}/HBF_{525}$ ratio, a sensitivity analysis with the measured data specifically for both P1 and P2 NPF days using the Mie model was conducted. Aerosol number size distributions could be assumed as a combination of multi-lognormal distribution functions, with each mode representing a distinct particle population (Hussein et al., 2004):

$$\frac{dN}{d\log D_P} = \sum_{i=1}^{n} \frac{N_{t,i}}{\sqrt{2\pi}\log\sigma_{g,i}} \exp\left[-\frac{(\log D_P - \log \overline{D_{Pg,i}})^2}{2\log^2\sigma_{g,i}}\right] \quad (5)$$

Where the three representative parameters, i.e., the total number concentration $N_{t,i}$, the geometric standard deviation (GSD) $\sigma_{g,i}$, and the geometrical mean diameter $D_{Pg,i}$, can be used to characterize an individual mode *i*; and n is the number of individual modes (Hussein et al., 2004). In this study, the measured PNSD data on NPF days during P1 and P2 periods were normally fitted into two modes: the predominant Uf. mode and the other one dominated by Acc. Mode particles (Fig. S5). Hence, nine parameters were employed in the Mie model: four parameter pairs (D_{Pg}, GSD, N_t and g(RH)) for both Uf. and Acc. mode particles, along with the mean *n* of the bulk aerosol population upon hydration. Further, the $HBF_{525,\ RH}/HBF_{525}$ can be simplified as a function of aerosol size distribution (i.e., D_{Pg}, GSD, N_t), water uptake (e.g., g(RH)), and *n* as below:

$$HBF_{525,\ RH}/HBF_{525} = f(D_{Pg}, GSD, N_t, g(RH), n) \quad (6)$$

The influence of a specific parameter on the $HBF_{525,\ RH}/HBF_{525}$ was evaluated by fixing all the other parameters at their measured mean values and computing $HBF_{525,\ RH}/HBF_{525}$ ratios across the range of this target parameter.

The measured mean value and variation range of each parameter were summarized in Table S3. The ranges of D_{Pg}, GSD, N_t and g(RH) were determined based on field measurements of this study. Zhao et al. (2021) reported that *n* of diverse aerosol populations could range from 1.36 to 1.78 across different Chinese cities, and this study constrained *n* to vary from 1.3 (nearly pure water of 1.33; Jung et al., 2016) to 1.8 (similar to black carbon of approximately 1.87; Schkolnik et al., 2007) in the modeling framework. The results are shown in Figures S15-16.

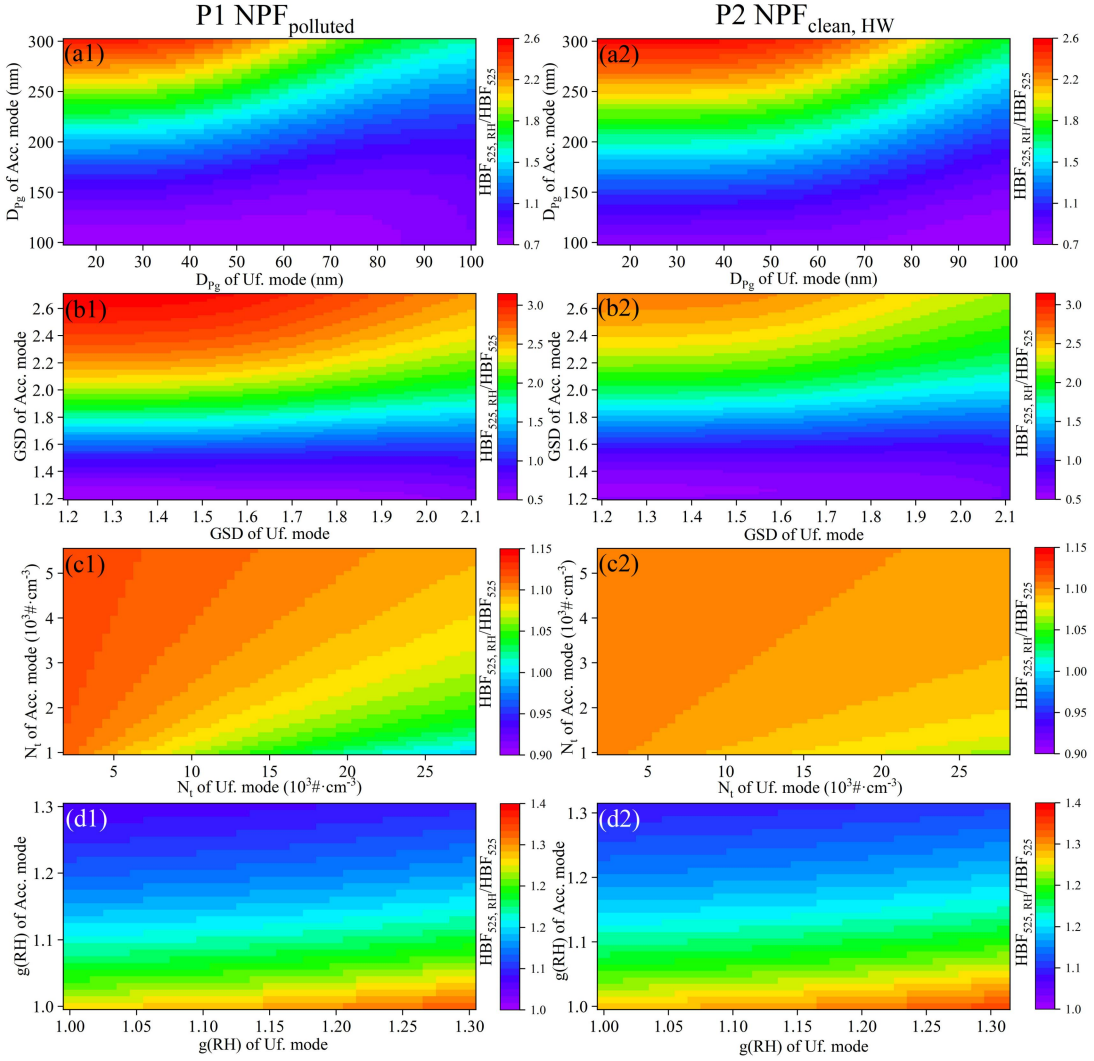

Figure S15. The relationships between the $HBF_{525,\ RH}/HBF_{525}$ ratios and the D_{pg} **(a)**, GSD **(b)**, N_t **(c)**, g(RH) **(d)** of two modes particleas. The left (right) column was corresponding to the P1 $NPF_{polluted}$ (P2 $NPF_{clean,\ HW}$) days.

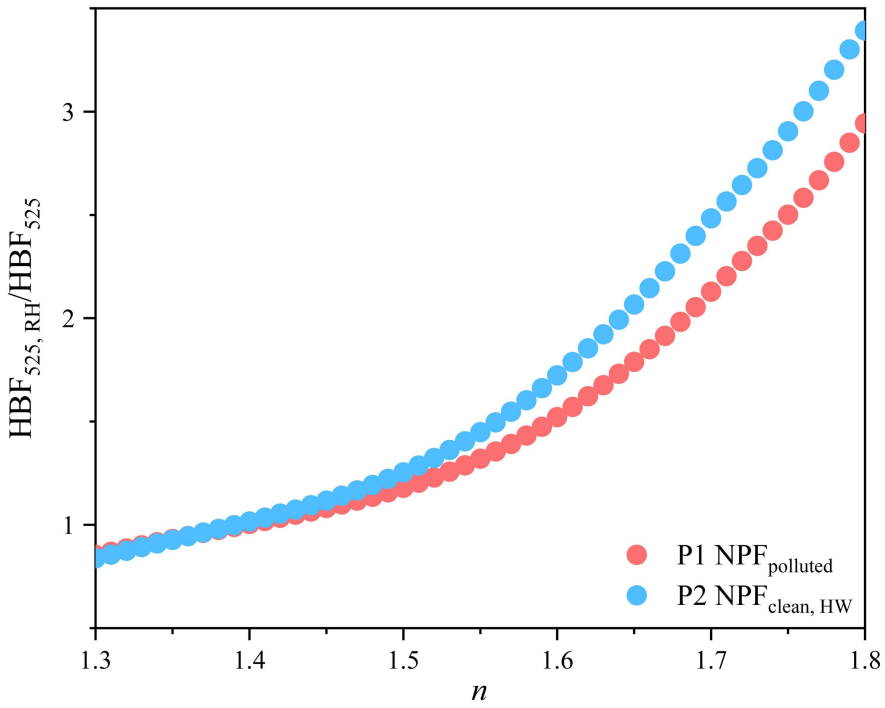

Figure S16. The variations of the $HBF_{525,\ RH}/HBF_{525}$ ratios with n on the P1 and P2 NPF days.

Table S1. Specific dates for different event categories during P1 and P2 periods.

Period	Category	Date
P1	$NPF_{polluted}$	7.29, 8.1-3
	non-event	8.4-6
	Undefined	7.30-31
P2	$NPF_{clean, HW}$	8.7-9, 8.12-14, 8.19
	non-event	8.11, 8.15-16
	Undefined	8.10, 8.17-18

Table S2. A summary (avg. ± std.) of the humidified nephelometer system determined parameters ($\sigma_{sca,\ 525}$, f(RH), ALWC, HBF_{525}, $SAE_{634/450}$, f_W), SMPS-relevant parameters ($N_{conc.}$, $V_{conc.}$, R_{eff}, $NF_{Acc.}$, $VF_{Acc.}$), meteorological parameters (T, RH, WS, VIS, MLH), air pollutants ($PM_{2.5}$, NO_2, SO_2, O_3, CO, O_3/O_X), NPF events related parameters (FR, GR, CS, CoagS), $HBF_{525,\ RH}/HBF_{525}$ and f_{RF}(RH) on NPF event and non-event days, as well as overall mean results during P1 and P2 periods.

	NPF		non-event		Overall	
	P1	P2	P1	P2	P1	P2
$\sigma_{sca,\ 525}$ (Mm^{-1})	103.8 ± 30.4	33.2 ± 11.7	76.7 ± 23.5	54.7 ± 17.6	88.0 ± 29.3	41.2 ± 16.0
f(RH)	1.64 ± 0.10	1.71 ± 0.13	1.62 ± 0.10	1.66 ± 0.12	1.61 ± 0.12	1.71 ± 0.15
ALWC ($\mu g \cdot m^{-3}$)	25.9 ± 6.6	10.2 ± 3.2	18.9 ± 7.5	14.8 ± 4.5	21.4 ± 7.8	12.0 ± 3.9
HBF_{525}	0.134 ± 0.007	0.157 ± 0.011	0.133 ± 0.008	0.152 ± 0.016	0.135 ± 0.008	0.153 ± 0.012
$SAE_{635/450}$	1.31 ± 0.10	1.48 ± 0.13	1.27 ± 0.11	1.44 ± 0.16	1.29 ± 0.12	1.47 ± 0.16
f_W	0.47 ± 0.04	0.48 ± 0.05	0.46 ± 0.04	0.46 ± 0.06	0.46 ± 0.05	0.48 ± 0.05
$N_{conc.}$ (10^4#·cm^{-3})	1.4 ± 0.7	1.2 ± 0.6	0.9 ± 0.3	0.9 ± 0.3	1.2 ± 0.6	1.0 ± 0.6
$V_{conc.}$ ($\mu m^3 \cdot cm^{-3}$)	22.5 ± 5.5	10.1 ± 3.6	17.0 ± 4.8	15.9 ± 5.6	19.5 ± 6.0	12.1 ± 5.0
R_{eff} (nm)	124.8 ± 10.7	102.8 ± 12.4	126.2 ± 10.6	118.6 ± 11.4	125.0 ± 10.0	110.6 ± 13.7
$NF_{ACC.}$	0.28 ± 0.11	0.20 ± 0.10	0.28 ± 0.06	0.33 ± 0.07	0.28 ± 0.09	0.26 ± 0.11
$VF_{ACC.}$	0.96 ± 0.02	0.91 ± 0.04	0.96 ± 0.02	0.96 ± 0.02	0.96 ± 0.02	0.93 ± 0.04
T (°C)	34.0 ± 3.4	36.8 ± 3.1	33.2 ± 3.3	37.6 ± 2.7	33.8 ± 3.4	37.3 ± 3.0
RH (%)	46.6 ± 14.1	34.7 ± 9.1	52.6 ± 13.0	34.0 ± 7.5	47.9 ± 13.7	33.5 ± 8.5
WS (m/s)	1.1 ± 0.6	1.8 ± 1.0	1.4 ± 1.1	1.6 ± 0.9	1.2 ± 0.8	1.8 ± 1.0
VIS (km)	23.3 ± 6.3	29.9 ± 0.7	25.7 ± 5.1	29.2 ± 2.1	25.0 ± 5.6	29.8 ± 1.2
MLH (m)	1062.0 ± 475.6	1461.3 ± 529.9	1075.6 ± 415.4	1340.8 ± 589.8	1063.3 ± 465.8	1454.8 ± 562.6
$PM_{2.5}$ ($\mu g \cdot m^{-3}$)	18.3 ± 6.2	9.3 ± 4.5	10.5 ± 4.2	11.8 ± 4.0	15.1 ± 6.6	10.1 ± 4.4
NO_2 ($\mu g \cdot m^{-3}$)	30.8 ± 18.7	22.7 ± 12.8	21.7 ± 9.6	33.4 ± 19.2	29.8 ± 19.1	24.8 ± 15.4
SO_2 ($\mu g \cdot m^{-3}$)	7.2 ± 1.8	8.8 ± 2.3	6.4 ± 1.5	9.6 ± 3.9	6.9 ± 1.8	9.0 ± 3.0
O_3 ($\mu g \cdot m^{-3}$)	108.2 ± 62.2	84.1 ± 50.2	98.7 ± 51.9	82.3 ± 58.3	100.2 ± 61.1	82.5 ± 49.5
CO ($mg \cdot m^{-3}$)	0.57 ± 0.10	0.44 ± 0.09	0.53 ± 0.05	0.51 ± 0.10	0.55 ± 0.10	0.45 ± 0.09
O_3/O_X	0.71 ± 0.24	0.72 ± 0.21	0.78 ± 0.14	0.62 ± 0.27	0.70 ± 0.25	0.70 ± 0.22
FR ($cm^{-3} \cdot s^{-1}$)	17.10 ± 7.79	11.22 ± 6.81	/	/	/	/
$GR_{<25\ nm}$ ($nm \cdot h^{-1}$)	13.68 ± 3.39	9.31 ± 3.23	/	/	/	/
$GR_{25\text{-}40\ nm}$ ($nm \cdot h^{-1}$)	7.12 ± 2.05	9.22 ± 4.28	/	/	/	/
$GR_{40\text{-}60\ nm}$ ($nm \cdot h^{-1}$)	6.87 ± 6.27	4.41 ± 1.72	/	/	/	/
$GR_{60\text{-}80\ nm}$ ($nm \cdot h^{-1}$)	10.73 ± 8.37	5.51 ± 2.98	/	/	/	/
CS (s^{-1})	2.3 ±	1.3 ±	/	/	/	/

CoagS (s^{-1})	0.4×10^{-2} 1.3 ± 0.2×10^{-4}	0.3×10^{-2} 0.9 ± 0.2×10^{-4}	/	/	/	/
$HBF_{525,\ RH}/HBF_{525}$	1.22 ± 0.10	1.78 ± 0.29	1.39 ± 0.24	1.43 ± 0.18	1.32 ± 0.19	1.63 ± 0.29
f_{RF}(RH)	1.89 ± 0.17	2.21 ± 0.23	1.93 ± 0.14	2.01 ± 0.18	1.91 ± 0.16	2.15 ± 0.23

296

Table S3. A summary of the input parameters for the sensitivity analysis with the Mie models.

	Variable	Mode	Mean	Range
P1 $NPF_{polluted}$	D_{Pg} (nm)	Uf.	39	14-100
		Acc.	173	100-300
	GSD	Uf.	1.69	1.2-2.1
		Acc.	1.56	1.2-2.7
	N_t ($\#\cdot cm^{-3}$)	Uf.	16,844	2,000-28,000
		Acc.	2,311	1,000-5,500
	g(RH)	Uf.	1.14	1.0-1.3
		Acc.	1.26	1.0-1.3
	n	/	1.45	1.3-1.8
P2 $NPF_{clean, HW}$	D_{Pg} (nm)	Uf.	39	14-100
		Acc.	150	100-300
	GSD	Uf.	1.46	1.2-2.1
		Acc.	1.65	1.2-2.7
	N_t ($\#\cdot cm^{-3}$)	Uf.	14,963	2,000-28,000
		Acc.	2,251	1,000-5,500
	g(RH)	Uf.	1.15	1.0-1.3
		Acc.	1.27	1.0-1.3
	n	/	1.44	1.3-1.8

Table S2. A summary (avg. ± std.) of humidified nephelometer system determined parameters ($\sigma_{sca,\ 525}$, f(RH), ALWC, HBF_{525}, $SAE_{634/450}$, f_W), SMPS-relevant parameters ($N_{conc.}$, $V_{conc.}$, R_{eff}, $NF_{Acc.}$, $VF_{Acc.}$), meteorological parameters (T, RH, WS, VIS, MLH), air pollutants ($PM_{2.5}$, NO_2, SO_2, O_3, CO, O_3/O_X), NPF events related parameters (FR, GR, CS, CoagS), $HBF_{525,\ RH}/HBF_{525}$ and f_{RF}(RH) on NPF event and non-event days, as well as overall mean levels during P1 and P2 periods.

	NPF		non-event		Overall	
	P1	P2	P1	P2	P1	P2
$\sigma_{sca,\ 525}$ (Mm^{-1})	103.8 ± 30.4	33.2 ± 11.7	76.7 ± 23.5	54.7 ± 17.6	88.0 ± 29.3	41.2 ± 16.0
f(RH)	1.64 ± 0.10	1.71 ± 0.13	1.62 ± 0.10	1.66 ± 0.12	1.61 ± 0.12	1.71 ± 0.15
ALWC ($\mu g \cdot m^{-3}$)	25.9 ± 6.6	10.2 ± 3.2	18.9 ± 7.5	14.8 ± 4.5	21.4 ± 7.8	12.0 ± 3.9
HBF_{525}	0.134 ± 0.007	0.157 ± 0.011	0.133 ± 0.008	0.152 ± 0.016	0.135 ± 0.008	0.153 ± 0.012
$SAE_{635/450}$	1.31 ± 0.10	1.48 ± 0.13	1.27 ± 0.11	1.44 ± 0.16	1.29 ± 0.12	1.47 ± 0.16
f_W	0.47 ± 0.04	0.48 ± 0.05	0.46 ± 0.04	0.46 ± 0.06	0.46 ± 0.05	0.48 ± 0.05
$N_{conc.}$ (10^4#$\cdot cm^{-3}$)	1.4 ± 0.7	1.2 ± 0.6	0.9 ± 0.3	0.9 ± 0.3	1.2 ± 0.6	1.0 ± 0.6
$V_{conc.}$ ($\mu m^3 \cdot cm^{-3}$)	22.5 ± 5.5	10.1 ± 3.6	17.0 ± 4.8	15.9 ± 5.6	19.5 ± 6.0	12.1 ± 5.0
R_{eff} (nm)	124.8 ± 10.7	102.8 ± 12.4	126.2 ± 10.6	118.6 ± 11.4	125.0 ± 10.0	110.6 ± 13.7
$NF_{ACC.}$	0.28 ± 0.11	0.20 ± 0.10	0.28 ± 0.06	0.33 ± 0.07	0.28 ± 0.09	0.26 ± 0.11
$VF_{ACC.}$	0.96 ± 0.02	0.91 ± 0.04	0.96 ± 0.02	0.96 ± 0.02	0.96 ± 0.02	0.93 ± 0.04
T (°C)	34.0 ± 3.4	36.8 ± 3.1	33.2 ± 3.3	37.6 ± 2.7	33.8 ± 3.4	37.3 ± 3.0
RH (%)	46.6 ± 14.1	34.7 ± 9.1	52.6 ± 13.0	34.0 ± 7.5	47.9 ± 13.7	33.5 ± 8.5
WS (m/s)	1.1 ± 0.6	1.8 ± 1.0	1.4 ± 1.1	1.6 ± 0.9	1.2 ± 0.8	1.8 ± 1.0
VIS (km)	23.3 ± 6.3	29.9 ± 0.7	25.7 ± 5.1	29.2 ± 2.1	25.0 ± 5.6	29.8 ± 1.2
MLH (m)	1062.0 ± 475.6	1461.3 ± 529.9	1075.6 ± 415.4	1340.8 ± 589.8	1063.3 ± 465.8	1454.8 ± 562.6
$PM_{2.5}$ ($\mu g \cdot m^{-3}$)	18.3 ± 6.2	9.3 ± 4.5	10.5 ± 4.2	11.8 ± 4.0	15.1 ± 6.6	10.1 ± 4.4

NO_2 ($\mu g \cdot m^{-3}$)	30.8 ± 18.7	22.7 ± 12.8	21.7 ± 9.6	33.4 ± 19.2	29.8 ± 19.1	24.8 ± 15.4
SO_2 ($\mu g \cdot m^{-3}$)	7.2 ± 1.8	8.8 ± 2.3	6.4 ± 1.5	9.6 ± 3.9	6.9 ± 1.8	9.0 ± 3.0
O_3 ($\mu g \cdot m^{-3}$)	108.2 ± 62.2	84.1 ± 50.2	98.7 ± 51.9	82.3 ± 58.3	100.2 ± 61.1	82.5 ± 49.5
CO ($mg \cdot m^{-3}$)	0.57 ± 0.10	0.44 ± 0.09	0.53 ± 0.05	0.51 ± 0.10	0.55 ± 0.10	0.45 ± 0.09
O_3/O_X	0.71 ± 0.24	0.72 ± 0.21	0.78 ± 0.14	0.62 ± 0.27	0.70 ± 0.25	0.70 ± 0.22
FR ($cm^{-3} \cdot s^{-1}$)	17.10 ± 7.79	11.22 ± 6.81	/	/	/	/
$GR_{<25\ nm}$ ($nm \cdot h^{-1}$)	13.68 ± 3.39	9.31 ± 3.23	/	/	/	/
$GR_{25\text{-}40\ nm}$ ($nm \cdot h^{-1}$)	7.12 ± 2.05	9.22 ± 4.28	/	/	/	/
$GR_{40\text{-}60\ nm}$ ($nm \cdot h^{-1}$)	6.87 ± 6.27	4.41 ± 1.72	/	/	/	/
$GR_{60\text{-}80\ nm}$ ($nm \cdot h^{-1}$)	10.73 ± 8.37	5.51 ± 2.98	/	/	/	/
CS (s^{-1})	$2.3 \pm 0.4 \times 10^{-2}$	$1.3 \pm 0.3 \times 10^{-2}$	/	/	/	/
CoagS (s^{-1})	$1.3 \pm 0.2 \times 10^{-4}$	$0.9 \pm 0.2 \times 10^{-4}$	/	/	/	/
$HBF_{525,\ RH}/HBF_{525}$	1.22 ± 0.10	1.78 ± 0.29	1.39 ± 0.24	1.43 ± 0.18	1.32 ± 0.19	1.63 ± 0.29
f_{RF}(RH)	1.89 ± 0.17	2.21 ± 0.23	1.93 ± 0.14	2.01 ± 0.18	1.91 ± 0.16	2.15 ± 0.23

304

References

Brock, C. A., Wagner, N. L., Anderson, B. E., Attwood, A. R., Beyersdorf, A., Campuzano-Jost, P., Carlton, A. G., Day, D. A., Diskin, G. S., Gordon, T. D., Jimenez, J. L., Lack, D. A., Liao, J., Markovic, M. Z., Middlebrook, A. M., Ng, N. L., Perring, A. E., Richardson, M. S., Schwarz, J. P., Washenfelder, R. A., Welti, A., Xu, L., Ziemba, L. D., and Murphy, D. M.: Aerosol optical properties in the southeastern United States in summer - Part 1: Hygroscopic growth, Atmos. Chem. Phys., 16, 4987–5007, https://doi.org/10.5194/acp-16-4987-2016, 2016.

Castro, L. M., Pio, C. A., Harrison, R. M., and Smith, D. J. T.: Carbonaceous aerosol in urban and rural European atmospheres: Estimation of secondary organic carbon concentrations, Atmos. Environ., 33, 2771–2781, https://doi.org/10.1016/S1352-2310(98)00331-8, 1999.

Chen, J., Wu, Z., Chen, J., Reicher, N., Fang, X., Rudich, Y., and Hu, M.: Size-resolved atmospheric ice-nucleating particles during East Asian dust events, Atmos. Chem. Phys., 21, 3491–3506, https://doi.org/10.5194/acp-21-3491-2021, 2021.

Chen, J., Zhao, C. S., Ma, N., Liu, P. F., Göbel, T., Hallbauer, E., Deng, Z. Z., Ran, L., Xu, W. Y., Liang, Z., Liu, H. J., Yan, P., Zhou, X. J., and Wiedensohler, A.: A parameterization of low visibilities for hazy days in the North China Plain, Atmos.

Chow, J. C., Watson, J. G., Chen, L. W. A., Chang, M. C. O., Robinson, N. F., Trimble, D., and Kohl, S.: The IMPROVE_A temperature protocol for thermal/optical carbon analysis: Maintaining consistency with a long-term database, J. Air Waste Manag. Assoc., 57, 1014–1023, https://doi.org/10.3155/1047-3289.57.9.1014, 2007.

Chow, J. C., Watson, J. G., Robles, J., Wang, X., Chen, L. W. A., Trimble, D. L., Kohl, S. D., Tropp, R. J., and Fung, K. K.: Quality assurance and quality control for thermal/optical analysis of aerosol samples for organic and elemental carbon, Anal. Bioanal. Chem., 401, 3141–3152, https://doi.org/10.1007/s00216-011-5103-3, 2011.

Dal Maso, M., Kulmala, M., Riipinen, I., Wagner, R., Hussein, T., Aalto, P. P., and Lehtinen, K. E. J.: Formation and growth of fresh atmospheric aerosols: Eight years of aerosol size distribution data from SMEAR II, Hyytiälä, Finland, Boreal Environ. Res., 10, 323–336, 2005.

Denjean, C., Formenti, P., Picquet-Varrault, B., Camredon, M., Pangui, E., Zapf, P., Katrib, Y., Giorio, C., Tapparo, A., Temime-Roussel, B., Monod, A., Aumont, B., and Doussin, J. F.: Aging of secondary organic aerosol generated from the ozonolysis of α-pinene: Effects of ozone, light and temperature, Atmos. Chem. Phys., 15, 883–897, https://doi.org/10.5194/acp-15-883-2015, 2015.

Dominick, D., Wilson, S. R., Paton-Walsh, C., Humphries, R., Guérette, E. A., Keywood, M., Kubistin, D., and Marwick, B.: Characteristics of airborne particle number size distributions in a coastal-urban environment, Atmos. Environ., 186, 256–265, https://doi.org/10.1016/j.atmosenv.2018.05.031, 2018.

Fitsiou, E., Pulido, T., Campisi, J., Alimirah, F., and Demaria, M.: Cellular Senescence and the Senescence-Associated Secretory Phenotype as Drivers of Skin Photoaging, J. Invest. Dermatol., 141, 1119–1126, https://doi.org/10.1016/j.jid.2020.09.031, 2021.

Grainger, R. G., Lambert, A., Rodgers, C. D., Taylor, F. W., and Deshler, T.: Stratospheric aerosol effective radius, surface area and volume estimated from infrared measurements, J. Geophys. Res., 100, https://doi.org/10.1029/95jd00988, 1995.

Hamed, A., Joutsensaari, J., Mikkonen, S., Sogacheva, L., Dal Maso, M., Kulmala, M., Cavalli, F., Fuzzi, S., Facchini, M. C., Decesari, S., Mircea, M., Lehtinen, K. E. J., and Laaksonen, A.: Nucleation and growth of new particles in Po Valley, Italy, Atmos. Chem. Phys., 7, 355–376, https://doi.org/10.5194/acp-7-355-2007, 2007.

Hansen, J. E. and Travis, L. D.: Light scattering in planetary atmospheres, Space Sci. Rev., 16, 527–610, https://doi.org/10.1007/BF00168069, 1974.

Hao, Y., Gou, Y., Wang, Z., Huang, W., Wan, F., Tian, M., and Chen, J.: Current challenges in the visibility improvement of urban Chongqing in Southwest China: From

the perspective of PM2.5-bound water uptake property over 2015–2021, Atmos. Res., 300, 107215, https://doi.org/10.1016/j.atmosres.2023.107215, 2024.

Hong, J., Ma, J., Ma, N., Shi, J., Xu, W., Zhang, G., Zhu, S., Zhang, S., Tang, M., Pan, X., Xie, L., Li, G., Kuhn, U., Yan, C., Qi, X., Zha, Q., Nie, W., Tao, J., He, Y., Zhou, Y., Sun, Y., Xu, H., Liu, L., Cai, R., Zhou, G., Kuang, Y., Yuan, B., Wang, Q., Petäjä, T., Kerminen, V. M., Kulmala, M., Cheng, Y., and Su, H.: Low Hygroscopicity of Newly Formed Particles on the North China Plain and Its Implications for Nanoparticle Growth, Geophys. Res. Lett., 51, https://doi.org/10.1029/2023GL107516, 2024.

Hussein, T., Puustinen, A., Aalto, P. P., Mäkelä, J. M., Hämeri, K., and Kulmala, M.: Urban aerosol number size distributions, Atmos. Chem. Phys., 4, 391–411, https://doi.org/10.5194/acp-4-391-2004, 2004.

Jung, C. H., Shin, H. J., Lee, J. Y., and Kim, Y. P.: Sensitivity and contribution of organic aerosols to aerosol optical properties based on their refractive index and hygroscopicity, Atmosphere (Basel)., 7, https://doi.org/10.3390/atmos7050065, 2016.

Kerminen, V. M., Chen, X., Vakkari, V., Petäjä, T., Kulmala, M., and Bianchi, F.: Atmospheric new particle formation and growth: Review of field observations, Environ. Res. Lett., 13, https://doi.org/10.1088/1748-9326/aadf3c, 2018.

Kuang, Y., He, Y., Xu, W., Zhao, P., Cheng, Y., Zhao, G., Tao, J., Ma, N., Su, H., Zhang, Y., Sun, J., Cheng, P., Yang, W., Zhang, S., Wu, C., Sun, Y., and Zhao, C.: Distinct diurnal variation in organic aerosol hygroscopicity and its relationship with oxygenated organic aerosol, Atmos. Chem. Phys., 20, 865–880, https://doi.org/10.5194/acp-20-865-2020, 2020.

Kuang, Y., Zhao, C. S., Zhao, G., Tao, J. C., Xu, W., Ma, N., and Bian, Y. X.: A novel method for calculating ambient aerosol liquid water content based on measurements of a humidified nephelometer system, Atmos. Meas. Tech., 11, 2967–2982, https://doi.org/10.5194/amt-11-2967-2018, 2018.

384 Kuang, Y., Zhao, C., Tao, J., Bian, Y., Ma, N., and Zhao, G.: A novel method for
385 deriving the aerosol hygroscopicity parameter based only on measurements from a
386 humidified nephelometer system, Atmos. Chem. Phys., 17, 6651–6662,
387 https://doi.org/10.5194/acp-17-6651-2017, 2017.

388 Kulmala, M., Petäjä, T., Nieminen, T., Sipilä, M., Manninen, H. E., Lehtipalo, K., Dal
389 Maso, M., Aalto, P. P., Junninen, H., Paasonen, P., Riipinen, I., Lehtinen, K. E. J.,
390 Laaksonen, A., and Kerminen, V. M.: Measurement of the nucleation of atmospheric
391 aerosol particles, Nat. Protoc., 7, 1651–1667, https://doi.org/10.1038/nprot.2012.091,
392 2012.

393 Lu, Y., Yan, C., Fu, Y., Chen, Y., Liu, Y., Yang, G., Wang, Y., Bianchi, F., Chu, B.,
394 Zhou, Y., Yin, R., Baalbaki, R., Garmash, O., Deng, C., Wang, W., Liu, Y., Petäjä, T.,
395 Kerminen, V. M., Jiang, J., Kulmala, M., and Wang, L.: A proxy for atmospheric daytime
396 gaseous sulfuric acid concentration in urban Beijing, Atmos. Chem. Phys., 19, 1971–
397 1983, https://doi.org/10.5194/acp-19-1971-2019, 2019.

398 Nairn, J. R. and Fawcett, R. J. B.: The excess heat factor: A metric for heatwave intensity
399 and its use in classifying heatwave severity, Int. J. Environ. Res. Public Health, 12, 227–
400 253, https://doi.org/10.3390/ijerph120100227, 2014.

401 Peng, C., Tian, M., Chen, Y., Wang, H., Zhang, L., Shi, G., Liu, Y., Yang, F., and Zhai,
402 C.: Characteristics, formation mechanisms and potential transport pathways of PM2.5 at a
403 rural background site in Chongqing, Southwest China, Aerosol Air Qual. Res., 19, 1980–
404 1992, https://doi.org/10.4209/aaqr.2019.01.0010, 2019.

405 Peng, C., Tian, M., Wang, X., Yang, F., Shi, G., Huang, R. J., Yao, X., Wang, Q., Zhai,
406 C., Zhang, S., Qian, R., Cao, J., and Chen, Y.: Light absorption of brown carbon in
407 PM2.5 in the Three Gorges Reservoir region, southwestern China: Implications of
408 biomass burning and secondary formation, Atmos. Environ., 229, 117409,
409 https://doi.org/10.1016/j.atmosenv.2020.117409, 2020.

410 Rissler, J., Vestin, A., Swietlicki, E., Fisch, G., Zhou, J., Artaxo, P., and Andreae, M. O.:
411 Size distribution and hygroscopic properties of aerosol particles from dry-season biomass

burning in Amazonia, Atmos. Chem. Phys., 6, 471–491, https://doi.org/10.5194/acp-6-471-2006, 2006.

Rosati, B., Isokääntä, S., Christiansen, S., Jensen, M. M., Moosakutty, S. P., De Jonge, R. W., Massling, A., Glasius, M., Elm, J., Virtanen, A., and Bilde, M.: Hygroscopicity and CCN potential of DMS-derived aerosol particles, Atmos. Chem. Phys., 22, 13449–13466, https://doi.org/10.5194/acp-22-13449-2022, 2022.

Schkolnik, G., Chand, D., Hoffer, A., Andreae, M. O., Erlick, C., Swietlicki, E., and Rudich, Y.: Constraining the density and complex refractive index of elemental and organic carbon in biomass burning aerosol using optical and chemical measurements, Atmos. Environ., 41, 1107–1118, https://doi.org/10.1016/j.atmosenv.2006.09.035, 2007.

Stein, A. F., Draxler, R. R., Rolph, G. D., Stunder, B. J. B., Cohen, M. D., and Ngan, F.: Noaa's hysplit atmospheric transport and dispersion modeling system, Bull. Am. Meteorol. Soc., 96, 2059–2077, https://doi.org/10.1175/BAMS-D-14-00110.1, 2015.

Strader, R., Lurmann, F., and Pandis, S. N.: Evaluation of secondary organic aerosol formation in winter, Atmos. Environ., 33, 4849–4863, https://doi.org/10.1016/S1352-2310(99)00310-6, 1999.

Tan, F., Zhang, H., Xia, K., Jing, B., Li, X., Tong, S., and Ge, M.: Hygroscopic behavior and aerosol chemistry of atmospheric particles containing organic acids and inorganic salts, npj Clim. Atmos. Sci., 7, 1–21, https://doi.org/10.1038/s41612-024-00752-9, 2024.

Tian, J., Guan, H., Zhou, Y., Zheng, N., Xiao, H., Zhao, J., Zhang, Z., and Xiao, H.: Isotopic source analysis of nitrogen-containing aerosol: A study of PM2.5 in Guiyang (SW, China), Sci. Total Environ., 760, 143935, https://doi.org/10.1016/j.scitotenv.2020.143935, 2021.

Wan, F., Hao, Y., Huang, W., Wang, X., Tian, M., and Chen, J.: Hindered visibility improvement despite marked reduction in anthropogenic emissions in a megacity of southwestern China: An interplay between enhanced secondary inorganics formation and

hygroscopic growth at prevailing high RH conditions, Sci. Total Environ., 895, 165114, https://doi.org/10.1016/j.scitotenv.2023.165114, 2023.

Wang, H., Tian, M., Chen, Y., Shi, G., Liu, Y., Yang, F., Zhang, L., Deng, L., Yu, J., Peng, C., and Cao, X.: Seasonal characteristics, formation mechanisms and source origins of PM2.5 in two megacities in Sichuan Basin, China, Atmos. Chem. Phys., 18, 865–881, https://doi.org/10.5194/acp-18-865-2018, 2018.

Wang, Y. Q.: MeteoInfo: GIS software for meteorological data visualization and analysis, Meteorol. Appl., 21, 360–368, https://doi.org/10.1002/met.1345, 2014.

Xu, W., Kuang, Y., Bian, Y., Liu, L., Li, F., Wang, Y., Xue, B., Luo, B., Huang, S., Yuan, B., Zhao, P., and Shao, M.: Current Challenges in Visibility Improvement in Southern China, Environ. Sci. Technol. Lett., 7, 395–401, https://doi.org/10.1021/acs.estlett.0c00274, 2020.

Xue, B., Kuang, Y., Xu, W., and Zhao, P.: Joint increase of aerosol scattering efficiency and aerosol hygroscopicity aggravate visibility impairment in the North China Plain, Sci. Total Environ., 839, 141163, https://doi.org/10.1016/j.scitotenv.2022.156279, 2022.

Zhao, G., Hu, M., Fang, X., Tan, T., Xiao, Y., Du, Z., Zheng, J., Shang, D., Wu, Z., Guo, S., and Zhao, C.: Larger than expected variation range in the real part of the refractive index for ambient aerosols in China, Sci. Total Environ., 779, 146443, https://doi.org/10.1016/j.scitotenv.2021.146443, 2021.

Zhu, Y., Shen, Y., Li, K., Meng, H., Sun, Y., Yao, X., Gao, H., Xue, L., and Wang, W.: Investigation of Particle Number Concentrations and New Particle Formation With Largely Reduced Air Pollutant Emissions at a Coastal Semi-Urban Site in Northern China, J. Geophys. Res. Atmos., 126, 1–20, https://doi.org/10.1029/2021JD035419, 2021.